The University Of Sheffield.

New development of Subchannel CFD for complex flows in nuclear reactor system

Chenxin Zhang

A thesis submitted in partial fulfilment of the requirements for the degree of

Doctor of Philosophy

The University of Sheffield

Faculty of Engineering

School of Mechanical , Aerospace and Civil Engineering

Submission Date

21/05/2025

This thesis is dedicated to
My wife Wenxiao
for her patience, love, and constant support throughout this journey.

Acknowledgements

First and foremost, I would like to express my sincere gratitude to my primary supervisor, Professor Shuisheng He. I am very thankful that he gave me the opportunity to continue my research as a PhD student. During the past four years, he has provided continuous guidance and valuable suggestions. His support has been important not only for my academic progress but also for my personal growth and mental well-being.

I would also like to extend my sincere thanks to my second supervisor, Dr. Bo Liu, who provided essential technical support and guidance throughout my research. I greatly appreciate his patience, dedication, and the time he spent helping me, especially in his role as an external supervisor.

I am deeply grateful to my family for their support throughout this journey. I would especially like to thank my wife, Miss Wenxiao Tan, for her understanding and for supporting my decision to continue my studies. Although we have been living in different countries during these years, with me in the UK and her in China, she has always supported me with care and patience. Her encouragement during difficult times has meant a great deal to me, and I am truly grateful for her support and for waiting for me during this precious stage of her life.

Finally, I would like to thank all the friends I met during my PhD. They have been an important part of my life over the past four years. Their support and company helped me stay positive and keep a good balance between studying and daily life.

Abstract

This thesis presents new developments of a coarse-grid CFD method known as Subchannel CFD (SubChCFD) for the thermal-hydraulic analysis of nuclear reactors. The focus is on extending the capability of SubChCFD in capturing complex phenomena such as variable-property and buoyancy effects under supercritical conditions, flow swirl phenomena in wire-wrapped rod bundle configuration, and flow instabilities in the natural circulation loop (NCL). While traditional system and sub-channel codes offer computational efficiency, they are not designed to resolve local flow features. In contrast, high-fidelity CFD methods provide detailed insights but are computationally intensive, particularly for large-scale configurations. For supercritical conditions, developments include the implementation of empirical heat transfer and friction factor correlations for mixed convection and entrance region effects. The developments are validated through comparisons with resolved CFD simulations and available experimental data, showing reasonable accuracy across a range of operating conditions. Further developments are made to enable simulation of wire-wrapped fuel assemblies by incorporating momentum source terms to account for the influence of helical spacers. Furthermore, the SubChCFD is applied to natural circulation loop systems to assess its ability to reproduce flow instabilities. In summary, the work reported herein has extended the capability of SubChCFD to deal with a number of complex flows encountered in nuclear reactors successfully, and has demonstrated that SubChCFD captures key thermal-hydraulic features, such as heat transfer enhancement and deterioration, secondary flow structures, and oscillatory flow behaviour. This work further establishes SubChCFD as a practical alternative for a nuclear thermal-hydraulic analysis tool.

Contents

List of Figures

Chapter 1

Introduction

1.1 Background

The increasing demand for clean and reliable energy has highlighted the importance of nuclear power as a stable, low-carbon energy source. Generation IV reactors are advanced designs aimed at improving thermal efficiency, operational safety, and environmental sustainability. One particularly promising concept within this generation is the Supercritical Water-Cooled Reactor (SCWR), which operates at pressures and temperatures above the critical point of water.

However, the thermal-hydraulic analysis of supercritical systems presents several challenges. Near the pseudo-critical point, supercritical fluids exhibit drastic changes in thermal physical properties with small temperature variations. In addition, buoyancy effects can significantly influence bulk flow parameters in subchannel regions and alter wall temperature distributions. Consideration of these phenomena is essential for accurately predicting fluid behaviour and heat transfer performance under supercritical conditions.

In addition, complex reactor geometries such as rod bundles with wire-wrap spacers introduce further modelling challenges. Wire-wrap spacers are designed to enhance mixing and promote more uniform temperature distributions across subchannels. However, they also induce secondary flows and lead to increased pressure losses. Accurately capturing these effects is crucial for predicting flow distribution, pressure drop, and thermal performance in wire-wrapped fuel assemblies.

Natural circulation loops (NCLs) represent another area of complexity, especially in the context of passive safety. These systems rely on buoyancy-driven flow without external mechanical or electrical power, making them sensitive to flow instabilities and reversal phenomena. Examples of passive cooling systems include the Passive

Residual Heat Removal (PRHR) system and the Passive Containment Cooling System (PCCS) in the AP1000 reactor, as well as the Supercritical Pressure Natural Circulation Loop (SPNCL) at Bhabha Atomic Research Centre. Accurate modelling is essential to capture the complex fluid behaviours in these systems.

Traditional system and sub-channel codes offer computational efficiency but often lack the spatial resolution required to capture local effects such as flow redistribution, secondary flows, and entrance region behaviour. In contrast, high-fidelity Computational Fluid Dynamics (CFD) simulations can resolve these details but are typically too computationally demanding for large-scale or engineering applications.

To address this gap, this PhD study adopts a coarse-grid CFD approach called Subchannel CFD (SubChCFD), which combines the efficiency of sub-channel methods with the conventional resolved CFD method. The study includes modelling methodology developments, coding and validations against experimental and resolved CFD data.

1.2 Aim and Objectives

The primary aim of this research is to further develop SubChCFD to handle challenges, including variable thermal physical properties and buoyancy effects in supercritical conditions, flow swirl in wire-wrapped rod bundles, and instability phenomena in NCL systems. To achieve the stated aim, the following objectives are established:

- Further develop SubChCFD for supercritical thermal-hydraulic analysis, incorporating appropriate heat transfer and friction factor correlations.
- Extend the capability of SubChCFD to simulate wire-wrapped rod bundles by introducing momentum source terms to represent wire-induced effect.
- Apply SubChCFD to natural circulation loops to evaluate its ability to capture the instabilities;

1.3 Significance and Contributions

This research advances the field of nuclear thermal-hydraulic analysis by developing and applying the SubChCFD as a computationally efficient alternative to fully resolved CFD simulations. The key contributions of this PhD work are as follows:

- Further development of the SubChCFD framework for the modelling of flow and heat transfer in rod bundle geometries under supercritical conditions, accounting for strong buoyancy effects and rapid variations in thermal physical properties;
- Integration of empirical heat transfer and friction factor correlations to enhance the capability of SubChCFD in capturing buoyancy-influenced supercritical flows, including entrance-region effects;
- Introduction of momentum source terms to represent the influence of wire-wrap spacers, enabling SubChCFD to simulate secondary flow structures in wire-wrapped rod bundles;
- Application of the SubChCFD approach to NCLs, demonstrating its capability to capture flow instabilities in passive safety systems.

1.4 Thesis Outline

This thesis is structured as follows:

- **Chapter 2 - Literature Review:** Reviews SCWR technology, thermal-hydraulic modelling approaches, such as system code, subchannel code and the state of the art in CFD. It also covers numerical and experimental investigations related to mixed convection studies, wire-wrapped rod bundles and natural circulation loops;
- **Chapter 3 - Methodology:** Describes the governing equations, turbulence models, and numerical schemes used in the conventional CFD approach, as well as the fundamental methodology of the SubChCFD framework.
- **Chapter 4 - Development and Application of SubChCFD for Supercritical Fluid Heat Transfer:** Extends the SubChCFD approach for supercritical conditions by implementing various heat transfer and friction factor correlations. This chapter includes validation against CFD and experimental data, and examines buoyancy-driven flow redistribution in rod bundle configurations.
- **Chapter 5 - Development for the wire-wrapped rod bundles:** Extends the SubChCFD to model wire-wrapped fuel assemblies by incorporating momentum source terms to represent wire-induced effect. The approach is validated against experimental measurements and high-fidelity CFD simulations.

- **Chapter 6 - Application of SubChCFD in Natural Circulation Loops:** Further develops and demonstrates the capability of the SubChCFD to simulate flow instability phenomena in natural circulation loops.
- **Chapter 7 - Conclusion and Future Work:** Summarises the key findings of the research and outlines potential directions for further development of SubChCFD.

Chapter 2

Literature review

2.1 Supercritical water-cooled reactor (SCWR)

2.1.1 Overview of SCWR

The Supercritical Water-Cooled Reactor (SCWR) is a Generation IV nuclear reactor design that utilizes water as both a coolant and a moderator, designed to achieve higher thermal efficiency, enhanced safety, and reduced environmental impact. It integrates the principles of conventional Light Water Reactors (LWRs) with the high efficiency of Supercritical Fossil Power Plants (FPPs). Operating at a core pressure of 25 MPa, the SCWR achieves a thermal efficiency of approximately 45%, significantly higher than that of traditional LWRs which is typically around 30% [102].

Unlike traditional boiling water reactors (BWRs) and pressurized water reactors (PWRs), which involve phase changes, SCWRs operate in a single-phase regime above the critical point of water (22.1 MPa at 374°C). This ensures that no phase transition occurs, eliminating the need for steam separators and dryers, thus simplifying reactor design while improving thermal efficiency.

Figure 2.1 illustrates a typical SCWR system, where the coolant, heated by reactor fuel, is directly supplied to the turbine to generate electricity. The absence of phase change allows for simplified thermal management, leading to a more compact system design [102].

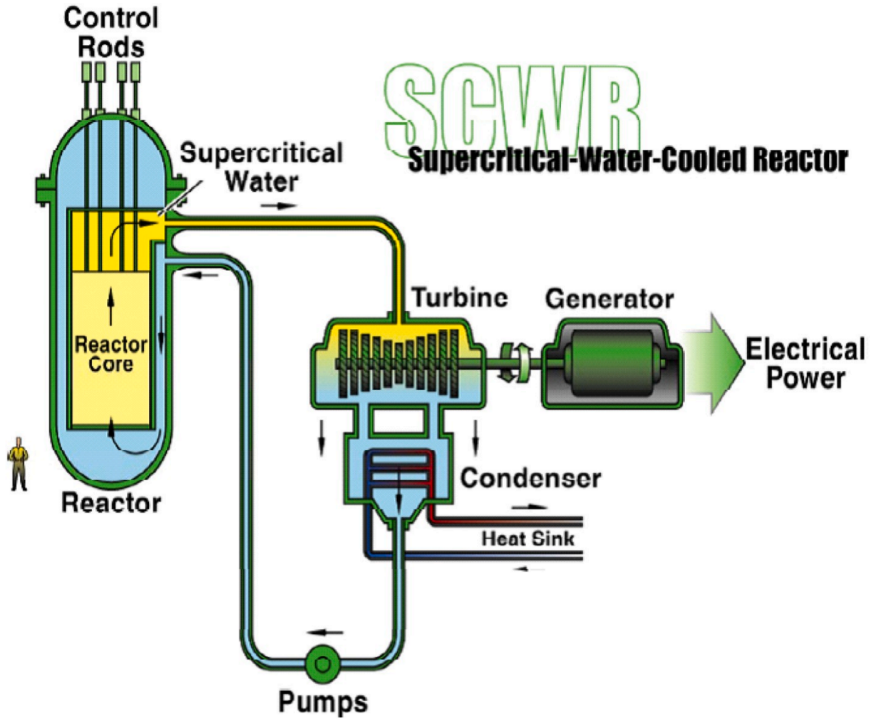

Figure 2.1: A typical SCWR system [102].

2.1.2 Design concept

An SCWR operates above the critical pressure ($\approx 25\,\mathrm{MPa}$) with single-phase supercritical water, typically entering the core at 280-350 °C and exiting at 500-625 °C; strong property gradients near the pseudocritical temperature ($\sim 390\,^{\circ}\mathrm{C}$ at 25 MPa) make heat-transfer prediction challenging. Core mass flux is concept-dependent but commonly 400–1200 $\mathrm{kg\,m^{-2}\,s^{-1}}$.

Several countries have contributed to the development of SCWR designs, each focusing on different core configurations and fuel assemblies to optimize reactor performance. These efforts can be categorized into two main types: pressure tube and pressure vessel designs.

- **Japan**: One of the earliest SCWR designs was proposed by Oka et al. [95], featuring a hexagonal fuel assembly with zirconium hydride (ZrH) moderators. Later, American researchers assessed various moderators, ultimately selecting ZrH_x due to its superior neutronic performance [19].

- **Korea**: The Korean SCWR design incorporates square fuel assemblies with a cruciform U/Zr solid moderator, which simplifies the water flow path. The fuel

enrichment varies axially and radially to enhance neutron economy. A power plant with a capacity of 1400 MWe has been designed to operate at an outlet temperature of 510°C [64].

- **Europe (HPLWR Project)**: As part of the 5th Framework Program, European researchers have explored a pressure vessel-type SCWR. Their investigations focused on reactor feasibility at supercritical conditions, particularly at an operating pressure of approximately 25 MPa and a coolant temperature range of 280 to 500°C [113].

- **Canada (AECL SCWR)**: Developed by Atomic Energy Canada Limited (AECL), the Canadian SCWR follows the well-established CANDU reactor principles, utilizing a pressure tube system. Its primary objective is electricity generation, with additional applications in hydrogen production, process heating, and water desalination [139].

- **China (CSR1000 by NPIC)**: In 2014, the Nuclear Power Institute of China (NPIC) proposed the CSR1000, a pressure vessel-type SCWR operating in the thermal spectrum. The reactor has a thermal power output of 2300 MW and an electrical power output of 1000 MW, with a core inlet temperature of 280°C and an outlet temperature of 500°C, achieving a thermal efficiency of approximately 45% [136].

2.1.3 Thermal-hydraulic challenges

Under supercritical conditions, the thermal-hydraulic behaviour of fluids differs from that in subcritical regimes. In subcritical flows, phase changes occur, characterised by the coexistence of liquid and vapour phases. This is evident in the temperature–entropy (T–s) diagram of water (Figure 2.2), where horizontal segments at constant pressure represent the two-phase region bounded by the saturated liquid and saturated vapour lines. However, above the critical point (22.1 MPa, 374 °C), these discontinuities vanish, and water transitions smoothly from a liquid-like to a gas-like state without a phase change. This continuous variation in thermal physical properties is a defining feature of supercritical fluids and is particularly relevant in SCWR applications.

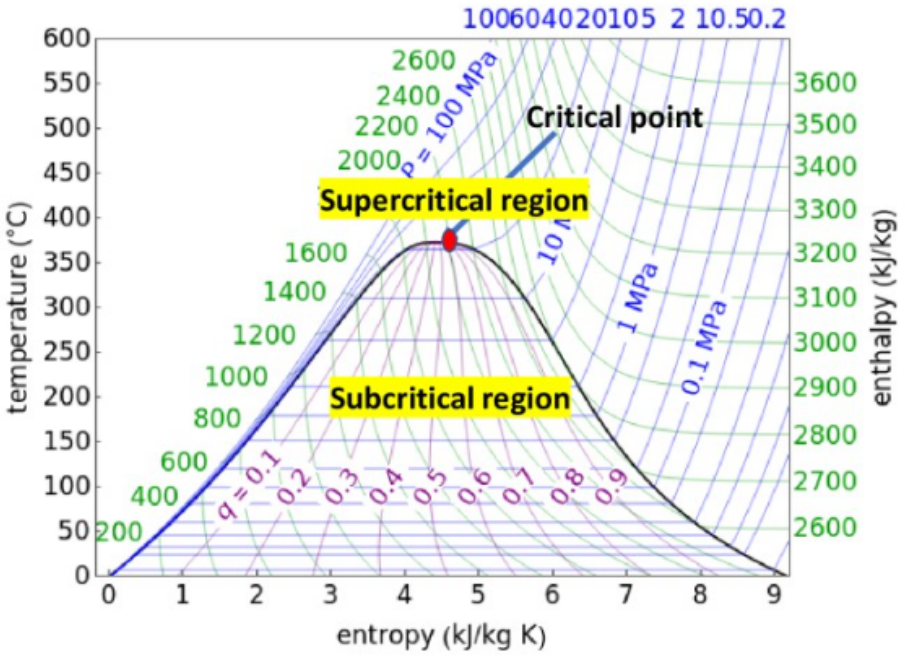

Figure 2.2: T-s diagram of water [62]

.

In this single-phase supercritical flow regime, fluids exhibit strong variations in their thermal physical properties near the pseudo-critical region. This behaviour is illustrated in Figure 2.3, which presents the temperature-dependent variations of water properties at 25 MPa.

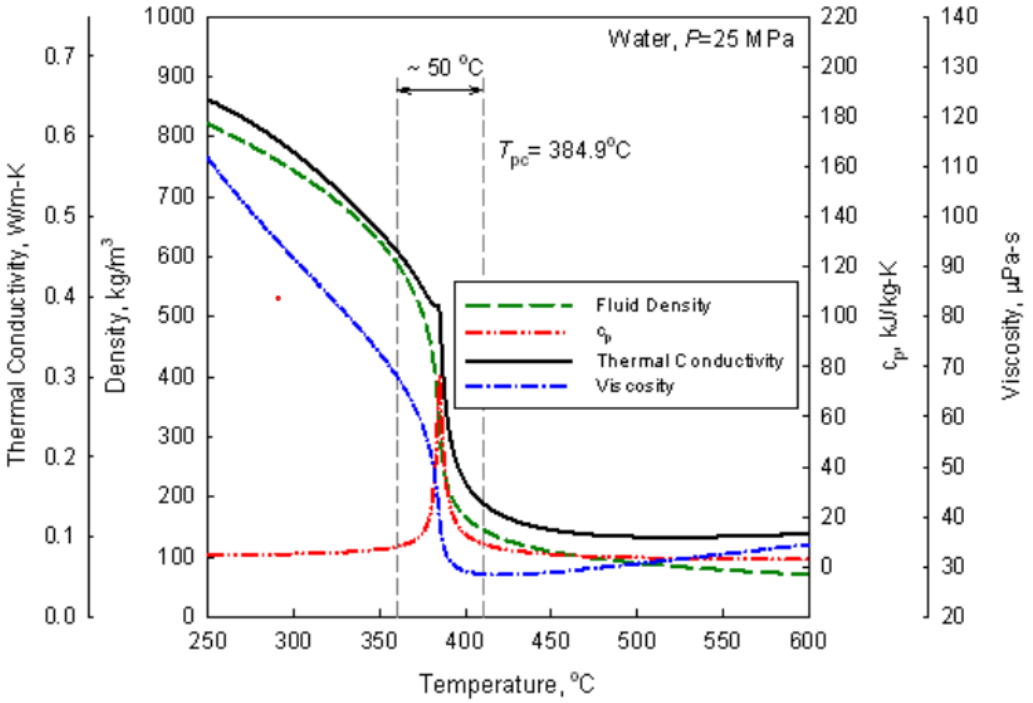

Figure 2.3: Variation of fluid properties near the pseudo-critical point at 25 MPa [46].

The drastic variations of thermal properties near the pseudo-critical region significantly affect flow and heat transfer behaviour. For instance, buoyancy forces can be really strong due to the rapid decrease in fluid density, and heat transfer and flow behaviour are also strongly influenced by rapid changes in thermal conductivity and viscosity. The ability of fluid to absorb energy significantly increases near the pseudo-critical point, as indicated by a pronounced peak in specific heat capacity (C_p). These strong property variations introduce challenges in predicting flow and heat transfer behaviour under supercritical conditions.

Understanding and predicting the thermal-hydraulic phenomena under supercritical conditions are essential for the development of SCWRs and other applications of supercritical fluids. Experimental studies play a crucial role in directly investigating the complex phenomena, enhancing fundamental understanding, and providing essential data for numerical model validation. However, experimental facilities for supercritical conditions are expensive and challenging to operate. Therefore, numerical methods are important as complementary approaches to investigate flow and heat transfer behaviours in this area. Various approaches have been developed to model and predict heat transfer and flow characteristics under these conditions. These methods broadly fall into three categories: system codes, sub-channel codes, and computational fluid dynamics (CFD) models. Numerical simulations face key challenges,

including managing rapid changes in fluid properties, analysing mixed convection with significant buoyancy effects, and accurately modelling complex geometries like wire-wrapped rod bundles. Additionally, thermal-hydraulic behaviour predictions in Natural Circulation Loops (NCLs), which are relevant to the passive cooling systems, are also quite challenging. A literature review of numerical approaches and experimental work related to different topics will be presented in later sections.

2.2 Thermal-hydraulic Analysis Methods

Thermal-hydraulic analysis plays an essential role in nuclear reactor design and operation. It evaluates key parameters such as critical heat flux (CHF), wall temperatures, and coolant flow behaviour. These analyses are important under normal operating conditions, as well as during transients and accident scenarios. To support this, a range of computational tools, such as system codes, sub-channel analysis codes, and CFD simulations are employed to model thermal-hydraulic behaviour with varying degrees of resolution and fidelity.

2.2.1 System codes

System codes are numerical simulation tools used to analyse the behaviour of nuclear reactor systems under various operational conditions. System codes were first introduced in the early 1960s to predict the overall behaviour of nuclear power plants under different operational scenarios. Such codes typically involve lumped (0D) or one-dimensional (1D) flow representations, empirical correlations, and engineering approximations for heat transfer and pressure drop. Their primary purpose is to support reactor safety assessments, design optimization, and licensing processes by predicting key parameters such as temperature, pressure, and flow distribution.

Over the past few decades, system codes have undergone significant advancements, improving their ability to model a wide range of physical phenomena in reactor systems. Some of the most well-known system codes include RELAP5, TRAC, and ATHLET, which were developed for specific reactor designs and are widely recognized as best-estimate system codes. These tools are extensively used for thermal-hydraulic analysis in both research and industry [143, 18].

Although they have been extensively developed and are used widely, traditional system codes are primarily 0D/ 1D. They cannot account for small-scale turbulence and local flow variations which limits their ability to capture complex three-dimensional (3D) flow phenomena. Validation of the codes against large-scale phe-

nomena is essential to ensure the accuracy and reliability of the predictions. Many researchers, including Sabundjian et al. [[106]], D'Auria et al. [32], and Misale et al. [93], have validated RELAP5 using experimental data obtained from scaled-down test facilities. Additionally, benchmarking exercises conducted by Martin et al. [89] have demonstrated that RELAP5/MOD3 can reasonably predict forced flow behaviour in vertical channels.

Furthermore, multi-dimensional thermal-hydraulic system codes have been developed, incorporating advanced modelling techniques to improve fidelity. One example is the MARS 1.3.1 code, developed by Jeong et al. [61], which integrates features from RELAP5, a 1D system code, and COBRA-TF, which incorporates a 3D hydrodynamic model to enhance the simulation of multi-dimensional flow effects. These improvements mark a significant step toward increasing the predictive capability of system codes, making them more suitable for advanced reactor safety analysis and design.

System codes reached a high level of advancement after decades of refinement, and are now widely used for thermal-hydraulic analysis of nuclear reactor systems. Although system codes have demonstrated considerable success, further improvements in accuracy and standardization of validation procedures remain important challenges. Currently, validation and qualification approaches vary across different regulatory organizations, and international standardization has yet to be fully achieved. Several international bodies, such as the OECD, CSNI, OECD/NEA, and IAEA [80, 51, 57, 112], have systematically evaluated system codes to enhance their accuracy and reliability for nuclear safety applications.

2.2.2 Sub-channel analysis codes

System codes, as discussed in the previous section, provide reliable predictions of the overall thermal-hydraulic behaviour of nuclear power plants under various steady-state and transient conditions. However, for more detailed analyses, results from system codes often serve as boundary conditions for localized core or fuel-channel simulations, which are traditionally performed using sub-channel codes[94]. These sub-channel codes solve the conservation equations for mass, momentum, and energy across discretized groups of flow channels, enabling them to estimate key safety parameters, such as Critical Heat Flux Ratio (CHFR), Critical Power Ratio (CPR), centreline fuel temperature, cladding surface temperature, and coolant temperature distribution. It divides the reactor core or the fuel channel/bundle into sub-channels,

representing the flow regions surrounding and between fuel rods, simplifying the complex interactions within the core.

Sub-channel codes solve the mass, momentum, and energy conservation equations using a 1D framework, where control volumes are connected both radially and axially to partially account for 3D flow effects [94]. To close the governing equations, these codes rely on empirical correlations for pressure drop, heat transfer, and turbulent mixing, derived from experimental data. While this approach enhances computational efficiency and allows for rapid analysis, the 1D formulation limits the ability to resolve complex 3D flow structures, localized turbulence, and secondary flow effects.

As illustrated in Figure 2.4, the fuel channel can be visualized as a repeated geometric arrangement consisting of both coolant-centred and rod-centred sub-channels. This representation is fundamental in the development of sub-channel codes and serves as a critical framework in experimental research aimed at improving thermal-hydraulic modelling.

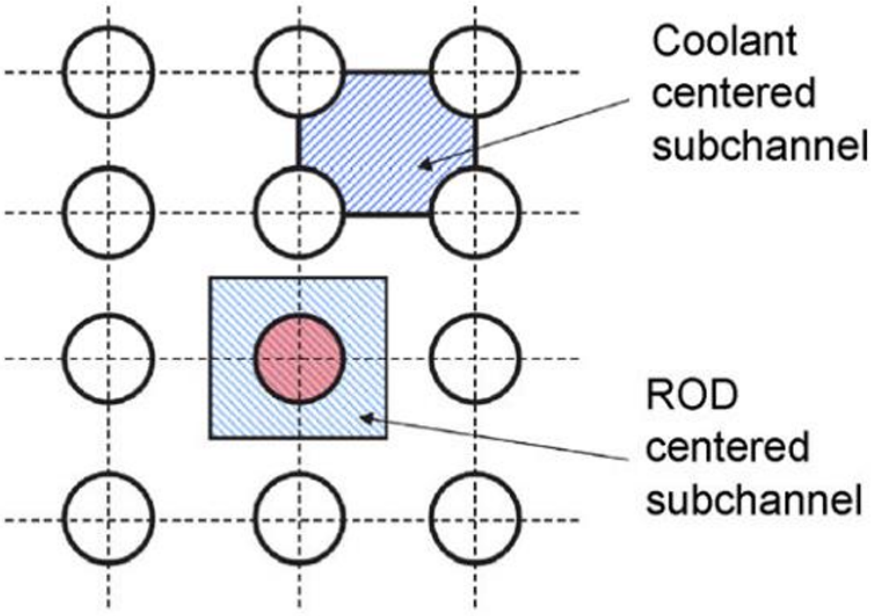

Figure 2.4: Illustration of the sub-channel concept [94].

Significant research efforts have focused on developing sub-channel codes for various reactor types to effectively predict the thermal-hydraulic behaviour of reactors. For PWRs, the COBRA series of codes was created by the Pacific Northwest Laboratory (PNL) in the USA[34]. This series includes COBRA-I, COBRA-II, COBRA-III, COBRA-IIIC, and COBRA-IV. The early versions, COBRA-I and COBRA-II, were

limited to steady-state simulations because they did not account for transient momentum effects. Later, COBRA-III, developed by Rowe[105], introduced the ability to predict transient flow behaviour; however, it lacked heat transfer models and could only calculate pressure gradients. To overcome this limitation, COBRA-IIIC [105] and COBRA-IV [129] were further developed to incorporate heat transfer models, enabling more accurate thermal predictions.

In addition to the COBRA series, several other sub-channel codes have been developed. Chaudri et al. [24] introduced the Steady and Transient Analyser for Reactor thermal-hydraulics (START), which uses a homogeneous model to simulate both steady and transient conditions in PWRs with two-phase flow. Later, Yoo et al. [34] developed MATRA, an efficient sub-channel code capable of predicting enthalpy and flow distributions in both PWRs and Advanced Light Water Reactors (ALWRs) under steady and transient conditions.

As next-generation nuclear reactors advance, new sub-channel codes have been developed to address their distinct thermal-hydraulic characteristics. Deng et al. [35] created a sub-channel code specifically designed for lead-cooled fast reactors, which are part of the Generation IV reactor concept. Their model featured both grid spacers and wire spacers to more accurately capture coolant flow behaviour. Similarly, Liu et al. [87] expanded the COBRA-IV framework to develop COBRA-LM, tailored for liquid metal-cooled fast reactors (LMFRs). Validation studies showed that the predicted coolant and fuel cladding temperatures closely aligned with both experimental data and CFX simulation results.

For SCWRs, Shan et al. [110] developed the ATHAS sub-channel code. This code includes empirical correlations for heat transfer and friction factors under supercritical conditions, which allows for accurate predictions of fuel cladding temperature and coolant enthalpy distribution. Notably, ATHAS is suitable for both steady-state and transient scenarios, making it a versatile tool for thermal-hydraulic simulations of SCWRs.

In summary, while sub-channel codes are highly effective for reactor safety assessments and operational predictions, their inherent limitations due to the nature of 1D representation require the use of higher-fidelity Computational Fluid Dynamics (CFD) models when a detailed understanding of 3D flow physics is necessary.

2.2.3 Computational Fluid Dynamics (CFD)

System codes and sub-channel codes provide reasonable predictions of nuclear power plant thermal-hydraulic behaviour at the system level and core level, respectively.

However, their effectiveness is limited when resolving detailed sub-scale flow physics, such as localized turbulence, flow separation, and small-scale mixing effects. The significant advancements in computational power over recent decades have enabled the application of CFD as an advanced tool for investigating complex coolant flow phenomena in nuclear fuel channels. Unlike system codes or sub-channel codes, which rely on simplified models and empirical correlations, CFD offers a high-fidelity approach by solving the Navier-Stokes equations directly or through turbulence models. This enables a more detailed resolution of local flow structures, boundary layer effects, and transient behaviours. [94].

In nuclear reactor thermal-hydraulics, particularly for SCWRs, CFD is an essential tool for predicting fluid behaviour. It captures strong buoyancy effects, variable property changes near the pseudo-critical point, and complex flow interactions, providing deeper insight into heat transfer and flow behaviour. As shown in Figure 2.5, CFD approaches vary in their level of physics resolution and computational cost, ranging from Reynolds-Averaged Navier-Stokes (RANS) models, which approximate turbulence effects and offer the most computationally efficient solution, to Direct Numerical Simulation (DNS), which fully resolves all turbulence scales and stand out as high-fidelity numerical experiments to provide detailed insight into the underlying flow physics. But it is excessively costly for reactor-scale applications. Large Eddy Simulation (LES) provides an alternative by resolving larger turbulent structures while modelling only the smallest scales, achieving a balance between accuracy and computational requirements. Hybrid RANS/LES methods combine the advantages of both techniques, employing LES in essential flow areas and RANS in other regions to enhance efficiency, making them an appropriate choice for complex flow simulations in nuclear reactor applications.

CFD can be used to optimize reactor designs, improve safety evaluations, and enhance efficiency predictions, complementing lower-order modelling approaches such as system and sub-channel codes. Selecting an appropriate CFD approach is crucial to balancing computational feasibility and accuracy.

For the application of CFD, as the demand for detailed physical insights in reactor design and safety assessments continues to grow, CFD has become an essential tool for simulating various nuclear reactor components, including single channels [31, 48], multiple channels [25, 85], rod bundles [1, 16], reactor core sectors [111, 118], and plenum [66, 65]. A variety of CFD approaches have been applied, including RANS [23], Unsteady Reynolds-Averaged Navier-Stokes (URANS) [91], LES [12], and DNS [11]. For RANS and URANS, commonly used turbulence models include

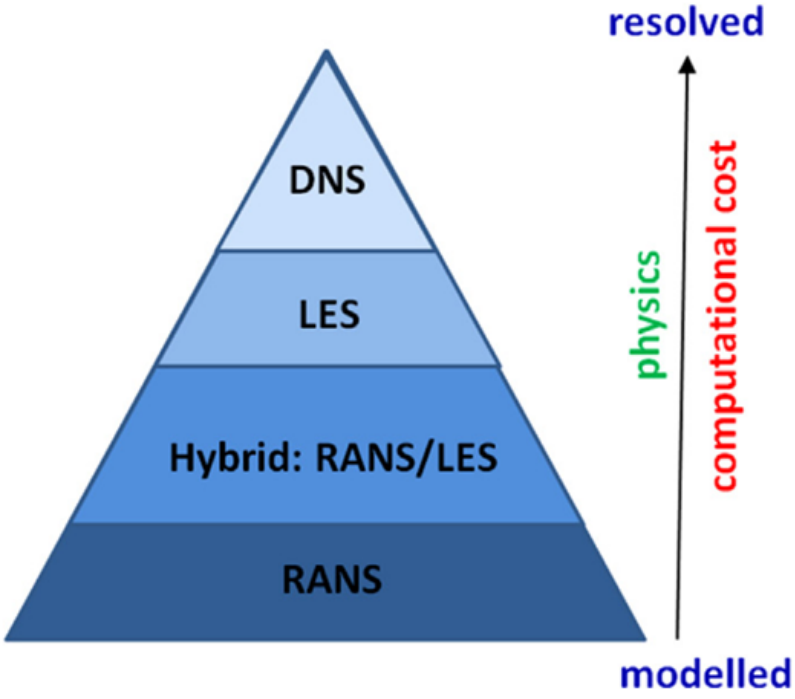

Figure 2.5: Computational cost and the level of physics resolution [104].

the k-ε model [10] though k-ω SST has been more and more widely used.CFD has also been utilized to study different reactor types, such as PWRs [29], SCWRs [45], and LMFBRs [42].

A key advantage of CFD is its ability to resolve near-wall flow characteristics, particularly within the viscous sublayer [83]. This is achieved by employing highly refined meshes in the near-wall region, ensuring an appropriate y^+ value when using low-Reynolds-number turbulence models. Typically, $y^+ \approx 1$ is required for wall-resolved simulations, while wall functions allow for coarser grids, reducing computational costs. However, achieving high-resolution CFD simulations demands substantial computational resources, as finer meshes are required to capture small-scale turbulence structures and detailed thermal-hydraulic effects.

CFD has demonstrated the capability to provide detailed flow and thermal field predictions with relatively minimal reactor-specific adjustments. However, due to its high computational cost, CFD cannot fully replace system codes or sub-channel codes. Instead, CFD is best suited for resolving localized flow phenomena, offering high-fidelity insights that complement traditional thermal-hydraulic analysis methods. While CFD continues to evolve with advances in computational efficiency and turbulence modelling, its practical implementation in full-core reactor simulations

remains constrained by computational limitations. Future research should focus on hybrid modelling approaches, high-performance computing, and improved turbulence closures to enhance CFD's applicability in nuclear reactor thermal hydraulics.

2.2.4 Coupling methods

As discussed in previous sections, system codes, sub-channel codes, and conventional CFD each have distinct advantages and limitations. System codes investigate the thermal-hydraulic behaviour over the entire reactor, while sub-channel codes enhance resolution at the core level. CFD, on the other hand, offers high-fidelity insights into localized flow phenomena. To utilize the strengths of these different approaches and minimize their drawbacks, various coupling strategies have been developed. The implementation of coupling can vary depending on the modelling objectives and the numerical tools used.

At the system level, CFD can be integrated with system codes to enhance the accuracy of specific regions that exhibit complex 3D flow phenomena. For example, Toti et al. [117] developed and validated a coupling approach between the CFD software ANSYS FLUENT and the system code RELAP5-3D, specifically for liquid metal types of reactors. Their method demonstrated considerable accuracy in analysing safety margins and showed reliable agreement with experimental data for a loss-of-flow transient scenario.

Similarly, Bertolotto et al. [14] investigated mixing phenomena in a LWR by coupling the system code TRACE with the CFD software CFX. Another noteworthy study by Anderson et al. [6] performed a thermal-hydraulic analysis of a Very High Temperature Reactor (VHTR) by integrating RELAP5-3D with CFD. In these coupling approaches, system codes conduct global reactor calculations, while CFD is applied to regions where system codes struggle to accurately capture complex 3D effects, such as outlet plena and mixing zones. By combining these methodologies, researchers achieve improved predictive capabilities while managing reasonable computational costs.

The geometry of a nuclear reactor core is highly complex, consisting of many fuel assemblies, each containing hundreds of fuel rods, which in turn create tens of hundreds of flow channels. Running full-core CFD simulations can be extremely demanding in terms of computational resources, making alternative coupling strategies necessary for reactor-level analysis. One effective approach involves coupling porous media models with CFD codes, as explored in previous studies[27, 40]. This

method enables efficient core-scale modelling by using the porous media approximation for bulk flow while applying detailed CFD to selected regions to capture finer-scale physics. Zhang et al. [142] applied a porous media approach to represent the PWR reactor core. The detailed rod bundle geometry was replaced with a distributed resistance model, implemented as momentum source terms in the CFD simulation. This method accounted for geometric, frictional, and permeability-based losses, effectively modeling the core as a porous region to reduce computational cost while preserving the essential pressure drop characteristics.

Alternative coupling techniques have been proposed to improve thermal-hydraulic analysis at the reactor level. Corzo et al. [30] developed a hybrid method that combines a 1D finite-volume code with CFD model specifically for a Pressurized Heavy Water Reactor (PHWR). In their approach, the 1D solver models the behaviour of the fuel channels, while the 3D model captures complex flow phenomena in areas such as the upper and lower plenum.

Coupling methods provide a practical solution to the limitations of system codes, sub-channel codes, and conventional CFD. By integrating CFD with lower-order models, researchers can achieve higher accuracy in critical areas while maintaining computational efficiency for large-scale reactor simulations.

2.2.5 Coarse Grid CFD

Alongside integrating low-cost simulation methods with CFD, another promising development in thermal-hydraulic analysis tools is the application of coarse-grid CFD. This technique has shown the capability to deliver high-quality results while notably lowering computational expenses. Coarse grid CFD methods utilize traditional CFD solvers combined with specialized techniques, enabling the use of a coarse mesh while still achieving acceptable accuracy in predictions.

One of the early advancements in this field is the Low-Resolution Geometry Resolving (LRGR) CFD method, proposed by Roelofs et al. [103]. This method employs a coarse-resolution mesh while still effectively capturing significant large- and medium-scale flow features in fuel channels, such as recirculation zones, which are often difficult to predict using system codes or sub-channel codes. Unlike traditional CFD, which requires high grid resolution to capture all flow features, LRGR CFD strategically reduces mesh refinement while preserving critical flow structures that influence overall thermal-hydraulic behaviour. The effectiveness of LRGR CFD with coarse meshes is primarily due to the dominance of axial flow in heat transport, meaning that fine-scale turbulence details, such as secondary flows, have a limited

impact on overall temperature distribution. By neglecting small-scale turbulence and localized flow variations, this method reduces computational cost while still providing accurate temperature and bulk flow predictions. However, since it does not resolve small-scale turbulence or cross-flow effects, it is best suited for analysing global flow behaviour, blockage effects, and large-scale recirculation patterns rather than fine-scale turbulence-driven phenomena.

Hu and Fanning [53] developed a three-dimensional momentum source model (MSM) that enables coarse-mesh CFD simulations of wire-wrapped rod bundles without explicitly resolving the wire geometry. Instead, volumetric body forces are introduced to represent the effects of the wire-wrap spacers, including flow blockage, induced swirl, and friction. These momentum sources depend on local flow velocity and geometry, allowing accurate prediction of crossflow and pressure drop on a significantly coarser mesh, thereby reducing computational cost while preserving key flow characteristics.

Bieder et al. [15] employed a low-resolution CFD approach to simulate the thermal-hydraulic behaviour of a wire-wrapped rod bundle in LMFBR fuel assembly. To enable the use of a coarse mesh, they simplified the model by reducing the number of computational cells, particularly near solid walls, and applied wall functions to approximate near-wall flow behaviour instead of resolving the boundary layers explicitly.

Viellieber and Class [120] introduced a thermal-hydraulic simulation methodology known as Coarse-Grid CFD (CG-CFD), which aims to enable full-core reactor simulations with significantly reduced computational effort. Unlike subchannel analysis, CG-CFD does not rely on empirical correlations; instead, it solves the Euler equations on a coarse mesh and incorporates volumetric source terms, representing turbulence and viscous effects, that are pre-computed from high-fidelity CFD simulations of representative subdomains. These source terms are then parameterized and applied throughout the coarse grid domain, allowing the method to capture key flow features without resolving fine-scale structures. Although CG-CFD may require a large number of initial detailed CFD runs for source-term generation, it enables the simulation of complex geometries, such as full-core rod bundles, at a fraction of the computational cost of full-resolution CFD. Moreover, by embedding physical behaviour derived from resolved simulations, it is less dependent on empirical inputs compared to traditional subchannel codes. This methodology offers an advantageous balance between accuracy and efficiency in large-scale thermal-hydraulic analyses.

2.2.6 Sub-channel CFD (SubChCFD)

A novel coarse-grid CFD approach, named Sub-channel CFD (SubChCFD), was proposed by Liu et al. [83] to integrate the strengths of sub-channel methods and CFD methodologies. SubChCFD is implemented within a conventional CFD solver while utilizing a coarse mesh to significantly reduce computational cost. Similar to other coarse mesh CFD approaches, closure modelling is required in SubChCFD to account for wall effects. The potential accuracy loss due to the coarse resolution is compensated through the implementation of well-validated sub-channel correlations to model wall friction and heat transfer. By leveraging these correlations, SubChCFD can maintain the accuracy of integral thermal-hydraulic behaviour predictions, even with a reduced computational resolution.

The initial development and validation of this method were presented by Liu et al. [83], where the thermal-hydraulic predictions of SubChCFD were compared against both high-resolution CFD results and experimental data. The study demonstrated that SubChCFD provides reasonable predictions of global and local flow characteristics in fuel channels while significantly reducing the computational cost. Specifically, the study was for a 5×5 bare bundle case based on the OECD/NEA MATiS-H benchmark. The case involved fully developed turbulent flow in a PWR rod bundle, with water at an operating pressure of 1.5 bar and a bulk velocity of 1.5 m/s, corresponding to a Reynolds number of 50250. A uniform heat flux of 200 kW/m^2 was applied to evaluate heat transfer performance. The SubChCFD simulation used a significantly coarser mesh of 1120 cells, compared to 54528 cells in the conventional CFD model, enabling substantial computational savings. SubChCFD required only 1/60th of the computational time per time step compared to conventional CFD. However, this efficiency gain is case-dependent and varies based on the specific flow conditions and mesh configuration.

To further assess the applicability of SubChCFD in non-design operating conditions, Liu et al. [83] investigated local blockage scenarios in a 5×5 rod bundle, where a partial obstruction was introduced in one of the sub-channels. This blockage caused significant flow redistribution, localized pressure losses, and enhanced inter-channel mixing, making it a challenging test for coarse-grid CFD methods. The results showed that SubChCFD could accurately capture form loss effects in the blocked region, predicting the pressure drop and lateral flow redistribution with reasonable accuracy compared to resolved CFD. This demonstrated SubChCFD's potential for complex thermal-hydraulic simulations beyond nominal operating conditions.

To enhance the predictive capability of SubChCFD, further developments have been explored by coupling it with other CFD-based methods. In one approach, SubChCFD was coupled with embedded resolved CFD sub-models to refine simulations and improve accuracy in selected regions of interest[83]. Another study integrated SubChCFD with a porous media approach, expanding its modelling flexibility and increasing its ability to handle sub-scale flow structures [84].

While previous studies have demonstrated the potential of SubChCFD, further development and refinement remain necessary to extend its applicability to supercritical pressure conditions and complex thermal-hydraulic phenomena. A number of areas of study have been identified for the topics for this PhD research. The first topic involves improving heat transfer modelling, particularly for mixed convection in supercritical fluids, where incorporating improved Nusselt number correlations and buoyancy corrections can enhance prediction accuracy. The second topic is the modelling of the influence of wire-wrapped spacers in the SubChCFD framework, which is important to accurately capture the secondary flow effects introduced by these structures. In addition to these developments, extending the capability of SubChCFD to predict NCL behaviour has been selected as a useful development for SubChCFD. This effort is useful for demonstrating the flexibility and potential of SubChCFD to handle complex geometries and flow conditions, such as those encountered in passive cooling systems.

2.3 Mixed convection in supercritical scenario

2.3.1 Physics overview of mixed convection

Mixed convection occurs when the flow is influenced by both forced convection and buoyancy-driven natural convection [63]. This condition arises when the buoyancy force is equivalent to or exceeds the inertial force, causing flow disturbances that can either enhance or reduce heat transfer performance.

The influence of buoyancy in mixed convection depends on the interaction between forced flow and gravity-driven effects. In a laminar flow, the influence of buoyancy is relatively straightforward. When the buoyancy force acts in the same direction as the main flow (buoyancy-aided flow, i.e., heated upwards flow or cooled downward flow), it accelerates the near-wall fluid, enhances advective transport, and improves heat transfer performance. Conversely, in buoyancy-opposed flow, such as heated fluid flowing downward, the buoyancy force resists the main flow direction. This slows

the near-wall fluid, reduces advection, and leads to deterioration in heat transfer compared to forced convection.

In turbulent flow, however, buoyancy not only affects the mean velocity but also significantly modifies turbulence production and structure. In buoyancy-opposed turbulent flow (e.g., downward heated flow), the upward buoyant force increases the near-wall velocity gradient, enhancing shear stress and promoting turbulence production. This leads to stronger turbulent diffusion and improved heat transfer. In contrast, in buoyancy-aided turbulent flow (e.g., upward heated flow), the buoyancy force flattens the velocity profile near the wall (except right next to the wall where the velocity gradient is increased but this does not affect turbulence production), thereby reducing shear stress and suppressing turbulence production. As a result, turbulent mixing weakens, and heat transfer deteriorates. [68]

This behaviour is illustrated in Figure 2.6, which shows the evolution of turbulent shear stress distributions across the pipe radius with increasing buoyancy influence. In an upward flow, turbulent shear stress near the wall progressively declines with increasing buoyancy, leading to laminarization. With even stronger buoyancy, turbulence can recover, resulting in improved heat transfer. In contrast, downward flow shows enhanced turbulent shear as buoyancy increases, improving heat transfer.

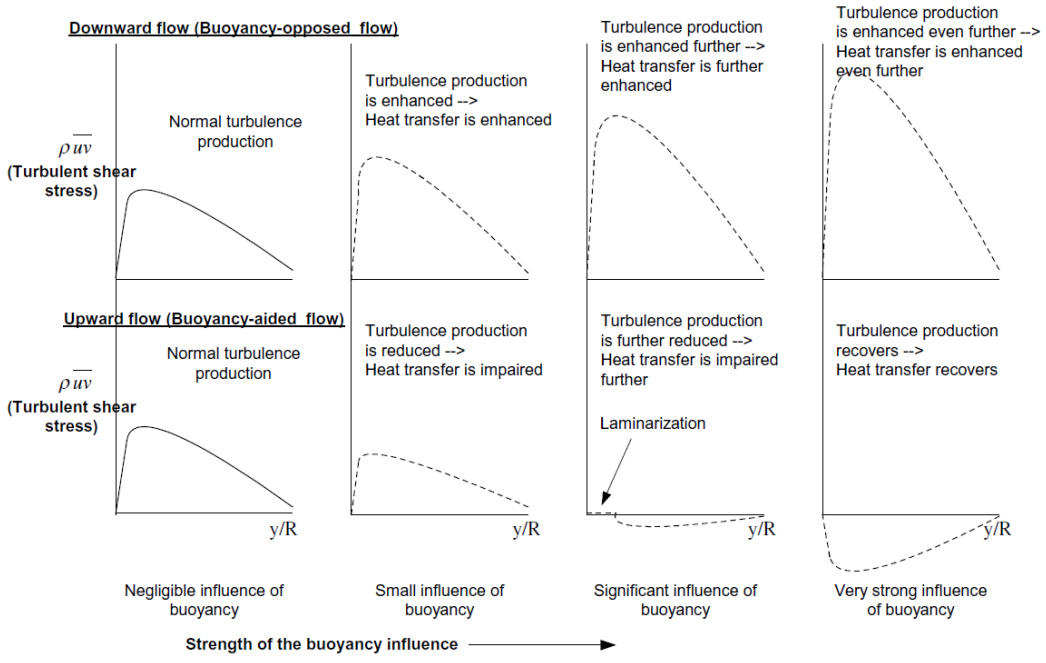

Figure 2.6: Evolution of turbulent shear stress distributions for upward (buoyancy-aided) and downward (buoyancy-opposed) flows with increasing buoyancy influence [68]

The effect of buoyancy on heat transfer can be observed in Figure 2.7 [59]. The plot shows the Nusselt number ratio (Nu_b/Nu_{b0}) as a function of a buoyancy parameter. This figure complements the earlier discussion of turbulent shear stress by linking the changes in flow behaviour directly to thermal performance.

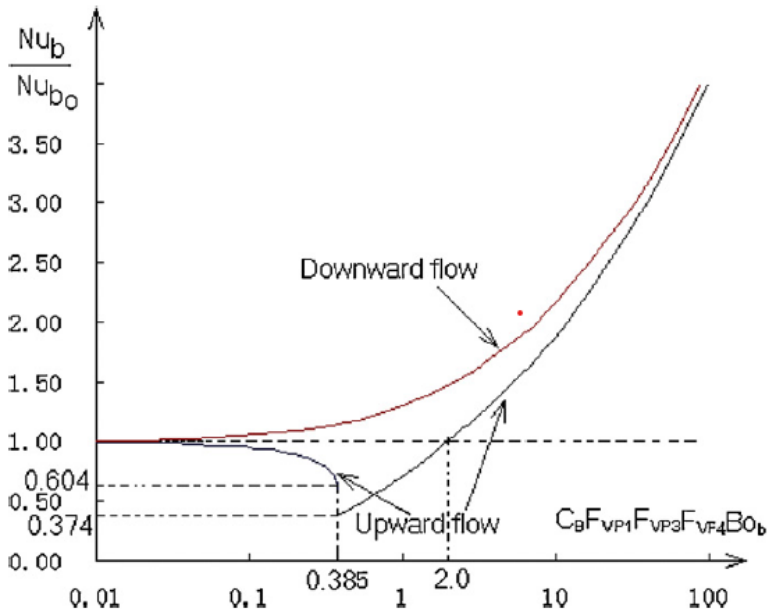

Figure 2.7: Effect of buoyancy on heat transfer for upward and downward flows [59].

For downward flow, buoyancy effect enhances near-wall shear stress and promoting turbulence production. As a result, heat transfer performance improves steadily with increasing buoyancy, with Nu_b/Nu_{b0} consistently above unity.

In contrast, upward flow shows a more complex trend. Initially, as buoyancy increases, turbulence is suppressed due to reduced wall shear stress, leading to laminarization near the wall and a significant drop in heat transfer performance. This results in a region of heat transfer deterioration, where Nu_b/Nu_{b0} drops below one. As the buoyancy effect becomes stronger, it leads to a recovery and eventual enhancement of heat transfer at higher buoyancy levels.

Understanding mixed convection is important in engineering applications such as nuclear reactor cooling systems, high-performance heat exchangers, and atmospheric flow analyses. In the context of nuclear reactors, mixed convection is relevant in SCWRs. It is particularly important due to significant variations in thermal physical properties and strong buoyancy effects resulting from large density gradients near the pseudo-critical point, resulting in complex heat transfer behaviour that needs to be carefully considered during reactor design and analysis. [2] As a result, extensive

research has been conducted to investigate mixed convection in vertical tubes, annular geometries, and fuel channels, both experimentally and numerically [101, 82].

Relevant experimental studies, numerical modelling and empirical correlation developments are present in the following sections.

2.3.2 Experimental studies

Experimental studies have played a crucial role in understanding heat transfer under supercritical pressure conditions. Researchers have conducted extensive investigations to explore the influence of buoyancy, turbulence, and thermal property variations on heat transfer performance. These studies provide valuable insights for developing reliable thermal-hydraulic models and improving the design of SCWRs.

The experimental investigation of heat transfer under supercritical pressure dates back to the 1930s, with Schmidt et al. [107] conducting some of the earliest studies. Their research focused on free convection heat transfer in fluids near the critical point, where they observed that the heat transfer coefficient (HTC) reaches a peak value in the near-critical region, highlighting the significant impact of thermal physical property variations on heat transfer behaviour.

Subsequently, numerousus experimental studies investigated mixed convection in supercritical heat transfer. Yamagata et al. [137] examined heat transfer deterioration in the vertical tubes using water as the working fluid and found that strong buoyancy effects led to turbulence suppression, reducing heat transfer efficiency in upward flow. Yamagata et al. [137] observed a peak in the heat transfer coefficient appears at low heat flux conditions. However, as the heat flux increases, heat transfer deterioration sets in, resulting in a decline in heat transfer performance. Similar results are also noticed in Swenson et al.'s experiment [115].

Jackson and co-workers [60, 59] conducted experimental studies on heat transfer in supercritical fluids, primarily focusing on buoyancy effects in vertical heated tubes using carbon dioxide at near-critical pressures. His experiments revealed that in an upward flow, heat transfer deterioration occurred. In contrast, the downward flow exhibited a more stable heat transfer performance. As shown in Figure 2.8, a sharp localized peak in wall temperature is observed in upward flow. This sharp rise in temperature indicates heat transfer deterioration, primarily caused by buoyancy-induced laminarization. In contrast, downward flow does not exhibit this effect.

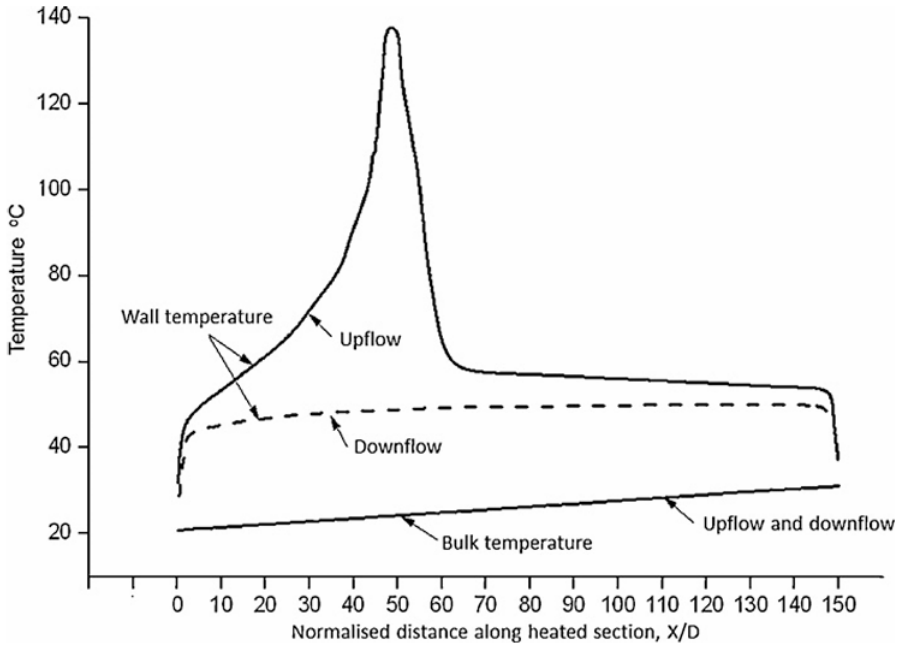

Figure 2.8: Localized deterioration of heat transfer [59].

Kirillov et al. [70] investigated the radial cross-sectional temperature profile of water flowing through a circular tube under subcritical and supercritical pressures. Their findings indicated that at supercritical pressures and temperatures near the pseudo-critical point, the temperature profile within the turbulent flow core follows a logarithmic distribution. Yoshida and Mori [140] observed that supercritical heat transfer is significantly influenced by rapid variations in thermophysical properties with temperature changes across the flow. These variations lead to a peak in the heat HTC near the pseudo-critical temperature at low heat flux. However, as the heat flux increases, the peak HTC diminishes, highlighting the impact of heat flux on supercritical heat transfer performance.

Experimental studies provide fundamental insights into supercritical heat transfer, particularly regarding HTD, buoyancy-driven laminarization, and thermal physical property variations. The results from historical and recent experiments demonstrate the importance of considering buoyancy effects and heat flux variations in developing accurate thermal-hydraulic models for SCWR applications. While this chapter presents only a selected set of experimental findings, it should be noted that an extensive body of experimental research has been conducted over the past several decades. For a more comprehensive overview, the reader is referred to the review by Rahman et al. [**?**], which summarises experimental efforts related to supercritical water heat

transfer. Experimental findings provide a foundation for further numerical simulations and the development of heat transfer correlations, which will be discussed in the following sections.

2.3.3 Numerical studies

In recent years, there has been growing interest in the numerical investigation of mixed convection heat transfer at supercritical pressures, motivated by the complexity of the fundamental physical phenomena. A major challenge is present in accurately capturing these phenomena, such as strong variations in thermal physical properties near the pseudo-critical point, buoyancy-induced flow instabilities, and the occurrence of heat transfer deterioration. CFD has been widely used to examine velocity distributions, turbulence intensity, and thermal performance under supercritical conditions. Numerical studies in this area are generally categorized into RANS, LES, and DNS, each offering different levels of accuracy and computational cost. Numerous studies also incorporate validation with experimental data and highlight the significance of buoyancy effects and variations in thermal physical properties in influencing heat transfer performance [97].

Kasagi and Nishimura [67] conducted one of the earliest DNS studies on mixed convection, focusing on how buoyancy affects Reynolds stress distributions. By using DNS, they were able to gather more detailed information about turbulence flow characteristics compared to what is typically available from experimental research. Their findings showed that buoyancy-driven flow significantly influences shear stress and turbulence production, which results in heat transfer enhancement and heat transfer deterioration.

You et al. [141] conducted DNS of turbulent mixed convection in fully developed upward and downward air flows within a vertically heated tube, using the Boussinesq approximation and assuming constant fluid properties. In upward flow, their results showed that with increasing heat flux, the velocity near the wall initially decreased and then increased, a trend also observed in the skin friction and heat transfer coefficients. In contrast, for downward flow, both the velocity and skin friction remained nearly unchanged, while the heat transfer coefficient increased with rising heat flux. These findings highlight the significant impact of buoyancy direction on turbulence structure and thermal transport in mixed convection.

Bae et al. [9] extended previous studies by performing DNS of turbulent heat transfer in supercritical carbon dioxide flowing through vertical heated tubes, explicitly accounting for strong property variations near the pseudo-critical point. Both

upward and downward flows were considered to analyse the influence of buoyancy on turbulence and heat transfer behaviour. Their simulations captured key features such as HTD in upward flow, associated with turbulence suppression near the wall, and enhanced turbulence and heat transfer in downward flow.

In addition to the earlier DNS investigations, more recent studies by He et al. [49] performed direct numerical simulations of heated pipe flow at supercritical pressure and proposed a unified explanation for flow laminarisation. They showed that the effects of buoyancy, changes in fluid properties, and flow development could all be treated as similar to body forces. These forces reduce the effective Reynolds number and lead to turbulence suppression. Their study clearly described how turbulence first weakens, then disappears, and later reappears downstream. Similarly, Cao et al. [20] conducted DNS of supercritical CO_2 flows in heated micron-scale tubes, where the pressure drop along the flow direction becomes significant. They found that flow acceleration, combined with changes in thermal physical properties, had a strong impact on turbulence and heat transfer performance. Together, these studies provide a detailed understanding of turbulence development under supercritical conditions.

Within the RANS framework, early studies employed simple eddy viscosity models, where turbulent viscosity was calculated using basic algebraic equations. Although these models lacked high accuracy, they offered valuable qualitative insights into the heat transfer mechanisms at supercritical pressure. Recent advancements in computational power have increased the use of refined turbulence models in numerical studies.[101] Koshizuka et al. [71] carried out a numerical analysis on heat transfer deterioration in a vertical tube by employing a low-Reynolds-number k-ε model. The findings were compared with experimental data from Yamagata et al. [137], and the results showed good agreement between them. In later study, Kim et al. [108] evaluated over ten first-order closure turbulence models and concluded that the RNG k-ε model yielded the most accurate predictions for supercritical heat transfer. Gu et al. [45] investigated HTD using six low-Reynolds-number turbulence models: Abe–Kondoh–Nagano (AKN), Chien–Hsieh–Chen (CHC), Abe–Basley–Inagaki–Durbin (ABID), Yang–Shih (YS), v^2–f, and Shear Stress Transport (SST). Their results showed that all models captured the effects of buoyancy reasonably well, but the v^2–f and SST models demonstrated superior performance in predicting the onset of HTD. Further assessment was conducted by He et al. [50], who compared several low-Reynolds-number RANS models against DNS data for supercritical carbon dioxide flow in vertical heated tubes. They found that models with damping functions highly sensitive to buoyancy and flow acceleration—such as the Launder–Sharma (LS), YS,

and AKN models—tended to over predict turbulence suppression. This resulted in an exaggerated prediction of flow laminarization and, consequently, heat transfer deterioration. In contrast, the v^2–f model and other models with less responsive damping functions more accurately predicted wall temperature profiles and turbulence recovery, with the v^2–f model showing the best overall agreement with DNS data. As v^2–f model can handle the near wall physics more realistically.

Numerical studies have played a critical role in advancing the understanding of mixed convection heat transfer under supercritical conditions. In particular, they have clarified the influence of buoyancy on turbulence behaviour and the mechanisms leading to heat transfer deterioration. These studies have provided valuable data that inform the development and refinement of heat transfer correlations, which will be discussed in the following section. We have to note that there is a huge body of literature on numerical studies of heat transfer to supercritical fluids and the above review only serves an illustration of the capabilities and contributions of numerical studies on this topic. Across studies, a consistent picture emerges: buoyancy, especially near the pseudocritical region, near-wall turbulence reduction under heating and, together with strong acceleration, triggers heat transfer deterioration, acceleration parameters, and proximity to T_{pc} correlate with onset and recovery. Common future directions include standardizing HTD criteria across studies and building open high fidelity (LES/DNS) datasets for calibration.

2.3.4 Correlations development

Empirical correlations are important tools for estimating heat transfer in mixed convection flows, particularly under supercritical conditions. These correlations provide simplified mathematical expressions based on experimental results or high-fidelity simulation data. They allow for fast and practical estimation of key thermal-hydraulic parameters, such as heat transfer coefficients and friction factors, which are especially useful in engineering applications where detailed numerical simulations may be too computationally expensive. In addition, empirical correlations are widely used in the development of system codes and subchannel analysis tools, where efficient and reliable empirical correlations are necessary for simulating the thermal-hydraulic behaviour of nuclear systems.

The complex interactions between buoyancy and inertial forces have led many researchers to develop correlations that consider various parameters, including Reynolds number, Grashof number, Prandtl number, and heat flux. These correlations offer

powerful tools for the design and safety assessment of nuclear reactor systems, particularly SCWRs. Numerous empirical correlations have been developed to estimate the Nusselt number in mixed convection. These correlations are derived from both experimental and numerical studies to capture the key thermal-hydraulic effects [101].

The Dittus-Boelter equation [37] remains one of the most widely used empirical relations for convective heat transfer, given by:

$$Nu = 0.023 Re_b^{0.8} Pr_b^{0.4} \tag{2.1}$$

However, this equation does not account for the significant variations in properties that occur in supercritical fluids. To address these limitations, numerous researchers have modified classical correlations to include additional terms that capture the influence of buoyancy. Bishop et al. [17] developed an empirical correlation that includes a geometry factor to account for entrance effects.

$$Nu_b = 0.0069 Re_b^{0.9} Pr_b^{0.66} \left(\frac{\rho_w}{\rho_b}\right)^{0.43} \left(1 + 2.4\frac{D}{x}\right) \tag{2.2}$$

This correlation also includes a correction based on the wall-to-bulk density ratio, which reflects the impact of strong property variations near the pseudo-critical point. Similar correction factors, particularly involving the density ratio, are commonly used in empirical correlations.

In 2002, Jackson [58] refined previous models by developing an empirical correlation for forced convection heat transfer at supercritical pressure. This correlation is based on the work of Krasnoshchekow and Protopopov [73]. The model takes into account variations in heat capacity near the pseudo-critical region by introducing a baseline Nusselt number (Nu_b). This baseline is then adjusted using multiplicative correction factors to account for additional effects.

$$Nu_b = 0.0183\,\mathrm{Re}_b^{0.82} Pr_b^{0.5} \left(\frac{\rho_w}{\rho_b}\right)^{0.3} \left(\frac{\bar{c}_p}{c_{pb}}\right)^n \tag{2.3}$$

$$\bar{c}_p = \frac{1}{T_w - T_b} \int_{T_b}^{T_w} c_p \, dT = \frac{h_w - h_b}{T_w - T_b} \tag{2.4}$$

$$n = \begin{cases} 0.4, & T_b < T_w \leq T_{pc} \text{ or } 1.2T_{pc} \leq T_b < T_w \\ 0.4 + 0.2\left(\frac{T_w}{T_{pc}} - 1\right), & T_b < T_{pc} < T_w \\ 0.4 + 0.2\left(\frac{T_w}{T_{pc}} - 1\right)\left[1 - 5\left(\frac{T_b}{T_{pc}} - 1\right)\right], & T_{pc} \leq T_b < 1.2T_{pc} \text{ and } T_b < T_w \end{cases} \tag{2.5}$$

To account for buoyancy effects in mixed convection, Jackson and Hall proposed a correction based on the dimensionless buoyancy parameter Bo^*. Their model relates the ratio of the Nusselt number for mixed convection (Nu) to that for forced convection (Nu_f) which is also Nu_b mentioned in the early equations to the buoynacy parameter (Bo^*) through an implicit equation. There are a number of versions of the correlation, and here we use one established in Li and Jackson [82]:

$$\frac{Nu}{Nu_f} = \left\| 1 \pm 2.5 \times 10^5 \, Bo^* \left(\frac{Nu}{Nu_f} \right)^{-2} \right\|^{0.46}. \tag{2.6}$$

In this expression, Nu represents the heat transfer under mixed convection conditions, while Nu_f corresponds to the heat transfer predicted from forced convection alone (such as from Jackson's correlation). The $+$ or $-$ sign is used depending on whether buoyancy aids or opposes the main flow direction, respectively. The buoyancy parameter (Bo^*) is a dimensionless quantity that quantifies the relative impact of buoyancy forces in the system and is defined as:

$$Bo^* = \frac{Gr^*}{\mathrm{Re}^{3.425}\,\mathrm{Pr}^{0.8}}, \tag{2.7}$$

where the Grashof number (Gr^*) is given by:

$$Gr^* = \frac{\beta g D^4 q_w}{\lambda \nu^2}. \tag{2.8}$$

In these equations, Gr^* is expressed as a function of applied heat flux (q_w), rod diameter (D), and some fluid properties. β is the thermal expansion coefficient, and g is the gravitational acceleration. λ denotes the thermal conductivity, and ν is the kinematic viscosity. The Prandtl number (Pr) characterizes the ratio of momentum diffusivity to thermal diffusivity, playing a crucial role in defining thermal transport characteristics. The correction (equation 2.6) captures the enhancement or deterioration of heat transfer due to buoyancy effects.

Cheng et al. [28] introduced a dimensionless parameter, known as the acceleration parameter (π_A), to represent the influence of flow acceleration in supercritical fluids. This acceleration arises from strong density gradients along the flow direction, particularly near the pseudo-critical point. The parameter is defined as:

$$\pi_A = \frac{\beta}{c_p} \cdot \frac{\rho}{G} \tag{2.9}$$

where β is the thermal expansion coefficient, c_p is the specific heat, ρ is the fluid density, and G is the mass flux. A high π_A value indicates strong acceleration effects

due to thermal expansion. Based on this parameter, Cheng proposed a correction to the classical Dittus–Boelter correlation to account for the acceleration effect:

$$F = \frac{Nu}{0.023 Re^{0.8} Pr^{1/3}} = f(\pi_A) \tag{2.10}$$

The correction factor F is defined by a piecewise function, with the final form:

$$F = \min(F_1, F_2) \tag{2.11}$$

$$F_1 = 0.85 + 0.776(\pi_A \times 10^3)^{2.4} \tag{2.12}$$

$$F_2 = \frac{0.48}{(\pi_{A,PC} \times 10^3)^{1.55}} + 1.21 \left(1 - \frac{\pi_A}{\pi_{A,PC}}\right) \tag{2.13}$$

This formulation avoids direct reliance on wall temperature, which enhances numerical stability and allows the correlation to be applied consistently across both normal and deteriorated heat transfer conditions.

Zhao et al. [144] further extended this approach by introducing the buoyancy parameter (π_B), which captures the influence of density gradients in the radial direction and is defined as:

$$\pi_B = \frac{\rho \beta D}{k} \tag{2.14}$$

where D is the tube diameter and k is the thermal conductivity. This parameter quantifies the effect of buoyancy forces on flow and turbulence structure. Based on experimental data for downward supercritical water flow, Zhao proposed a modified correlation:

$$Nu = 0.023 Re^{0.8} Pr^{1/3} \cdot F \tag{2.15}$$

$$F = \min(F_1, F_2) \tag{2.16}$$

$$F_1 = 0.62 + 0.06 \cdot \ln(\pi_B) \tag{2.17}$$

$$F_2 = 11.46 \cdot [\ln(\pi_B)]^{-1.74} \tag{2.18}$$

In addition to heat transfer correlations, the prediction of frictional pressure loss is a critical component in thermal-hydraulic analyses. For turbulent flow in smooth pipes under isothermal conditions, the Blasius approximation [131] is widely used:

$$f = 0.316 \cdot \mathrm{Re}^{-0.25}, \quad \text{for } 4 \times 10^3 < \mathrm{Re} < 1 \times 10^5. \tag{2.19}$$

However, under supercritical conditions, the strong temperature dependence of fluid properties such as density and viscosity introduces non-isothermal effects that

influence wall shear stress and flow development. To address this, modified friction factor correlations have been proposed.

Kirillov [69] introduced a correction based on the density ratio between the wall and bulk fluid:

$$f_{\text{non-iso}} = f_{\text{iso}} \left(\frac{\rho_w}{\rho_b} \right)^{0.4}, \quad \text{for } 8 \times 10^4 < \text{Re} < 1.5 \times 10^6. \tag{2.20}$$

Similarly, Yamashita et al. [138] proposed a viscosity-based correction:

$$f_{\text{non-iso}} = f_{\text{iso}} \left(\frac{\mu_w}{\mu_b} \right)^{0.72}. \tag{2.21}$$

These corrections are designed to capture the influence of property variations in non-isothermal flows, particularly near the pseudo-critical point. While they do not explicitly account for buoyancy forces, the use of density or viscosity ratios can indirectly reflect some effects associated with strong thermal gradients.

The correlations presented in this section are selected examples from a wide range of models. While not comprehensive, they reflect key approaches used to account for effects such as property variation, flow acceleration and buoyancy. These correlations offer powerful tools for analysing thermal-hydraulic behaviour under supercritical conditions.

A comprehensive research for supercritical thermal-hydraulic analysis relies on the integration of experimental investigations, numerical simulations, and correlation-based approaches. Experimental studies reveal key thermal-hydraulic phenomena and provide high-quality benchmark data. Numerical simulations enable detailed analysis of flow dynamics, turbulence behaviour, and heat transfer mechanisms under complex conditions. Empirical correlations, derived from experimental and numerical findings, serve as reliable tools for engineering design and analysis.

2.4 Wire-wrapped rod bundle

2.4.1 Overview of wire-wrapped spacer geometry and function

The wire-wrapped rod bundle is a common configuration for fuel assemblies used in various advanced nuclear reactor designs such as the SCWR and LMFRs.(see Figure 2.9) [26]

The wire-wrap spacers maintain the rod bundle's geometric arrangement and improve heat transfer and fluid mixing within the flow domain [75]. Wire wraps create a

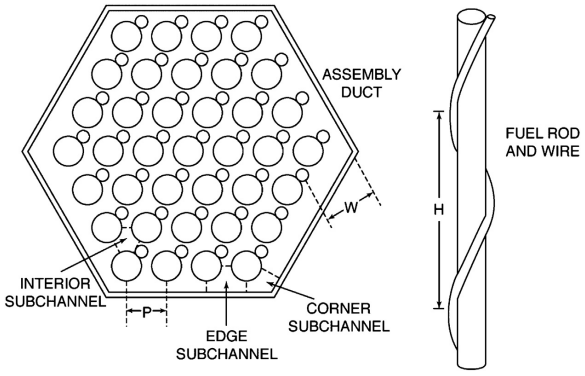

Figure 2.9: Wire-wrapped rod bundle schematic [26]

swirling motion in the coolant flow, which generates secondary flows that significantly impact heat transfer characteristics. These secondary flows enhance thermal mixing between adjacent subchannels, resulting in improved heat removal efficiency and a more uniform temperature distribution within the bundle. This helps reduce the risk of localized hot spots, which are among the major thermal-hydraulic concerns in SCWRs due to their potential to raise cladding temperatures. The use of wire wraps improves the safety margin by lowering peak cladding temperatures and producing a more uniform temperature distribution along the fuel rods [101].

In addition to enhancing axial heat transfer, wire wraps induce cross-flow between adjacent sub-channels, improving coolant redistribution. This lateral mixing enhances cooling performance and helps ensure a more uniform distribution of coolant across the fuel bundle. Overall, wire-wrapped spacers offer thermal-hydraulic advantages that contribute to safer and more efficient SCWR core designs.

Below, we review experimental and numerical research that explores the complex relationships among secondary flows, heat transfer enhancement, and pressure drop characteristics in wire-wrapped rod bundles. These studies offer valuable insights for optimising spacer designs and enhancing the overall efficiency and safety of SCWR fuel assemblies.

2.4.2 Experimental studies

The flow dynamics in wire-wrapped rod bundles are quite complex, and experimental studies are essential for investigating the underlying physical phenomena. They provide direct measurements of key parameters such as pressure drop, flow distribution, and heat transfer under realistic conditions. In addition to advancing physical understanding, experimental data also serve as important benchmarks for validating

CFD models. To support these efforts, specialized test facilities are developed to replicate the thermal-hydraulic conditions found in reactors employing wire-wrapped configurations.

Li et al.[81] conducted experimental research on heat transfer characteristics using a heated rod with a helically wrapped wire inside a square channel under supercritical conditions. Their results indicated that while the wire-wrap spacer had minimal impact on heat transfer under normal heat transfer conditions, it significantly enhanced heat transfer within the pseudo-critical region. The findings also revealed that, at lower supercritical pressures, the increased specific heat in the pseudo-critical region improved heat transfer, while higher pressures delayed the onset of heat transfer deterioration. Additionally, under strong buoyancy effect conditions, the wire-wrap spacer helped delay heat transfer deterioration, demonstrating its potential to improve the thermal performance of nuclear fuel assemblies.

Gang et al. [43] studied the heat transfer behaviour of supercritical water in annular channels equipped with wire-wrap spacers, focusing on the effects of heat flux and mass flux near the pseudo-critical region. A key observation from their study was the localised heat transfer enhancement induced by the spacers. The wire-wraps generated secondary flows that promoted coolant mixing and improved temperature uniformity, particularly under stronger buoyancy conditions. Specifically, the spacer effect was most pronounced at low mass fluxes (below 750 $kg/m^2 \cdot s$) and high heat fluxes (above 400 kW/m^2), where buoyancy effects became stronger and turbulence levels were insufficient. Under these conditions, supercritical flows are normally expected to have localised overheating and reduced heat transfer performance. However, the experimental results showed that wall temperatures remained relatively uniform near spacer locations, indicating that spacer-induced mixing effectively mitigated HTD. Gu et al.[44] conducted experiments using supercritical water in a 2 $\times$ 2 wire-wrapped rod bundle. They found that the wire wrap also enhanced heat transfer compared to a bare rod bundle under lower buoyancy effect conditions.

Wang et al.[124] investigated the circumferential temperature distribution in a 2 $\times$ 2 wire-wrapped rod bundle and found that the maximum wall temperature occurred in the narrow gap between the heated rod and the ceramic flow tube. In contrast, the lowest temperature was observed in the central sub-channel between the rods. The study reported that the circumferential temperature gradient was more pronounced in both low and high enthalpy regions, while it significantly decreased near the pseudo-critical enthalpy zone. Additionally, when compared to a bare rod bundle, the wire-wrapped configuration led to lower overall wall temperatures and significantly reduced

circumferential temperature gradients. This improvement is attributed to enhanced turbulence and mixing induced by the wire wraps, which promote more uniform heat transfer around the rod surface and help mitigate localized hot spots. In a later phase of the same study [54], the researchers also demonstrated that the presence of wire wraps affected the uniformity of circumferential wall temperatures. The wire wraps improved heat transfer, especially in the pseudo-critical region, by facilitating better thermal mixing and redistributing the flow.

Hu et al. [55] investigated the heat transfer performance of a 2×2 wire-wrapped rod bundle under supercritical conditions and found that the presence of wire-wrap spacers enhanced heat transfer. Specifically, the heat transfer coefficient was observed to be 8.4% higher compared to an equivalent bare rod bundle without spacers. This enhancement was attributed to the swirl flow induced by the helical wire-wrap, which promoted secondary flows and improved coolant mixing within the bundle.

2.4.3 Numerical studies

In recent years, numerical simulations have become a widely adopted tool for investigating cross-flow and heat transfer in wire-wrapped rod bundles. While traditional system and subchannel codes have been widely used to analyse wire-wrapped rod bundle configurations, their strength lies in evaluating overall thermal-hydraulic behaviour, such as average heat transfer rates and pressure drops at the bundle or core scale. However, due to their reliance on simplified models and empirical correlations, these tools have limited ability to resolve complex local flow phenomena, including vortices, swirl, and secondary flows induced by wire-wrap spacers. In contrast, CFD provides detailed resolution of the flow field. This allows for accurate prediction of 3D flow behaviour and local heat transfer characteristics, making CFD particularly valuable for studying the effects of spacer-induced mixing and anisotropic flow structures within wire-wrapped bundles.

Shan et al.[109] developed a sub-channel code for wire-wrapped SCWR rod bundles using the ATHAS in-house code. Their results indicated that wire-wrapped assemblies provide a more uniform coolant temperature distribution compared to scattered grid assemblies, which leads to lower peak cladding temperatures. Additionally, these wire-wrapped assemblies have a lower pressure drop than grid-attached configurations, potentially reducing the pump's power requirements. The study also emphasised the significant impact of wire-wrap pitch (the axial distance for one full turn of the helical wire around a rod) on flow behaviour; a smaller pitch enhances

cross-flow, promotes a more uniform coolant temperature distribution, and results in a higher pressure drop.

Fischer et al.[41] conducted LES to investigate the flow behaviour in a wire-wrapped fuel pin, applying periodic boundary conditions. Their results showed that cross-flow velocities displayed a sinusoidal pattern. These findings from the LES have since served as a reference dataset for validating turbulence modelling methods based on RANS simulations. In CFD simulations, it is crucial to balance computational cost and the level of detail flow feature capture.

Advanced models such as LES and DNS offer a more detailed representation of flow field characteristics, but the computing cost is often prohibitively high. the RANS model is commonly used to capture the macroscopic distributions of three-dimensional thermal-hydraulic parameters with a much reduced cost [127]. The performance of RANS has been demonstrated to be effective in several research studies. Pointer et al.[99] performed simulations of flow in a wire-wrapped 7-pin bundle using both RANS and LES methods. Their findings demonstrated that the RANS-based CFD approach was capable of accurately predicting cross-flow behaviour. Debbarma and Pandey[33] conducted a numerical study on the proposed model HPLWR, focusing on rod spacing and sub-channel behaviour within a rod bundle. Their analysis revealed that the RNG k-ε with enhanced near-wall treatment provided the most accurate predictions for flow and heat transfer characteristics in sub-channels. Simulation results demonstrated that the inclusion of wire-wrapped spacers significantly enhanced flow mixing while maintaining a relatively low-pressure drop across the assembly. Additionally, the simulations indicated that the temperatures stayed within material limits, suggesting that the wire-wrapped spacer enhanced the safety design. Merzari et al. [92] assessed RANS calculations from two independent research institutions in comparison to LES simulations carried out by Argonne National Laboratory, which is widely regarded as the reference data for wire-wrapped rod bundles. Among their various simulations, the k-ω SST turbulence model demonstrated the highest accuracy, making it the preferred choice in this PhD study. The same finding was demonstrated in the work of the other group [145]. Leung et al.[79] investigated how sensitive CFD predictions are to two turbulence models: k-ω and v2f. The study found that the k-ω model consistently under-predicted wall temperature measurements across all three experimental test conditions. In contrast, the v2f model under-predicted results in subcritical conditions but over-predicted them in pseudo-supercritical and supercritical conditions. Additionally, the peak wall temperature in the wire-wrapped cases was simulated to be lower than that observed in non-wired rod bundles. Furthermore,

Podila and Rao's study[98] concludes that the k-ω SST turbulence model provided the most accurate predictions against experimental data in pseudo and supercritical conditions, while the v2f model performed better under subcritical test conditions.

Coarse-grid CFD approaches for wire-wrapped rod bundles have also been explored by Hu and Fanning [53] and Bieder et al. [15], as discussed in the previous section. Their work demonstrated that with appropriate modeling strategies, such as momentum source terms or wall function treatments, key thermal-hydraulic features can be captured while significantly reducing computational cost.

Numerical studies on wire-wrapped rod bundles have highlighted both the strengths and limitations of various turbulence models in predicting thermal-hydraulic behaviour. The presence of wire wraps significantly alters the flow structure by enhancing turbulence and promoting mixing, which leads to lower peak wall temperatures compared to bare rod configurations. While several turbulence models have been applied to this geometry, capturing the detailed flow features often requires fine meshes and results in high computational costs. One of the key research interests is to develop computationally efficient methods that can accurately capture the essential thermal-hydraulic effects of wire-wrapped geometries without requiring excessive computational resources. In this PhD study, a special approach will be considered for SubChCFD to enable this coarse grid CFD method to effectively deal with wire wrap spacers.

2.5 Natural circular loop system

2.5.1 Overview of natural circulation

Natural circulation loops (NCLs) are thermal-hydraulic systems in which fluid motion is driven entirely by buoyancy forces, without the use of mechanical pumps. The circulation arises from density gradients caused by temperature differences within the loop. Typically, an NCL consists of a heat source and a heat sink: fluid in the heated section becomes less dense, while fluid in the cooler section becomes more dense. This density difference establishes a continuous natural flow cycle.

However, temperature-driven flow in NCLs can result in complex behaviour. Variations in density between the vertical sections of the loop can generate fluctuating buoyancy forces that accelerate or decelerate the flow. When combined with frictional losses and thermal dissipation, these fluctuations may lead to flow instabilities, including oscillatory behaviour or even flow reversals [128]. Further modelling challenges

arise from heat conduction through structural materials and transitions between laminar and turbulent flow regimes at different locations in the loop. Accurately capturing these effects is essential for reliable simulation and design of NCL systems.

Beyond their fundamental fluid dynamics, NCLs play a critical role in various engineering applications, particularly where passive heat removal is required. They are widely used in solar thermal systems, electronic cooling, and most notably, in passive safety systems for nuclear reactors. In Generation IV reactor concepts, NCLs are expected to enhance system reliability, reduce operational costs, and improve safety margins by eliminating the need for active pumping [56].

2.5.2 Experimental studies

The study of natural circulation experimental loops attracts significant attention, particularly concerning their stability characteristics under various operating conditions, including those at supercritical pressure. Such systems are known to exhibit unstable behaviour under certain thermal-hydraulic conditions. [21]

Some reduced-scale and simplified integral system test facilities have been established globally to replicate and analyse natural circulation behaviour under controlled conditions. These facilities contribute to the advancement of passive safety system design by supplying experimental datasets that support numerical modelling and predictive simulations of natural circulation loops.

In the early time, Hallinan and Viskanta [47] conducted experimental investigations on natural circulation in a rectangular loop equipped with tube bundles where one vertical section functioned as the heat source and the other as the heat sink. Their results indicated that the transition from laminar to turbulent flow occurred at a relatively low Reynolds number of approximately 340, which was attributed to strong buoyancy effects under mixed convection conditions. Additionally, they found that the friction parameter exhibited an approximately linear relationship with the Reynolds number in the laminar regime, similar to trends observed in forced convection. These findings offer valuable insights into the onset of turbulence and the frictional characteristics of naturally circulating flows, enhancing the overall understanding of stability and performance in passive thermal-hydraulic systems.

Vijayan et al. [122] studied the frictional characteristics and overall hydrodynamics of NCLs using a figure-eight-shaped experimental facility. Their findings revealed that, for a given Reynolds number, the pressure loss coefficient under natural circulation conditions was up to 30% higher than that observed in forced circulation. This increase in pressure loss was accompanied by a notable enhancement in the Nusselt

number, emphasizing the distinct thermal-hydraulic behaviour of NCLs compared to forced-flow systems. These insights enhance the understanding of frictional effects and heat transfer efficiency in naturally circulating systems. Following earlier studies on heat transfer and frictional characteristics, Vijayan et al. [123] shifted their experimental research focus to evaluating the instability behaviour of NCLs in rectangular configurations. Their study analysed three geometrically similar setups, each featuring heating in the lower horizontal arm and cooling in the upper horizontal arm, but differing in tube diameters: 6 mm, 11 mm, and 23.2 mm. The experiments were conducted over a wide range of heater power levels and coolant flow rates. No instabilities were detected in the two smaller diameter loops across the tested conditions; however, the largest loop exhibited oscillatory instabilities and flow reversals under specific experimental conditions. These findings highlight the significant influence of pipe diameter on system stability, suggesting that geometric parameters play a crucial role in determining the dynamic behaviour of NCLs.

2.5.3 Numerical studies

Computational methods, including CFD and system codes (e.g.ATHLET, RELAP, TRACE, and CATHARE), have been widely used to investigate the thermal-hydraulic behaviour, stability characteristics, and transient responses of natural circulation loops. These tools provide a flexible and efficient approach to analysing NCLs under a wide range of conditions, including supercritical pressures and complex geometries, which are challenging to capture through experiments alone. However, accurate numerical prediction remains a challenge due to uncertainties in turbulence modelling, heat transfer correlations, and fluid property variations, particularly in supercritical conditions.

The initial phase of numerical investigations in this area begins with a 1D simulation approach. Vijayan et al. [121] emphasized the importance of frequently switching frictional correlations between laminar and turbulent regimes when modelling unstable oscillatory flow that involves repetitive flow reversals. In their study, the ATHLET code was used to solve 1D mass, momentum, and energy conservation equations, along with a radial heat conduction model to account for wall damping effects. To accurately model the changing flow regime, the laminar friction factor was calculated as $f_l = \frac{16}{|Re|}$, while the turbulent friction factor was determined using the Colebrook–White correlation. This implicit correlation accounts for the combined effects of Reynolds number and relative roughness:

$$\frac{1}{\sqrt{f}} = -2\log_{10}\left(\frac{\varepsilon/D}{3.7} + \frac{2.51}{\mathrm{Re}\sqrt{f}}\right) \tag{2.22}$$

where f is the Darcy friction factor, ε/D is the relative roughness of the pipe, and Re is the Reynolds number.

To ensure a smooth transition and avoid numerical instability, a simple switching criterion was applied:

$$f = \max(f_l, f_t) \tag{2.23}$$

where f_l and f_t are the laminar and turbulent friction factors, respectively. This method avoids abrupt changes in the friction factor near the transitional Reynolds number and helps maintain numerical stability during rapid oscillations. Their simulations showed reasonable agreement with steady-state experimental results [123], although the predicted flow rates were slightly overestimated. The study also highlighted the importance of spatial resolution: fine nodalization was essential to accurately capture instability growth, while coarse grids failed to reproduce the oscillatory behaviour.

Mangal et al. [88] evaluated the performance of RELAP5 in modelling high-pressure natural circulation loops and multi-channel heating systems. Their findings highlighted that the choices made in nodalization and numerical discretization have a significant impact on stability predictions. These are user effects, and they can be minimised by using a standard input template, verifying mesh and time-step independence, changing one setting at a time, and staying within model validity. One limitation noted was the numerical diffusion caused by the first-order upwind scheme, which resulted in artificially stable flow predictions, even in cases where oscillatory behaviour was expected. Additionally, inconsistencies were attributed to semi-empirical equations, which may have led to deviations from experimental results. The stability prediction for single-phase NCLs is highly sensitive to numerical factors and nodalization strategies, as previously discussed.

Ambrosini and Ferreri [4] examined how grid resolution and discretisation methods affect the stability for turbulent flow in a loop with a point heat source and sink. Their findings emphasised that both grid size and the chosen numerical approach significantly impact stability predictions. Among first-order methods, the explicit upwind scheme demonstrated greater effectiveness than its implicit counterpart, maintaining numerical stability. In their later research, the choice of friction correlations was discovered to significantly affect the neutral stability curve. Ambrosini et al. [5]

strongly recommended using accurately assessed wall friction factors, emphasising the importance of properly capturing the transition between laminar and turbulent flow regimes. Their findings demonstrated that improper modelling of friction can lead to inaccuracies in stability predictions, highlighting the necessity of a precise correlation accounting for frictional effects in numerical simulations of NCLs.

Experimental studies have shown that flow stratification and secondary flows occur in NCLs. These phenomena cannot be accurately captured by 1D analyses. This limitation has been identified as a key reason why 1D codes sometimes fail to predict flow stability, leading to inconsistent results across various loop configurations, as noted by Ambrosini[3]. To address these challenges, researchers have increasingly turned to multi-dimensional models and CFD codes. These advanced tools provide greater accuracy in capturing complex flow structures and stability characteristics within NCLs. One of the earliest attempts to develop a 2D model for a toroidal natural circulation loop was conducted by Mertol et al. [90] in 1982. Their study utilized a finite-difference method to account for variations in flow both radially and axially. They expressed friction and heat transfer relationships as a function of the Graetz number ($\mathrm{Gz} = \mathrm{Re}\,\mathrm{Pr}\,\frac{D_h}{x}$). The results showed that average velocity initially increased with Gz, reached a peak, and then declined due to increased friction and reduced temperature differentials at higher velocities. While their model successfully predicted steady-state flow characteristics, it struggled to accurately capture flow reversals, highlighting the limitations of early 2D approaches in modelling complex behaviours of natural circulation loops. Recent research by Desrayaud et al. [36] investigated the effects of Rayleigh number (Ra) and aspect ratio on the behaviour of a rectangular NCL. The simulations utilized staggered, non-uniform 2D Cartesian grids to improve numerical accuracy. The study found that local vortices were the main factor driving the growth of oscillations, emphasizing the critical role of secondary flow structures in influencing loop stability and flow dynamics. These findings provide valuable insights into the mechanisms causing flow instabilities in NCLs, highlighting the importance of considering localized flow features in numerical modelling. Subsequently, in Wilson et al.'s research [135], they conducted transient CFD simulations on simplified 2D NCLs with varying aspect ratios and a range of Rayleigh numbers. By employing an URANS approach, the simulations effectively captured unstable flow behaviour, including persistent flow reversals, which were qualitatively consistent with experimental observations. Furthermore, the steady-state predictions closely matched existing empirical correlations. The study highlighted a significant

sensitivity of flow stability to thermal boundary conditions and loop geometry, showing that higher Rayleigh numbers and larger aspect ratios tend to promote instability in NCLs.

With the increasing availability of computational resources, 3D simulations allow for a more accurate evaluation of turbulent structures, instability mechanisms, and localized heat transfer effects that are not well captured in lower-dimensional models. Various three-dimensional numerical studies have been conducted to gain a better understanding of flow reversals and transition phenomena in NCLs. In early research, Lavine et al. [77][76] developed a 3D steady-state model for a toroidal NCL. Their model effectively represented streamwise flow reversal, secondary flow, and asymmetric temperature distribution. The findings indicated that 1D and 2D models tend to overestimate total buoyancy as they cannot represent 3D recirculations and cross-flows, resulting in average axial velocity predictions that were 31% and 47% higher than actual measurements, respectively. Recent observations have shown flow reversal in the toroidal NCL, attributed to the formation of small-scale vortices, localized recirculation zones, and helical flow motion within the bulk circulation. To enhance the understanding of these complex flow dynamics, Ridouane et al. [52] developed a more advanced 3D numerical model, focusing on a Rayleigh number range of 10^3–10^7. This refined approach improved the visualization and analysis of vortex structures and instability mechanisms, providing deeper insights into flow reversals and their effects on NCL behaviour.

After this, Kudariyawar et al. [74] conducted 3D steady-state and transient CFD simulations of the Bhabha Atomic Research Centre (BARC) NCL in a vertical heater–vertical cooler (VHVC) configuration. Their study demonstrated strong agreement with both experimental data and established correlations, highlighting the accuracy and reliability of their CFD approach. The numerical methodology involved solving the RANS equations using both the standard k-ε turbulence model with wall functions and the low-Reynolds-number k-ε model developed by Launder and Sharma. The low-Re model proved particularly effective in capturing the complex flow structures and oscillatory instabilities characteristic of natural circulation loops, especially under low-Reynolds-number conditions.

Wilson et al. [133] conducted a comparison between URANS models and LES for simulating rectangular NCLs. Their study revealed that the Elliptic-Blending Reynolds Stress Model (EB-RSM) exhibited the best agreement with LES results. The Launder-Sharma (LS) k-ε model also performed well, accurately capturing key

flow structures. In contrast, the k-ω SST model tended to overpredict turbulence levels, leading to excessive mixing and enhanced heat transfer, especially in the cooler section, which resulted in a greater temperature drop and overall lower predicted fluid temperatures compared to both experimental data and higher-fidelity models like LES. Additional simulations using the LS k-ε model showed a strong alignment with experimental data and effectively captured flow trends. However, the study emphasized that consistent results with empirical correlations do not necessarily guarantee the accuracy of the flow field. These findings highlight the effectiveness of URANS models for simulating NCLs, providing valuable insights for the design and validation of such systems.

Numerical modelling has greatly enhanced our understanding of NCLs by capturing essential thermal-hydraulic behaviours, flow instabilities, and stability characteristics. While 1D and 2D models provided initial insights, 3D simulations and advanced turbulence models led to improved accuracy in predicting flow reversals and secondary flows.

Chapter 3

Methodology

3.1 CFD

As introduced in the literature review, CFD is a powerful approach for analysing complex flow and heat transfer behaviours in nuclear systems, including those operated under supercritical conditions.

This section outlines the fundamental methodology underpinning CFD analysis relevant to the present study. It begins with the governing equations, followed by the closure problem involving turbulence modelling and wall treatment. The finite volume method (FVM) used for numerical discretisation is also briefly introduced. The fidelity of CFD predictions depends on various factors such as numerical schemes, grid resolution, and physical modelling, all of which are discussed in this section.

3.1.1 Governing equations

The behaviour of fluid flow and heat transfer is governed by the fundamental conservation laws of mass, momentum, and energy. The resulting governing equations form the basis of CFD analysis.

The continuity equation ensures mass conservation in a fluid flow and is expressed as:

$$\frac{\partial \rho}{\partial t} + \nabla \cdot (\rho \mathbf{u}) = 0 \tag{3.1}$$

where ρ is the fluid density, t is time, and $\mathbf{u}$ is the velocity vector.

The Navier-Stokes equations describe the conservation of momentum for a Newtonian fluid. They are derived from Newton's second law of motion, which states that the rate of change of momentum of a fluid element is equal to the sum of the forces acting on it, including pressure gradients, viscous stresses, and external body forces

such as gravity. These equations provide a mathematical framework for analysing fluid motion by accounting for inertia, pressure forces, viscous effects, and external body forces.

The general form of the Navier-Stokes equations in conservation form is given as:

$$\rho\frac{\partial \mathbf{u}}{\partial t} + \rho\nabla\cdot(\mathbf{u}\otimes\mathbf{u}) = -\nabla p + \nabla\cdot\boldsymbol{\tau} + \rho\mathbf{f} \tag{3.2}$$

where $\mathbf{u} = (u, v, w)$ is the velocity vector, p is the pressure, $\boldsymbol{\tau}$ is the viscous stress tensor, and $\mathbf{f}$ represents external body forces such as gravity.

The viscous stress tensor $\boldsymbol{\tau}$ is defined as:

$$\boldsymbol{\tau} = \mu\left(\nabla\mathbf{u} + \nabla\mathbf{u}^T\right) - \frac{2}{3}\mu(\nabla\cdot\mathbf{u})\mathbf{I} \tag{3.3}$$

Here, μ is the dynamic viscosity, and $\mathbf{I}$ is the identity tensor. The second term accounts for the effect of volumetric expansion or compression.

The transient term $\rho\frac{\partial \mathbf{u}}{\partial t}$ represents unsteady effects, the convective term $\rho\nabla\cdot(\mathbf{u}\otimes\mathbf{u})$ represents advection, the pressure gradient term $-\nabla p$ accounts for pressure forces, the viscous diffusion term $\nabla\cdot\boldsymbol{\tau}$ models viscous effects, and the body force term $\rho\mathbf{f}$ includes external forces such as gravity. Together, these terms fully define fluid motion under the continuum assumption.

The conservation of energy in the CFD solver is expressed as:

$$\frac{\partial(\rho c_p T)}{\partial t} + \nabla\cdot(\rho c_p \mathbf{u} T) = \nabla\cdot(k\nabla T) + \dot{q} \tag{3.4}$$

where T is the temperature, c_p is the specific heat at constant pressure, k is the thermal conductivity, and $\dot{q}$ represents the volumetric heat generation.

3.1.2 Closure problem and turbulence modelling

The Navier–Stokes equations can describe the full behaviour of fluid flow, including turbulence. However, turbulent flows exhibit complex, chaotic fluctuations across a wide range of spatial and temporal scales. To capture all these details directly in a simulation, extremely fine grids and small time steps are required, which makes the computational cost prohibitively high for practical engineering problems.

DNS solves the Navier–Stokes equations without any turbulence modelling. It resolves all scales of motion and provides very accurate results. However, DNS is limited to simple geometries and low Reynolds number flows because of its high computational demand. For this reason, it is mostly used in academic research or to validate turbulence models as a numerical experiment.

To reduce the computational cost, other approaches have been developed. LES resolves the large-scale turbulent structures while modelling the smaller, subgrid-scale motions. LES is based on the spatially filtered Navier-Stokes equations, where the filtering operation introduces the subgrid-scale (SGS) stress tensor:

$$\tau_{ij}^{SGS} = \overline{u_i u_j} - \bar{u}_i \bar{u}_j \tag{3.5}$$

which represents the effect of unresolved scales on the resolved flow. To close the equations, this SGS tensor must be approximated using a subgrid-scale model. Various SGS models have been developed for this purpose, and the choice depends on the flow configuration and desired accuracy.

LES can capture important unsteady and three-dimensional features of turbulence with better accuracy than simpler models, but it still requires relatively fine meshes near walls and remains expensive for complex flows.

RANS is widely used in engineering applications, which is much less computationally expensive than DNS and LES. RANS solves time averaged Navier-Stokes equations based one the following decomposition of the flow variables:

$$\mathbf{u} = \overline{\mathbf{u}} + \mathbf{u}', \quad p = \bar{p} + p'$$

where $\bar{\mathbf{u}}$ and $\bar{p}$ represent the mean velocity and pressure, while $\mathbf{u}'$ and p' denote the fluctuating components.

When this decomposition is substituted into the Navier–Stokes equations and averaged over time, new terms appear which are the so-called Reynolds stress tensor:

$$\tau_{ij} = -\rho \overline{u_i' u_j'}$$

These additional terms represent the influence of turbulence on the mean flow. These new terms are additional unknown variables, which cannot be determined from the RANS equations by simply introducing more equations, nor can they be derived exactly from theory. These need to be represented using empirical turbulence models. Hence this problem is known as the closure problem.

Most turbulence models are eddy viscosity type based on Boussinesq hypothesis [119]. That assumes a linear relationship between the Reynolds stresses and the mean velocity gradients. that is:

$$\tau_{ij} = 2\nu_t \bar{S}_{ij} - \frac{2}{3}\rho k \delta_{ij} \tag{3.6}$$

$$S_{ij} = \frac{1}{2}\left(\frac{\partial U_i}{\partial x_j} + \frac{\partial U_j}{\partial x_i}\right) \tag{3.7}$$

Different turbulence models have different ways calculating the eddy viscosity ν_t. The mixing length model due to Prandt is one of the most simple models [130], which express turbulent viscosity is defined as:

$$\nu_t = l_m^2 \left|\frac{dU}{dy}\right| \tag{3.8}$$

where l_m is the mixing length, representing the characteristic size of turbulent eddies. While effective for simple shear flows, such as fully developed pipe flows, this model lacks general applicability for complex geometries and highly unsteady flows. In practice, the mixing length is often estimated based on the distance from the wall or determined using empirical relations based on specific flow conditions.

Two-equation turbulence models introduce transport equations for turbulence quantities, improving their accuracy over algebraic models. The most widely used two-equation models are the k-ϵ and k-ω models. [119]

The k-ϵ model provides a widely used solution to the closure problem by solving two additional transport equations, one for turbulent kinetic energy (k) and one for its dissipation rate (ϵ). In the k-ϵ model, the turbulent viscosity ν_t is modelled as:

$$\nu_t = C_\mu \frac{k^2}{\varepsilon} \tag{3.9}$$

where C_μ is an empirical constant.

To determine k and ϵ, the model solves two additional transport equations:

$$\frac{\partial k}{\partial t} + \mathbf{u} \cdot \nabla k = \nabla \cdot \left(\frac{\nu_t}{\sigma_k} \nabla k\right) + P_k - \epsilon \tag{3.10}$$

$$\frac{\partial \epsilon}{\partial t} + \mathbf{u} \cdot \nabla \epsilon = \nabla \cdot \left(\frac{\nu_t}{\sigma_\epsilon} \nabla \epsilon\right) + C_1 \frac{\epsilon}{k} P_k - C_2 \frac{\epsilon^2}{k} \tag{3.11}$$

where P_k is the production of turbulent kinetic energy, and C_1, C_2, σ_k, and σ_ϵ are model constants.

The k-ϵ model is robust and computationally efficient, making it popular for many engineering applications. However, it relies on wall functions for near-wall treatment and may not perform well in flows with strong pressure gradients or separation.

The Launder-Sharma model is a modification of the standard k-ϵ turbulence model, formulated to resolve low-Reynolds-number effects near walls without the need for empirical wall functions. In this study, the Launder-Sharma model is employed in

NCL resolved CFD simulations. It introduces damping functions that reduce turbulent kinetic energy production and dissipation in the viscous sublayer, allowing the model to be integrated all the way to the wall.

The transport equations for k and ϵ are expressed as:

$$\frac{\partial k}{\partial t} + \mathbf{u} \cdot \nabla k = \nabla \cdot \left(\frac{\nu_t}{\sigma_k} \nabla k \right) + P_k - \epsilon \tag{3.12}$$

$$\frac{\partial \epsilon}{\partial t} + \mathbf{u} \cdot \nabla \epsilon = \nabla \cdot \left(\frac{\nu_t}{\sigma_\epsilon} \nabla \epsilon \right) + C_1 f_1 \frac{\epsilon}{k} P_k - C_2 f_2 \frac{\epsilon^2}{k} \tag{3.13}$$

where f_1 and f_2 are damping functions introduced to model near-wall viscous effects. These functions are typically expressed in terms of the turbulent Reynolds number:

$$Re_t = \frac{k^2}{\nu \epsilon} \tag{3.14}$$

where ν is the kinematic viscosity.

The damping functions are defined as:

$$f_1 = \frac{Re_t}{Re_t + 5} \tag{3.15}$$

$$f_2 = \frac{1}{1 + 0.02 Re_t} \tag{3.16}$$

These functions reduce the turbulent viscosity and dissipation near the wall where Re_t is low, enabling accurate resolution of the laminar-to-turbulent transition and the viscous sublayer.

The k-ω turbulence model also solves a two-equation system, but instead of using the dissipation rate ϵ, it introduces the specific dissipation rate $\omega = \epsilon / k$ as the second transported variable.

The transport equations for k and ω are given by:

$$\frac{\partial k}{\partial t} + \mathbf{u} \cdot \nabla k = \nabla \cdot \left(\frac{\nu_t}{\sigma_k} \nabla k \right) + P_k - \beta^* k \omega \tag{3.17}$$

$$\frac{\partial \omega}{\partial t} + \mathbf{u} \cdot \nabla \omega = \nabla \cdot \left(\frac{\nu_t}{\sigma_\omega} \nabla \omega \right) + \alpha \frac{\omega}{k} P_k - \beta \omega^2 \tag{3.18}$$

where $\nu_t = k / \omega$, and α, β, β^*, σ_k, and σ_ω are empirical constants.

However, the k-ω model can be overly sensitive to turbulence properties specified in the freestream. To overcome the freestream sensitivity of the k-ω model and

improve performance in separated flows, the k-ω SST (Shear Stress Transport) model was developed. The SST model blends the k-ω formulation near walls with the k-ϵ formulation in the far field, using a blending function to transition smoothly between the two models.

Another key feature of the SST model is its modified definition of turbulent viscosity, which includes a limiter on shear stress transport to better capture flow separation:

$$\nu_t = \frac{a_1 k}{\max(a_1\omega, SF_2)} \tag{3.19}$$

Here, a_1 is a model constant (typically 0.31), S is the magnitude of the mean strain rate defined as $S = \sqrt{2S_{ij}S_{ij}}$, and F_2 is defined as:

$$F_2 = \tanh\left(\left[\max\left(\frac{2\sqrt{k}}{\beta^*\omega y}, \frac{500\nu}{y^2\omega}\right)\right]^2\right) \tag{3.20}$$

where y is the distance to the nearest wall, ν is the kinematic viscosity, and β^* is a model constant.

This function returns values close to 1 near the wall, activating the viscosity limiter, and approaches 0 in the freestream, where the limiter is turned off. It ensures that the eddy viscosity is reduced in regions of high shear, preventing overprediction of turbulence and improving accuracy in separated flow regions.

By combining the strengths of both the k-ϵ and k-ω models, the SST model offers robust and accurate predictions across a wide range of turbulent flow scenarios. Owing to its enhanced near-wall performance and reliability in separated and shear-dominated flows, the SST model is selected in this PhD study for simulating mixed convection under supercritical conditions, as well as flow in wire-wrapped spacer geometries. For the coarse-grid CFD (SubChCFD), a simple mixing length turbulence model is employed. Given the coarse mesh resolution, there is no significant advantage in using more sophisticated turbulence models.

3.1.3 Wall treatment in turbulence modelling

Accurate near-wall treatment is important in CFD simulations to account for the near-wall effects such as heat transfer and shear stress. The thermal boundary layer is the near-wall region where the fluid temperature adjusts from the bulk value to the wall condition. In internal flows it grows downstream from the inlet. The appropriate wall treatment depends on the turbulence model employed and the grid resolution used

near solid boundaries. The structure of the turbulent boundary layer is illustrated in Figure 3.1.

Near the wall, the flow field differs significantly from the freestream due to the presence of the boundary layer, where viscous effects become important. The boundary layer is typically divided into two main regions: the inner layer and the outer layer. The inner layer is directly influenced by the wall and can be further subdivided into the viscous sublayer, buffer layer, and the log-law region. In the viscous sublayer, viscous shear forces dominate and the velocity increases approximately linearly with distance from the wall. The buffer layer provides a transitional zone between viscous and turbulent effects. Further from the wall, in the log-law region, turbulent mixing becomes dominant, and the velocity follows a logarithmic distribution. Above the inner layer lies the outer layer, where the flow begins to approach freestream conditions and is less affected by the wall, though still influenced by large-scale turbulent structures.

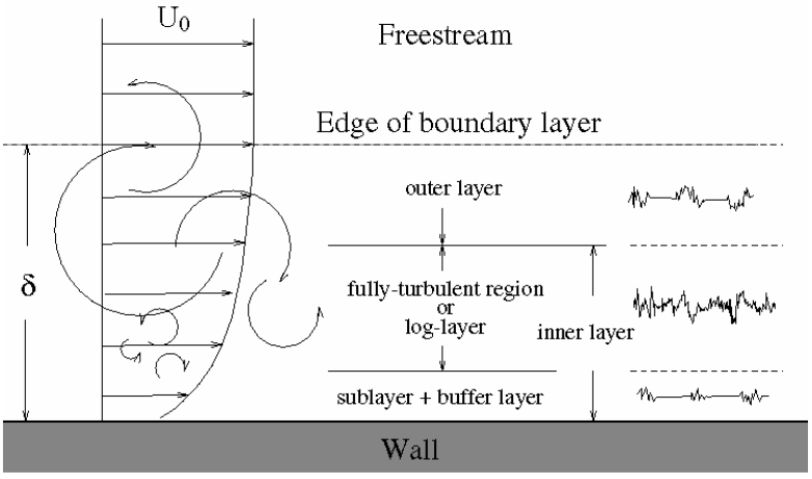

Figure 3.1: Structure of the turbulent boundary layer, showing sublayer, buffer layer, and log-law region [7].

Two main strategies exist for handling the near-wall region in turbulence modelling: wall functions and wall-resolved models. Wall functions rely on empirical relations to represent the logarithmic law to bridge the near-wall and outer regions, avoiding the need for an extremely fine mesh near the wall. They are valid when the first grid point lies in the log-law region, typically for $y^+ > 30$. In contrast, wall-resolved or low-Reynolds-number models resolve the entire near-wall structure, including the viscous sublayer, by refining the mesh to ensure $y^+ < 1$. This provides greater accuracy but at a higher computational cost.

Figure 3.2 illustrates the velocity distribution across the near-wall region, classified by y^+.

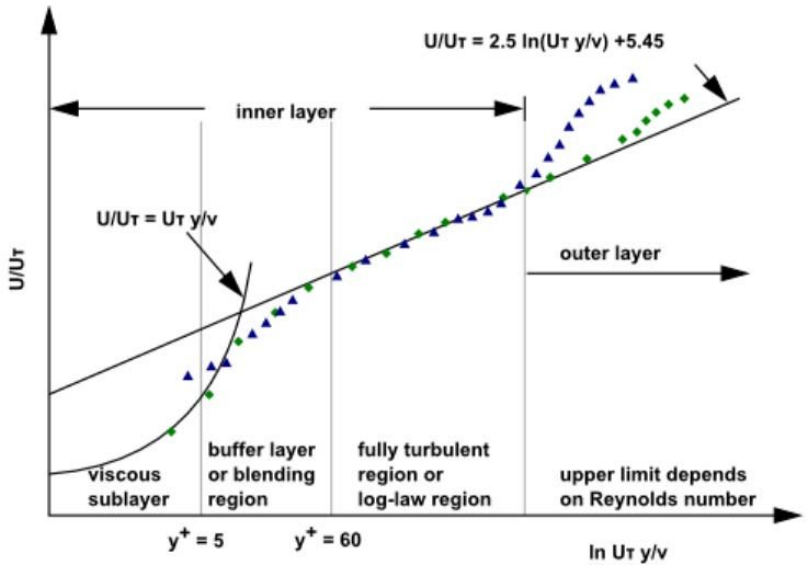

Figure 3.2: Velocity distribution in the near-wall region, highlighting different flow layers and y^+ values. [72]

In the viscous sublayer ($y^+ < 5$), the velocity profile is approximately linear:

$$U^+ = y^+ \tag{3.21}$$

where $U^+ = U/u_\tau$ is the dimensionless velocity, $y^+ = yu_\tau/\nu$ is the dimensionless wall distance, and $u_\tau = \sqrt{\tau_w/\rho}$ is the friction velocity.

In the log-law region ($y^+ > 30$), the velocity follows the classical logarithmic distribution:

$$U^+ = \frac{1}{\kappa}\ln(y^+) + B \tag{3.22}$$

where $\kappa \approx 0.41$ is the von Kármán constant, and $B \approx 5.0$ is an empirical constant [100, 130].

The buffer layer ($5 < y^+ < 30$) acts as a transition region between these two behaviours.

These velocity profiles are empirical representations of the near-wall behaviour in turbulent boundary layers and are widely used in CFD for two main purposes. First, they provide guidance for near-wall mesh generation. In wall-resolved simulations, such as those using low-Reynolds-number turbulence models, the mesh is refined to ensure $y^+ < 1$ so that the viscous sublayer is fully resolved. In contrast, when wall functions are used, the first grid point is typically placed in the log-law region

($y^+ > 30$). Second, these profiles form the basis of wall function formulations in RANS turbulence models. In such cases, they are used to approximate wall shear stress and near-wall velocity or temperature gradients without explicitly resolving the sublayer. Thus, the U^+–y^+ relations play a central role in both mesh design and turbulence model implementation.

The effectiveness of each approach depends on mesh resolution, turbulence model selection, and the flow regime. Figure 3.3 compares the use of wall functions and wall-resolved approaches.

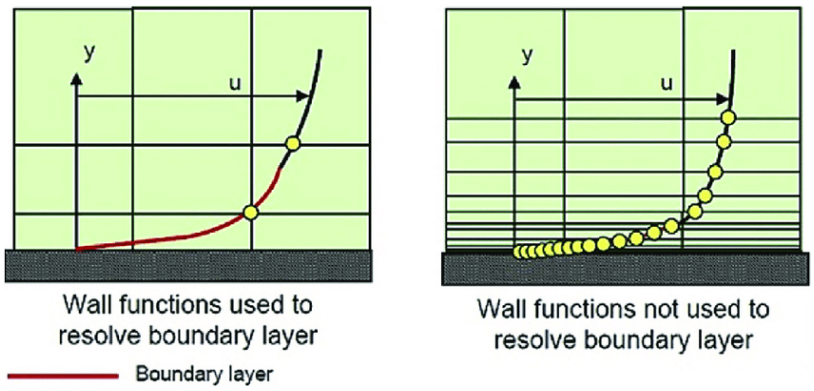

Figure 3.3: Comparison of wall function approach and resolving the boundary layer using a fine mesh.

Wall functions offer computational efficiency and are commonly used in turbulent flow simulations when the near-wall mesh is relatively coarse, particularly when the first grid point lies within the log-law region (typically $y^+ > 30$). However, they may introduce errors in regions with flow separation, strong pressure gradients, or significant heat transfer. Wall-resolved models, such as the low-Reynolds-number Launder–Sharma and the SST model with sufficient near-wall resolution, are more accurate but computationally demanding.

In this PhD study, wall-resolved turbulence models are employed in the resolved CFD simulations to capture near-wall behaviour accurately. In contrast, the SubChCFD methodology adopts a different approach by modelling near-wall effects using empirical correlations for friction factor and heat transfer. The implementation of these models is detailed in the SubChCFD methodology section.

3.1.4 Finite Volume Method

FVM is a widely used numerical technique for solving the partial differential equations (PDEs) governing fluid flow and heat transfer. It is particularly popular in

CFD due to its local conservation properties and ability to handle complex geometries and boundary conditions. Unlike the finite difference method, which discretises derivatives at grid points, or the finite element method, which relies on interpolation through shape functions, the FVM integrates the governing equations over finite control volumes, ensuring strict conservation of mass, momentum, and energy within each volume.

The computational domain is subdivided into discrete control volumes, with each control volume enclosing a computational node. The governing equations are then integrated over each control volume, transforming the differential form into a set of algebraic equations. Figure 3.4 shows a structured Cartesian grid where P denotes the control volume center and W, E, N, S represent neighboring nodes.

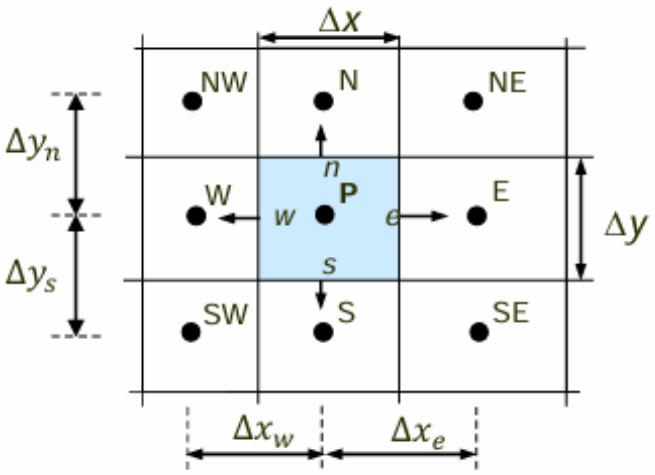

Figure 3.4: Structured grid representation in the Finite Volume Method (FVM).

The integral form of a general conservation equation for a scalar variable ϕ is written as:

$$\frac{\partial}{\partial t}\int_V \rho\phi\, dV + \oint_A \rho\phi\, \mathbf{u}\cdot d\mathbf{A} = \oint_A \Gamma\nabla\phi\cdot d\mathbf{A} + \int_V S_\phi\, dV \tag{3.23}$$

where the terms represent transient accumulation, convective transport, diffusive flux, and source contributions, respectively.

In Eq. 3.21, the original volume integrals for the convection and diffusion terms have been converted to surface integrals using Gauss's divergence theorem. The discretised form of equation 3.21 requires the fluxes at control volume faces to be approximated using interpolation or reconstruction schemes. The choice of spatial discretisation scheme—such as upwind differencing for stability or central differencing

and QUICK for higher accuracy—directly influences numerical diffusion and solution accuracy.

In this PhD study, to ensure numerical stability during the initial stages of the simulation, a first-order upwind scheme is used. Once the solution begins to converge and the flow field stabilises, the simulation is restarted using a second-order upwind scheme to improve accuracy while maintaining the robustness of convergence.

Time-dependent problems require temporal discretisation using either explicit or implicit schemes, with the choice depending on stability requirements and computational efficiency. In contrast, steady-state simulations assume that time-dependent terms are zero, and the solution proceeds iteratively until a converged stationary state is reached.

Depending on the nature of the problem, either steady-state or transient (unsteady) solvers may be employed. Steady-state simulations assume that all time derivatives are neglected, allowing the solution to converge to a final state without resolving temporal evolution. This approach is computationally efficient and suitable for flows where transient behaviour is negligible. In contrast, unsteady solvers retain the time derivative terms and resolve the flow field as it evolves over time. This is essential for capturing time-dependent phenomena such as buoyancy-induced oscillations or flow instabilities. In this study, both steady and unsteady simulations are used depending on the flow regime and objectives of each case.

Because the Navier–Stokes equations do not have an explicit equation for pressure, a pressure-velocity coupling strategy is essential. SIMPLE (Semi-Implicit Method for Pressure-Linked Equations) solves momentum with a guessed pressure, then applies iterative pressure corrections within each time step; it is robust but can damp transients if under-iterated. PISO (Pressure-Implicit with Splitting of Operators) uses one or more non-iterative pressure corrections per step; it typically gives better time accuracy with fewer inner iterations. Projection (fractional-step) methods advance an intermediate velocity and then solve one Poisson equation to project onto a divergence-free field; they are simple and accurate for unsteady flows but need consistent pressure boundary conditions to avoid splitting errors.

Overall, the Finite Volume Method, together with appropriate discretisation schemes and pressure-velocity coupling algorithms, forms the numerical foundation of most CFD solver.

3.1.5 Numerical platform: Code_Saturne

All CFD simulations in this study are performed using Code_Saturne, an open-source, general-purpose CFD solver developed by EDF [8]. Code_Saturne is based on the finite volume method and supports unstructured meshes, making it suitable for complex geometries encountered in nuclear thermal-hydraulic applications. The solver handles incompressible or weakly compressible flows and provides robust treatment for turbulence, heat transfer, and source terms.

In this work, Code_Saturne is used to solve the RANS equations along with turbulence models such as k–ω SST and Launder–Sharma, depending on the case. For near-wall modelling, both wall-resolved and wall-function approaches are supported and selected according to the mesh resolution. Boundary conditions and initial fields are defined using the graphical user interface (GUI), which also allows configuration of solver parameters and numerical schemes. Gravity is included as a body force in the momentum equations to represent the indirect effect of buoyancy. In combination with temperature-dependent fluid properties, this enables the direct effect of buoyancy to be captured through density variations in the flow field. This is especially important in supercritical conditions, where fluid properties vary strongly with temperature. Thermal physical properties can be assigned in two ways: the first is defined directly through the GUI, and the second, for supercritical conditions, involves implementing a user-defined Fortran subroutine to read from a pre-tabulated property table.

The same solver framework also serves as the foundation for SubChCFD, where a user-defined subroutine is implemented within Code_Saturne to extract subchannel-level quantities from the computing mesh and apply empirical closure models for wall friction and heat transfer.

3.2 SubChCFD

3.2.1 Overview

The fundamental concepts of SubChCFD have been introduced briefly in the literature review, and in this section, a detailed description of the numerical framework and mesh strategy is provided.

As introduced in the literature review, SubChCFD is a novel coarse-mesh CFD approach that integrates the advantages of both subchannel analysis and conventional CFD methods. The computational framework consists of two levels: the computing

mesh and the subchannel filtering mesh. The computational mesh is used to solve the governing equations with a relatively coarse resolution compared to high-fidelity CFD, enabling efficient numerical integration using the underlying CFD solver. The resulting flow fields are then spatially averaged over each of the subchannels to extract bulk flow parameters such as velocity and temperature. Figure 3.5 illustrates this structure for a 2×2 rod bundle. The grid represents the coarse computing mesh, while each colored region represents one sub-channel. There are three different subchannel types: red for the central subchannel, beige for edge subchannels, and blue for corner subchannels. Within each subchannel, the averaged flow quantities are used to evaluate wall friction and heat transfer through empirical correlations. These subchannel quantities are then used in the solution for the computing mesh as wall treatments, replacing the standard wall functions.

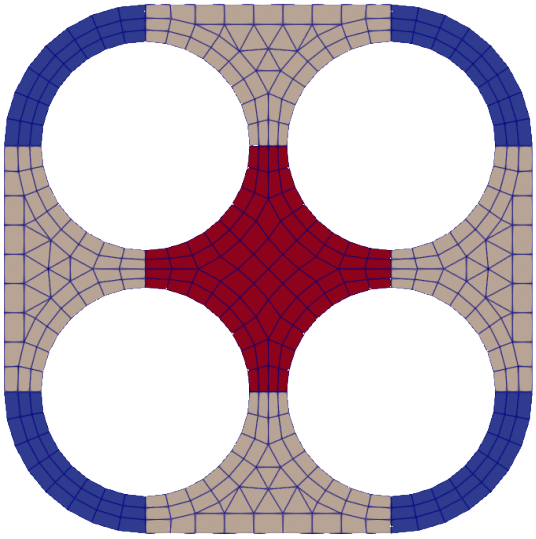

Figure 3.5: Illustration of the subchannel meshing strategy for a 2×2 rod bundle case.

The workflow of SubChCFD is illustrated in Figure 3.6.

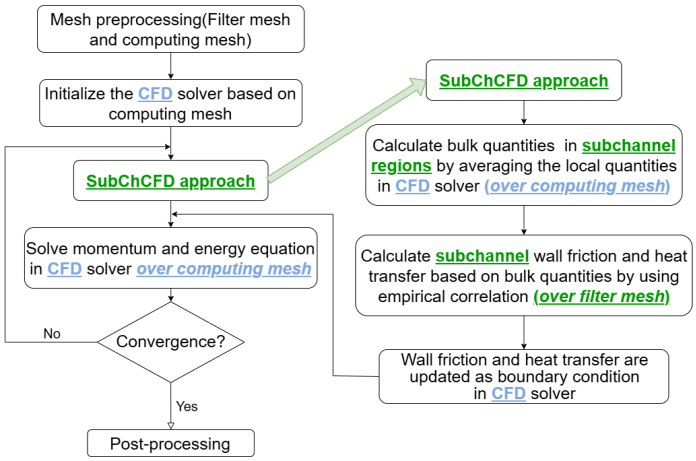

Figure 3.6: Workflow of the SubChCFD methodology.

A key distinction between SubChCFD and conventional CFD lies in the approach to near-wall modelling. Instead of relying on traditional wall functions embedded in RANS turbulence models, SubChCFD computes wall friction and heat transfer using empirical subchannel correlations. These quantities are then applied as boundary conditions in the CFD solver over the computational mesh.

3.2.2 Numerical implementation

In SubChCFD, the RANS momentum equation is discretised using the FVM over each control volume of the computing mesh, resulting in the following expression:

$$\iiint_{\Omega} \frac{\partial(\rho \mathbf{u})}{\partial t}\, dV + \iint_{S} \mathbf{u}\,(\rho\, \mathbf{u}\cdot\mathbf{n})\, dA = -\iint_{S} \bar{p}\,\mathbf{n}\, dA + \iint_{S} \bar{\boldsymbol{\sigma}}\cdot\mathbf{n}\, dA + \iiint_{\Omega} \mathbf{S}_u\, dV \quad (3.24)$$

where Ω is the control volume, S its surface, $\bar{\sigma}$ the viscous stress tensor, and $\vec{S}_u$ external momentum sources such as gravity or flow resistance.

A key feature of the SubChCFD formulation is the treatment of the viscous stresses differently for the interior and wall surfaces. This concept is illustrated in Figure 3.7.

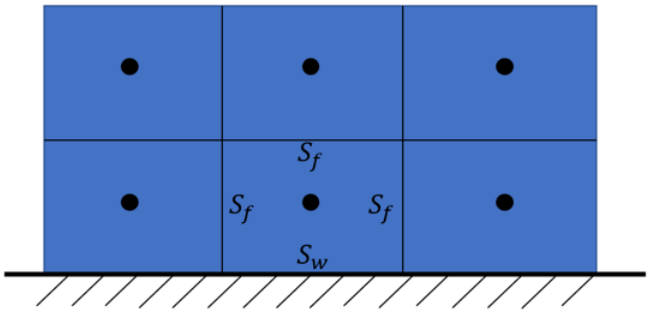

Figure 3.7: Decomposition of shear stress in SubChCFD: wall shear stress and internal face shear stress.

The total shear stress contribution across the control volume surface is therefore rewritten as:

$$\iint_S \bar{\sigma}\cdot n\, dA = \iint_{S_w} \bar{\sigma}\cdot n\, dA + \iint_{S_f} \bar{\sigma}\cdot n\, dA \tag{3.25}$$

where S_w represents the wall surface, and S_f denotes internal faces between neighboring cells. The internal face shear stresses are modelled in a standard way as in any CFD solver and can be expressed as:

$$\iint_{S_f} \bar{\sigma}\cdot n\, dA = \iint_{S_f} (\mu + \mu_t)\left(\nabla u + (\nabla u)^{\mathsf{T}} - (\nabla\cdot u)\,\delta\right)\cdot n\, dA \tag{3.26}$$

where $\vec{u}$ is the velocity vector, and δ is the identity tensor. μ_t is the eddy viscosity, and when a mixing length model is used, it is expressed as:

$$\mu_t = \rho l_m^2 \sqrt{2 S_{ij} S_{ij}} \tag{3.27}$$

With l_m being the local mixing length and S_{ij} the strain rate tensor. In bundle-type flows, the mixing length is approximated using a characteristic length scale given by [83]:

$$l_m = 0.09\,\Delta \tag{3.28}$$

where Δ represents the effective boundary layer thickness and is taken as half the hydraulic diameter in this study.

In contrast, the wall shear stress is modelled using the Darcy–Weisbach Equation based on the subchannel bulk flow quantities [22]:

$$\iint_{S_w} \bar{\sigma}\cdot n\, dA = -\frac{1}{4} f \cdot \frac{1}{2} \rho_b\, \bar{u}_b\, |\bar{u}_b| \iint_{S_w} dA \tag{3.29}$$

where f is friction factor, and ρ_b, $\bar{u}_b$ are the bulk density and bulk velocity of the subchannel, respectively.

For PWR fuel channels, the friction factor is evaluated using an empirical correlation in the baseline SubChCFD implementation [83]:

$$f = \left[a + b_1 \left(\frac{P}{D} - 1 \right) + b_2 \left(\frac{P}{D} - 1 \right)^2 \right] / Re^n \tag{3.30}$$

where the coefficients a, b_1, b_2, n depend on the subchannel type and are given in Table 3.1.

Table 3.1: Cheng and Todreas subchannel friction factor correlation constants.

Subchannel type	**a**	**b1**	**b2**	**n**
Interior (laminar)	35.55	263.7	-190.2	1
Edge (laminar)	44.40	256.7	-267.6	1
Corner (laminar)	58.83	160.7	-203.5	1
Interior (turbulent)	0.1339	0.09059	-0.009926	0.18
Edge (turbulent)	0.143	0.04199	-0.04428	0.18
Corner (turbulent)	0.1452	0.02681	-0.03411	0.18

The treatment of the energy equation in SubChCFD follows a similar approach, with the heat flux term divided into two components.

$$C_p \left(\iiint_\Omega \frac{\partial(\rho T)}{\partial t} \, dV + \iint_S (\rho T)\,(u \cdot n)\, dA \right) = - \iint_S q \cdot n \, dA + \iiint_\Omega S_E \, dV \tag{3.31}$$

$$- \iint_S q \cdot n \, dA = - \iint_{S_w} q \cdot n \, dA - \iint_{S_f} q \cdot n \, dA \tag{3.32}$$

The normal diffusion term across interior faces is computed as:

$$\iint_{S_f} q \cdot n \, dA = - \iint_{S_f} (\lambda + \lambda_t) \, \nabla T \cdot n \, dA \tag{3.33}$$

where λ and λ_t represent the molecular and turbulent thermal conductivities, respectively.

For wall faces, when the Neumann boundary condition is applied (prescribed heat flux), the heat flux equation simplifies to:

$$\iint_{S_f} q \cdot n \, dA = q \iint_{S_w} dA \tag{3.34}$$

In this case, the Nusselt number correlation is not required during the main simulation loop but is instead used during post-processing to estimate the wall temperature:

$$T_w = T_b - \frac{qD_h}{\lambda Nu} \tag{3.35}$$

The Nusselt number is evaluated using the empirical correlation: -

$$Nu = \psi (Nu_\infty)_{c.t.} \tag{3.36}$$

where

$$\psi = 1 + 0.9120 \, \mathrm{Re}^{-0.1} \, \mathrm{Pr}^{0.4} \left(1 - 2.0043 e^{-B}\right) \tag{3.37}$$

$$B = \frac{D_h}{D} \tag{3.38}$$

The fully developed flow Nusselt number is computed using the Dittus-Boelter equation:

$$(Nu_\infty)_{c.t.} = \begin{cases} 0.023 \, \mathrm{Re}^{0.8} \, \mathrm{Pr}^{0.4}, & \text{fluid heating} \\ 0.023 \, \mathrm{Re}^{0.8} \, \mathrm{Pr}^{0.3}, & \text{fluid cooling} \end{cases} \tag{3.39}$$

3.2.3 Mesh sensitivity

To assess mesh sensitivity, Liu et al. [83] defined several 'standard' mesh strategies, as shown in Figure 3.8. These strategies differ in terms of the number of layers and elements in both the wall and core regions.

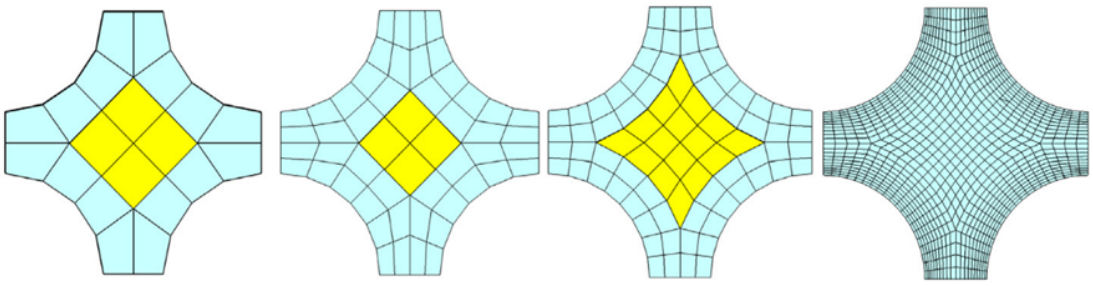

(a) Mesh-1 (b) Mesh-2 (c) Mesh-3 (d) CFD mesh

Figure 3.8: Mesh sensitivity study from Bo et al. Three different meshing strategies are presented [83].

Liu et al. [83] found that the simulation results remained within an acceptable prediction range across all mesh types. Typically, key friction and heat transfer parameters showed deviations within 10-20%. This demonstrated low sensitivity to mesh resolution. Based on these findings, the present PhD study adopts a mesh resolution similar to Mesh-3.

3.3 New developments

To further enhance the capability of SubChCFD for broader applications in complex reactor thermal hydraulics, particularly in scenarios encountered in SCWRs, this PhD study focuses on several key development objectives, including mixed convection of supercritical fluids, rod bundles with wire-wrap spacers and natural convection loops.

The development of SubChCFD for supercritical conditions focuses on accounting for thermal property variations and buoyancy effects. Different Nusselt number correlations and friction factor correlations were implemented to address the strong variation of physical properties near the pseudo-critical region. A buoyancy correction term was also incorporated into the Nusselt number formulation to capture buoyancy influenced heat transfer effects.

The wire-wrapped rod bundle case introduces additional complexity due to secondary flow induced by helical wire spacers. The key development of SubChCFD development for this case includes representing wire-induced flow behaviour by including additional momentum source terms to account for wire-wrapped effects.

For the NCL case, the emphasis is on predicting flow stability and circulation dynamics under buoyancy-driven conditions. The methodology incorporates flow regime transition modelling from laminar to turbulent, accounts for the thermal boundary development through Nusselt number calibration, and includes modelling of the flow over an elbow by implementing shear stress in the elbow regions.

Each of the development efforts contributes to the advancement of SubChCFD as a predictive tool for nuclear thermal-hydraulics under various operational conditions. The detailed methodology for each case will be presented in its respective chapter.

Chapter 4

Development and application of SubChCFD for supercritical fluid heat transfer

4.1 Introduction

Numerical simulation under supercritical conditions presents challenges due to the influence of variable thermal physical properties and buoyancy effects. Near the pseudo-critical point, steep gradients in properties such as specific heat, density, and viscosity can significantly affect both flow behaviour and heat transfer performance. This chapter presents the development of the SubChCFD for application in supercritical thermal-hydraulic scenarios.

Empirical correlations identified in the literature are employed to account for the effects of variable thermal physical properties and buoyancy. The development aims to provide a reasonably accurate yet computationally efficient approach. Model validations have been carried out using two approaches: comparison with resolved CFD simulations and prediction of thermal behaviour against experimental data.

4.2 Methodology

As introduced in Chapter 3, the original SubChCFD implementation employs the Dittus–Boelter equation to calculate the Nusselt number, which is then used to determine the wall temperature during the post-processing stage. In this development, a series of Nusselt number correlations are investigated. In the literature review, various correlations have been evaluated for supercritical flow conditions. In this chapter, the Nusselt number correlation proposed by Jackson [58], which is a mod-

ified Krasnoshchekov and Protopopov's correlation [9] has been selected for forced convection with strong variable properties but without the effect of buoyancy. This choice was made because of this correlation's extensive validation, applicability to a wide range of supercritical conditions, and demonstrated accuracy in predicting heat transfer near the pseudo-critical point. Unlike many conventional correlations, Jackson's correlation effectively accounts for the strong property variations characteristic of supercritical fluids. The correlation is expressed as:

$$Nu_f = 0.0183\,\mathrm{Re}_b^{0.82} Pr_b^{0.5} \left(\frac{\rho_w}{\rho_b}\right)^{0.3} \left(\frac{\bar{c}_p}{c_{pb}}\right)^n \tag{4.1}$$

where the average specific heat $\bar{c}_p$, is defined as:

$$\bar{c}_p = \frac{1}{T_w - T_b} \int_{T_b}^{T_w} c_p \, dT = \frac{h_w - h_b}{T_w - T_b} \tag{4.2}$$

Properties with the subscript w refer to values at the wall, while those with b represent the bulk fluid properties. To ensure accurate representation of fluid behaviour near the pseudo-critical temperature, where thermal physical properties vary sharply, all property values are obtained from a pre-generated table based on the NIST database [78]. The exponent n is defined based on the temperature range:

$$n = \begin{cases} 0.4, & T_b < T_w \leq T_{pc} \,\text{or}\, 1.2T_{pc} < T_b \leq T_w, \\ 0.4 + 0.2\left(\frac{T_w}{T_{pc}} - 1\right), & T_b \leq T_{pc} < T_w, \\ 0.4 + 0.2\left(\frac{T_w}{T_{pc}} - 1\right)\left[1 - 5\left(\frac{T_b}{T_{pc}} - 1\right)\right], & T_{pc} < T_b \leq 1.2T_{pc} \,\text{and}\, T_b < T_w. \end{cases} \tag{4.3}$$

where T_{pc} is the pseudo-critical temperature.

Besides, the correlation proposed by Bishop et al. [17] is also investigated, which is expressed as:

$$Nu_b = 0.0069 Re_b^{0.9} Pr_b^{0.66} \left(\frac{\rho_w}{\rho_b}\right)^{0.43} \left(1 + 2.4\frac{D}{x}\right) \tag{4.4}$$

In the implementation, x represents the axial distance from the beginning of the heated section. This value is updated along the axial direction as the flow develops, allowing the correlation to account for the entrance effect on heat transfer.

The Nusselt number correlation presented above does not explicitly account for buoyancy effects, which are particularly important in strong buoyancy effect conditions. To further develop the SubChCFD, a buoyancy correction is introduced to calibrate the Nusselt number.

Based on the work of Jackson et al. [82], the ratio of the mixed convection Nusselt number (Nu) to the forced convection Nusselt number (Nu_f) is implicitly related to the buoyancy parameter (Bo^*) by the following equation which has been discussed in the literature review chapter:

$$\frac{Nu}{Nu_f} = \left\| 1 \pm 2.5 \times 10^5 \, Bo^* \left[\frac{Nu}{Nu_f} \right]^{-2} \right\|^{0.46} . \tag{4.5}$$

The buoyancy parameter (Bo^*) is a dimensionless quantity that quantifies the relative impact of buoyancy forces in the system and is defined as:

$$Bo^* = \frac{Gr^*}{\mathrm{Re}^{3.425}\,\mathrm{Pr}^{0.8}}, \tag{4.6}$$

where the modified Grashof number (Gr^*) is given by:

$$Gr^* = \frac{\beta g D^4 q_w}{\lambda \nu^2}. \tag{4.7}$$

The relationship between the buoyancy parameter (Bo^*) and the Nusselt number ratio (Nu/Nu_f) is illustrated in Figure 4.1. This figure highlights the influence of buoyancy effects on heat transfer under mixed convection conditions, distinguishing between upward and downward flow regimes.

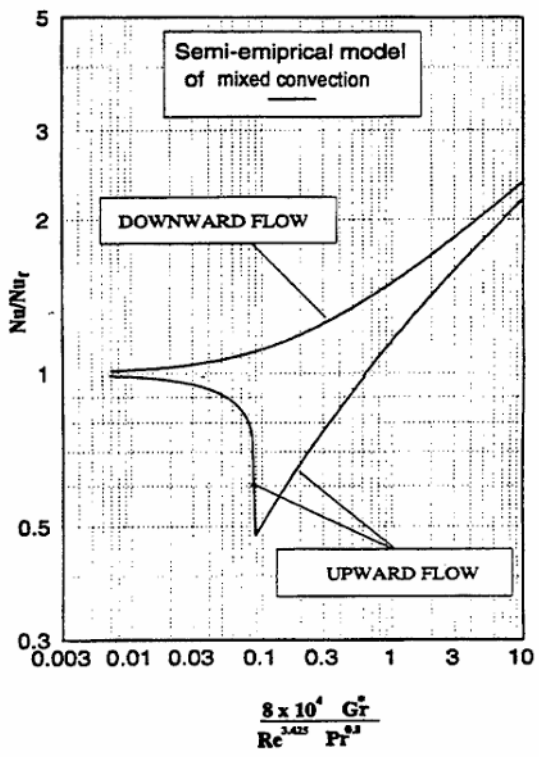

Figure 4.1: Effect of the buoyancy parameter on the Nusselt number ratio for mixed convection [82].

This correlation effectively captures the influence of buoyancy on heat transfer but was originally derived for subcritical fluids rather than supercritical conditions. To further investigate this relationship, He et al. [50] analysed the performance of various turbulence models in predicting buoyancy effects under supercritical conditions. Figure 4.2 presents the results of these comparisons, showing that the overall trends align with those observed in mixed convection such as the laminarization and recovery stages.

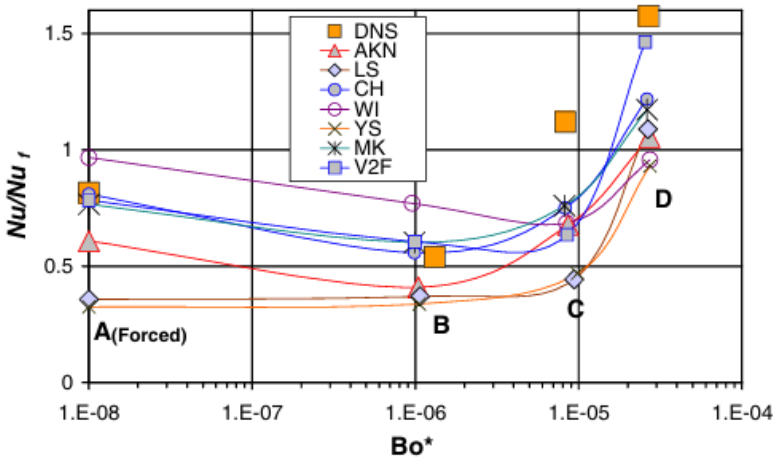

Figure 4.2: Comparison of different turbulence models for the relation between Bo^* and Nu/Nu_f under supercritical conditions [50].

The blue curve in Figure 4.3 represents the buoyancy correction proposed by Jackson, which is commonly employed for mixed convection. The red curve, on the other hand, is derived from He et al.'s research, which refines Jackson's correlation by calibrating it to align with DNS results for supercritical conditions. This comparison highlights the difference between the buoyancy effects in sub-critical air flow and supercritical fluid flow, particularly in the transition to laminarization and recovery stages. Although Jackson's correlation was developed for subcritical turbulent flow, it remains useful for supercritical conditions when properties are evaluated locally and buoyancy/acceleration effects are included; within those bounds, it provides baseline accuracy that can be verified and, if necessary, calibrated against supercritical data. For the implementation in SubChCFD, both corrections are considered to evaluate their applicability under supercritical conditions. These buoyancy corrections allow the SubChCFD to directly account for the buoyancy effect, potentially improving the performance of heat transfer predictions under supercritical conditions.

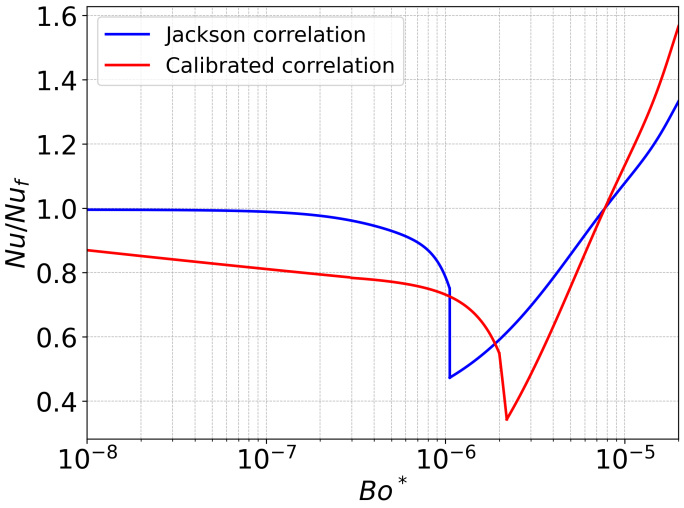

Figure 4.3: Comparison of buoyancy corrections approach.

It is useful noting that the thermal entrance effect is only accounted for in the Bishop correlation which however does not explicitly consider the buoyancy effect. In this study, two new correlations are implemented: (1) Bishop + Calibrated, and (2) Calibrated + Entrance correction, expressed as $(1 + 2.4D/x)$. A summary of the correlations discussed in this chapter is summarised in Table 4.1. Unless otherwise specified, K&P is used as the baseline model.

Table 4.1: Summary of heat-transfer correlations discussed in this chapter

Model	**Description**	**Range of applicability**
Dittus–Boelter [37]	Correlation used in original SubChCFD and used for forced convection without property variation	Subcritical pressures
K&P [58]	Jackson modified Krasnoshchekov and Protopopov correlation by incorporating property variation, and used for forced convection.	$8\times10^4 < \mathrm{Re}_b < 5\times10^5$ $0.85 < \overline{\mathrm{Pr}}_b < 65$ $0.02 < \dfrac{\overline{c_p}}{c_{p,b}} < 4$ $1.00 < \dfrac{\rho_w}{\rho_b} < 6.00$ $0.9 < \dfrac{T_w}{T_{pc}} < 2.5$ $4.6\times10^4 < q < 2.6\times10^6\ \mathrm{W\,m^{-2}}$
Bishop [17]	Includes thermal entrance effect $(1 + 2.4D/x)$.	P : 22.8 − 27.6 MPa, G : 651 − 3662 $\mathrm{kg\,m^{-2}\,s^{-1}}$, q : 310 − 3460 $\mathrm{kW\,m^{-2}}$.
Jackson [82]	K&P correlation with Jackson buoyancy correction	$8\times10^4 < \mathrm{Re}_b < 5\times10^5$ $0.85 < \overline{\mathrm{Pr}}_b < 65$ $0.02 < \dfrac{\overline{c_p}}{c_{p,b}} < 4$ $1.00 < \dfrac{\rho_w}{\rho_b} < 6.00$ $0.9 < \dfrac{T_w}{T_{pc}} < 2.5$ $4.6\times10^4 < q < 2.6\times10^6\ \mathrm{W\,m^{-2}}$
Calibrated	K&P correlation with calibrated Jackson buoyancy correction fitted to DNS data.	
Bishop + Calibrated	Bishop correlation combined with calibrated Jackson correction.	
Calibrated + Entrance	K&P with calibrated Jackson buoyancy correction and thermal entrance effect.	

In addition to the heat transfer correlation, corrections are also considered to the friction factor correlations in this study. Two empirical correlations from the literature are examined to evaluate their applicability under supercritical conditions. The first is Kirillov's correlation [69], expressed as:

$$f_{\text{non-iso}} = f_{\text{iso}} \left(\frac{\rho_w}{\rho_b} \right)^{0.4}, \quad \text{for } 8 \times 10^4 < \mathrm{Re} < 1.5 \times 10^6 \tag{4.8}$$

The second is proposed by Yamashita et al. [138]:

$$f_{\text{non-iso}} = f_{\text{iso}} \left(\frac{\mu_w}{\mu_b} \right)^{0.72} \tag{4.9}$$

Both correlations are applied as corrections to the isothermal friction factor f_{iso}, which is used in the original SubChCFD formulation, to account for non-isothermal effects associated with strong property variations near the pseudo-critical point. It might be attempting to combine the above two equations to consider the effects of variations in the density and viscosity. However, this is not done to avoid potential double-counting of the effects.

4.3 Test cases and SubChCFD model setup

4.3.1 Physical Model and Experimental Configuration

The test cases studied in this chapter are all based on the same 2×2 bare rod bundle configuration as that used in Wang et al. [126], and they are all upward flow. Four groups of test cases have been conducted to cover a broad range of thermal-hydraulic conditions:

(1) **Group A:** These cases follow the reference configuration and boundary conditions provided in the ECC-SMART project [38].

(2) **Group B:** These cases are designed to investigate the influence of buoyancy by reducing the mass flow rate and using different inlet temperatures.

(3) **Group C:** Simulations are carried out to study the performance of different friction factor correlations under supercritical conditions.

(4) **Group D:** These cases are used to validate the model against experimental measurements from Wang et al. [126].

The experimental test section consists of a 2×2 bare rod bundle enclosed within a square duct with rounded corners, as illustrated in Figure 4.4. The duct has an outer width of 23.03 mm and a total length of 600 mm. Each rod has an outer diameter of 8 mm and a wall thickness of 1.5 mm. The rod pitch is 9.44 mm, resulting in a minimum gap of 1.44 mm between adjacent rods and the inner wall of the duct.

To monitor the thermal and flow behaviour within the test section, thermocouple measurement points (mp-1 to mp-5) are distributed along the axial length of the assembly. These points capture temperature variations at various axial locations. The cross-sectional view (A-A) in Figure 4.4 illustrates the arrangement of the heated rods, thermocouples, and flow channels. These thermocouples are placed at different positions to capture localized temperature variations around the bundles.

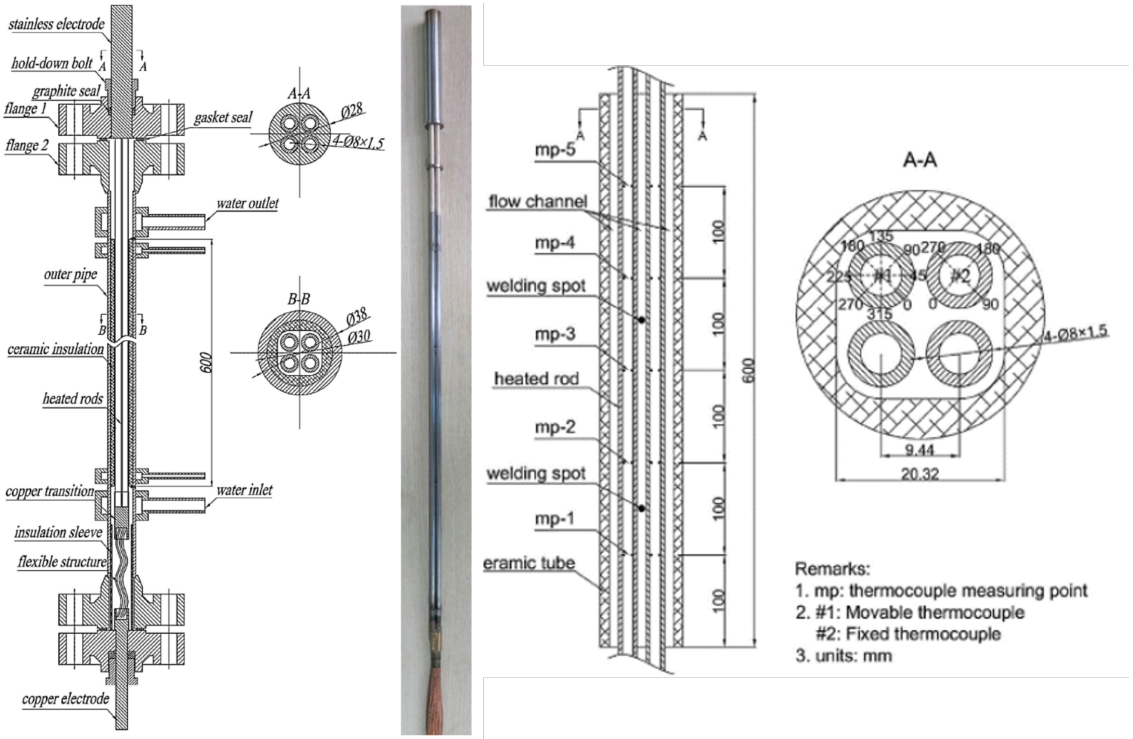

Figure 4.4: Schematic of the experimental rig [38].

4.3.2 Numerical modelling and mesh

For both the resolved CFD and SubChCFD simulations, a 2D cross-sectional mesh is first generated using ANSYS ICEM CFD. The 3D mesh is then constructed by extruding the 2D mesh along the axial direction.

In the resolved CFD simulation, one-eighth of the test section is modelled to reduce computational costs, taking advantage of the symmetry of the geometry and flow characteristics, as shown in Figure 4.5. The k-ω SST turbulence model is employed, which has been extensively validated in the literature for turbulent flows under supercritical conditions [86, 96]. A high-resolution structured computational mesh is generated, with the first layer of cells near the walls refined to maintain $y^+ < 1$, ensuring proper resolution of buoyancy-induced effects in the boundary layer.

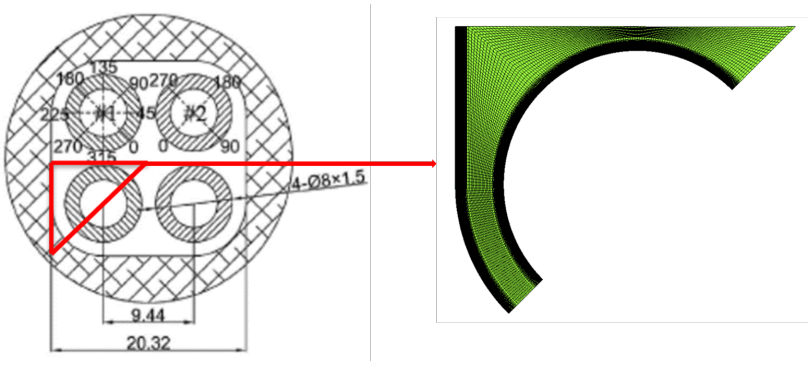

Figure 4.5: Mesh in resolved CFD.

Heat conduction in the solid rod walls is not considered to maintain consistency with the SubChCFD framework assumptions. The effect of conduction in this problem is thought to be secondary, and this simplification enables the study of convective heat transfer mechanisms while reducing computational costs.

For SubChCFD, the 2D cross-sectional mesh is shown in Figure 4.6. The coarse computing mesh in the cross-section is designed for the CFD solver. The entire section is divided into subchannels of three distinctive types: center, edge, and corner subchannels. These subchannels are utilized in the SubChCFD for the calculation of sub-channel quantities.

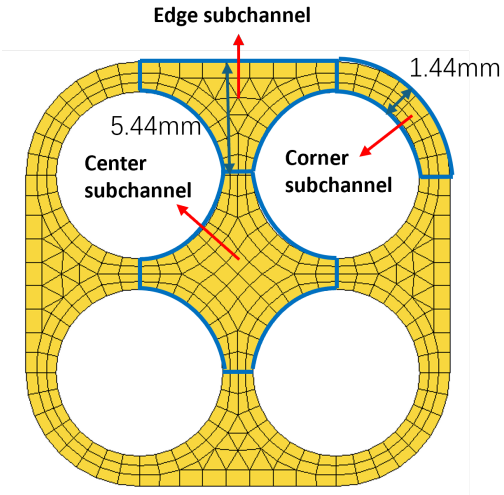

Figure 4.6: Mesh used in SubChCFD.

Both the SubChCFD and resolved CFD approaches utilize the same computational domain and axial extent. The total computational domain spans 660 mm in length, consisting of a heated test section and unheated buffer sections at both ends. Each buffer section extends 10 hydraulic diameters, as shown in Figure 4.7.

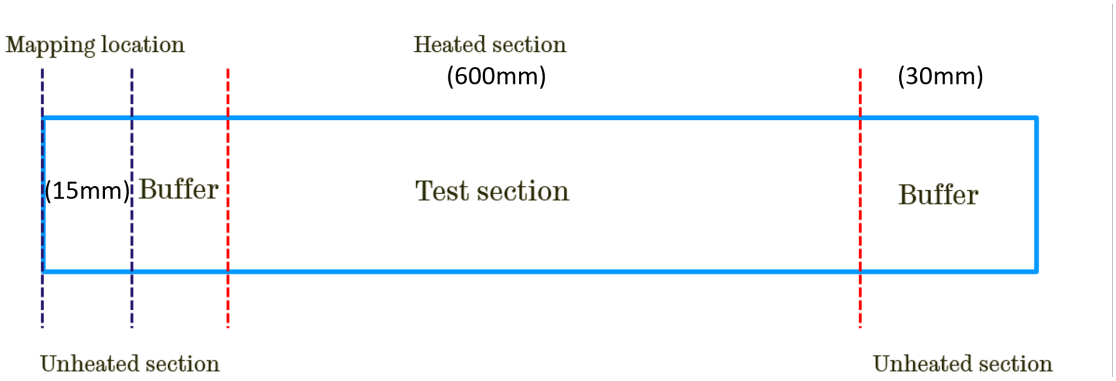

Figure 4.7: Computational domain layout.

To ensure the flow is fully developed before entering the heated section, a mapped inlet method is applied within the inlet buffer section. The mapping plane is situated at the centre of this section. Flow properties are extracted from this location and reapplied at the inlet, creating a pseudo-periodic boundary condition that produces fully developed flow. This method allows for an accurate representation of fully developed inflow conditions without requiring a long upstream computational domain.

The outlet buffer section serves a different purpose. It prevents the flow and temperature fields within the test section from being influenced by the potential numerical disturbances resulting from the outlet boundary condition.

A fine mesh consisting of approximately 35.2 million cells over one-eighth of the geometry is used in the resolved CFD simulation, while the SubChCFD simulation covers the full domain with a significantly coarser mesh of only 0.26 million cells.

4.3.3 Simulation condition

Firstly, the study begins by simulating two cases from the ECC-SMART project [38]. The operating conditions for these cases are summarized in Table 4.2. While all cases share the same geometric configuration, they differ in key operating parameters such as pressure, mass flow rate, heating power, and inlet temperature. These differences lead to variations in the Reynolds number and buoyancy parameter, resulting in different buoyancy effects. The Re and Bo^* in Table 4.2 are based on the inlet conditions.

Table 4.2: Operating conditions for group A.

Case	$\boldsymbol{P}$ (MPa)	$\boldsymbol{G}$ (kg/m^{2}s)	$\boldsymbol{q''}$ (kW/m^2)	$\boldsymbol{T}_{\text{in}}$ (°C)	**Re**	$\boldsymbol{Bo^*}$
Case 1	23.01	676.6	203.4	372.24	35028	8.48×10^{-8}
Case 2	22.89	723.4	192.3	390.06	74689	4.73×10^{-9}

Both cases are simulated under supercritical conditions, with operating pressures slightly above the critical pressure of water. While the mass flow rate and heating power are similar in both cases, the inlet temperatures vary significantly, leading to distinct thermal-hydraulic behaviours.

In Case 1, the inlet temperature is 372.24 °C, which is slightly below the pseudo-critical temperature of water at 23.01 MPa (377.51 °C). As the flow heats up within the test section, it is expected to undergo significant property variations, leading to pronounced heat transfer enhancement due to the sudden increase of c_p near the pseudo-critical region.

In Case 2, the inlet temperature is 390.06 °C, which is above the pseudo-critical temperature. Under these conditions, fluid properties remain relatively stable with less drastic variations. The absence of strong pseudo-critical property gradients is expected to result in a smoother thermal response and weaker buoyancy effects.

The contrast in inlet temperatures between these cases provides an opportunity to analyse the impact of crossing the pseudo-critical region on flow behaviour and heat transfer characteristics.

In addition to the conditions from the ECC-SMART project, three cases are designed to investigate the buoyancy effect and validate the buoyancy correction implementations. All cases are conducted using supercritical water at a pressure of 25 MPa. Under this pressure, the pseudo-critical temperature is approximately 385 °C. The applied heat flux is the same across all cases. Case 4 and Case 5 use half the mass flux of Case 3 in order to enhance the buoyancy effect. While both Case 4 and Case 5 share the same mass flux, but differ in inlet temperature.

Table 4.3: Flow conditions for Group B.

Case	$\boldsymbol{P}$ (MPa)	$\boldsymbol{G}$ (kg/m^{2}s)	$\boldsymbol{q''}$ (kW/m^2)	$\boldsymbol{T}_{\text{in}}$ (°C)	**Re**	$\boldsymbol{Bo^*}$
Case 3	25.0	700	200	380	39168	6.94×10^{-8}
Case 4	25.0	350	200	380	19581	7.45×10^{-7}
Case 5	25.0	350	200	384	18730	1.33×10^{-6}

Case 6 and Case 7 are designed to investigate the effect of different friction factor correlations.

Table 4.4: Flow conditions for group C.

Case	$\boldsymbol{P}$ (MPa)	$\boldsymbol{G}$ (kg/m^{2}s)	$\boldsymbol{q''}$ (kW/m^2)	$\boldsymbol{T}_{\text{in}}$ (°C)	**Re**	$\boldsymbol{Bo^*}$
Case 6	23.01	700	200	372.24	36278	7.4×10^{-8}
Case 7	23.01	350	200	372.24	18139	7.94×10^{-7}

Cases from Wang's study [126] are considered as additional demonstration cases. These cases include experimental data, which serve as reference points to demonstrate the capability of the SubChCFD method. The operating conditions for these cases are summarised in Table 4.5.

These cases share the same operating pressure of 25 MPa but vary in mass flow rate and inlet temperatures. The inlet temperatures span multiple values (380 °C, 382 °C, 384 °C, and 385 °C) to capture the sensitivity of the system to small thermal changes. Case 8 and case 9 represent higher and lower mass flow rates with the same heating power. By comparing the simulation results with experimental data, these cases provide an additional benchmark to evaluate the robustness of the SubChCFD approach.

Table 4.5: Operating conditions for group D.

Case	$\boldsymbol{P}$ (MPa)	$\boldsymbol{G}$ (kg/m^{2}s)	$\boldsymbol{q''}$ (kW/m^2)	$\boldsymbol{T}_{\text{in}}$ (°C)
Case 8	25.0	700	200	380, 382, 384, 385
Case 9	25.0	350	200	380, 382, 384, 385

4.4 Results and discussion

4.4.1 Group A - ECC-SMART project cases

Figure 4.8 presents the axial variation of the buoyancy parameter (Bo^*) for Case 1 and Case 2, calculated using cross-sectional bulk flow properties obtained from the resolved CFD results. The values of Bo^* remain relatively small for both cases, indicating a limited overall influence of buoyancy.

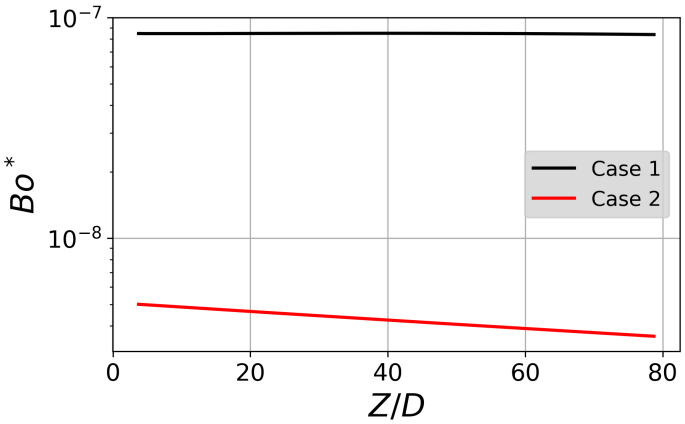

Figure 4.8: Axial variation of the buoyancy parameter (Bo^*).

Figure 4.9 presents the predicted wall temperature (T_w) at three angular positions along the axial direction, expressed in terms of the dimensionless location z/D. These positions correspond to subchannel regions: center, edge, and corner. It should be noted that for both Case 1 and Case 2, only the correlation accounting for variable physical properties has been implemented. The buoyancy effects in these cases are small and thus ignored. The results obtained from SubChCFD are compared with those from resolved CFD to evaluate model performance.

The results show that SubChCFD predictions align well with resolved CFD results except for the corner subchannel in Case 1, where the SubChCFD produces much lower temperature than the resolved CFD. The most significant temperature rise occurs in the early axial region ($Z/D < 10$), which is attributed to the entrance effect.

For both cases, the corner subchannel exhibits a higher temperature due to the narrower flow passage, where velocity is reduced by the combined effect of wall shear stress from both the housing wall and rod wall. In Case 1, the temperature rise rate at the corner subchannel is lower than that in Case 2, indicating an enhancement in heat transfer when the inlet temperature is close to the pseudo-critical temperature. This behaviour is attributed to the peak in specific heat capacity (C_p) near the pseudo-critical point, which allows the fluid to absorb more thermal energy with a smaller increase in temperature. Since the inlet temperature of Case 2 exceeds the pseudo-critical temperature, there is no sharp peak in C_p. Instead, C_p continues to decrease along the flow direction. As a result, the temperature rise is more pronounced compared to Case 1.

For Case 1, the flow experiences drastic property variations as it passes through the pseudo-critical temperature region. SubChCFD predictions suggest that the implemented correlation, which accounts for variable thermal physical properties, has the capability to capture the key thermal phenomena of supercritical flow near the pseudo-critical temperature. SubChCFD is able to predict the overall wall temperature profile along the axial direction across different subchannels.

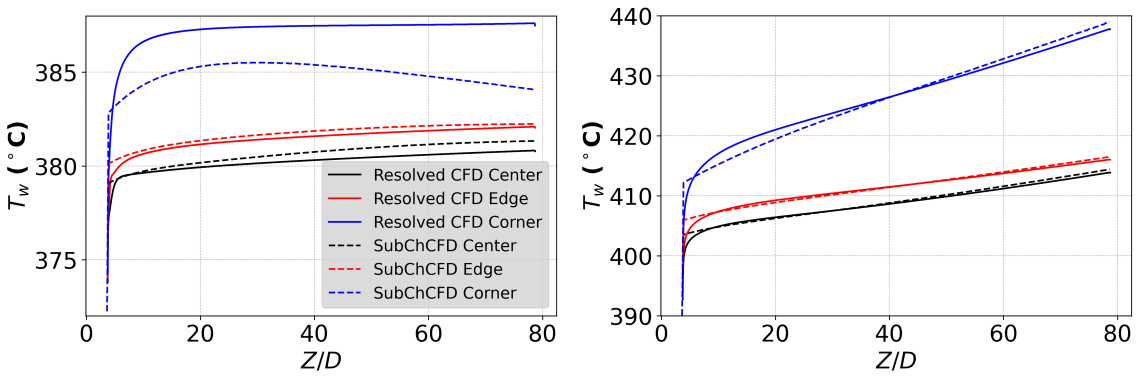

(a) Case 1.

(b) Case 2.

Figure 4.9: Comparison of wall temperature distributions for Case 1 and Case 2.

However, in Case 1, the wall temperature profile in the corner subchannel exhibits a small peak that deviates from the resolved CFD results. This may be attributed to the model's sensitivity to the applied heat transfer correlation. Secondly, the wall temperature profile predicted by SubChCFD in the corner subchannel shows an underprediction compared to the resolved CFD results. This discrepancy may be attributed to the lack of a buoyancy correction, which will be further developed in the following sections.

Figure 4.10 presents the fluid temperature distribution across the edge subchannel and the center subchannel at different axial locations for Case 1 and Case 2. The agreement between the subchCFD and the resolved CFD is exceptionally well, demonstrating the ability of the SunChCFD capturing some local distribution which cannot be done by traditional subchannel code. The temperature profiles show approximately a symmetric distribution and distinct peaks in the middle, where it is between the heated rods, due to stronger localized heating and slower flow.

The difference in the evolution of temperature distribution across the edge and center subchannels between the two cases is also influenced by the variation in thermophysical properties of the fluid near the pseudo-critical temperature, as discussed earlier. In Case 1, the temperature profiles exhibit a more uniform distribution, while in Case 2, the temperature rise rate is more pronounced. This predicted behaviour is consistent with the previously discussed effects of specific heat variation, where Case 1 benefits from enhanced heat absorption near the pseudo-critical region, leading to a smoother thermal development.

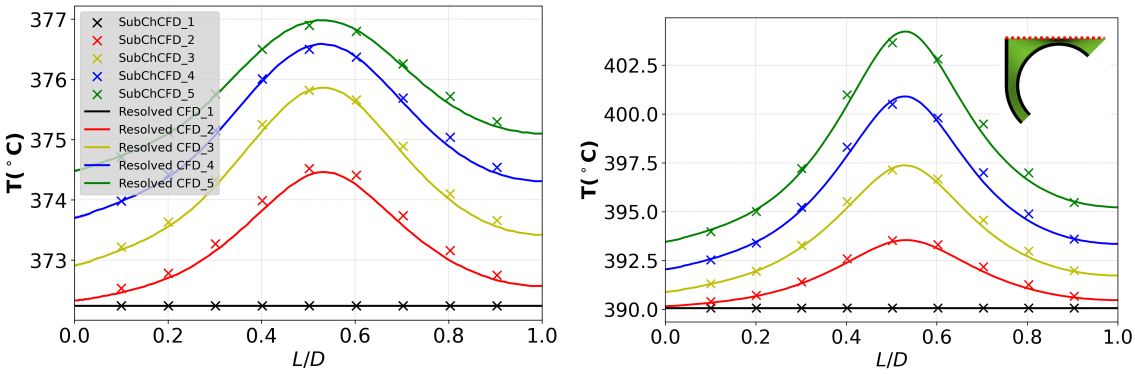

(a) Case 1.

(b) Case 2.

Figure 4.10: Comparison of temperature distributions for Case 1 and Case 2. 1, 2, 3, 4 and 5 represent the cross sections axial location at 0.03m, 0.18m, 0.33m, 0.48m and 0.63m

Figure 4.11 presents the velocity distributions across the edge and center subchannels for Case 1 and Case 2. In both cases, the velocity decreases in the central region due to flow redistribution driven by local shear effects. The peak velocities are observed in the center subchannel, where the fluid experiences reduced wall shear stress effect, allowing for higher velocities. Case 2 exhibits a more uniform velocity distribution, whereas Case 1 shows a more irregular acceleration pattern. This discrepancy is attributed to the sharp decrease in density near the pseudo-critical temperature in Case 1, which results in a reduction in velocity in the downstream region.

The comparison between SubChCFD and Resolved CFD shows reasonable agreement, confirming that the SubChCFD approach can effectively capture velocity distributions across different subchannels. The 10% error bars associated with SubChCFD predictions highlight the expected uncertainty due to the coarse mesh resolution. Despite this, the results remain consistent with resolved CFD trends, demonstrating the capability of SubChCFD to predict flow behaviours under supercritical conditions.

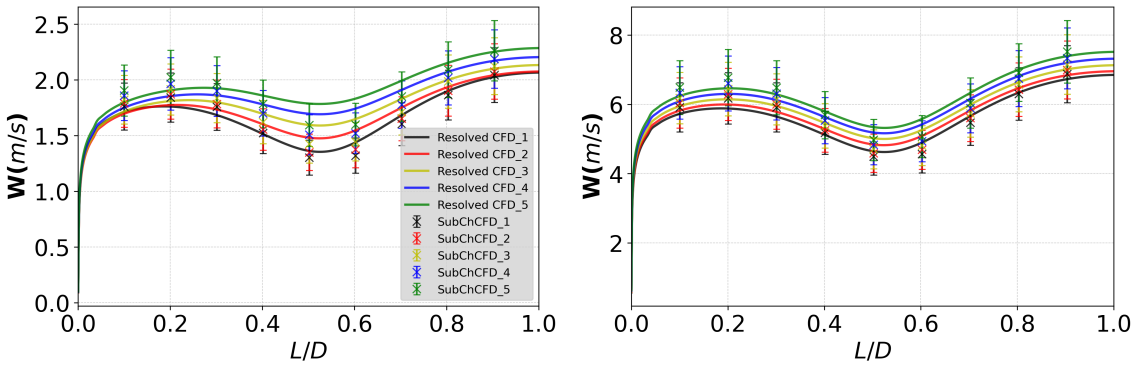

(a) Case 1. (b) Case 2.

Figure 4.11: Comparison of velocity distributions for Case 1 and Case 2.

Figure 4.12 presents the axial pressure drop for Case 1 and Case 2, comparing the predictions from the Resolved CFD approach and the SubChCFD model. The results show good agreement between the two methods, with the pressure drop percentage difference remaining within approximately 5% for both cases, indicating that the correlations used in the SubChCFD captures the overall pressure drop trend in supercritical conditions.

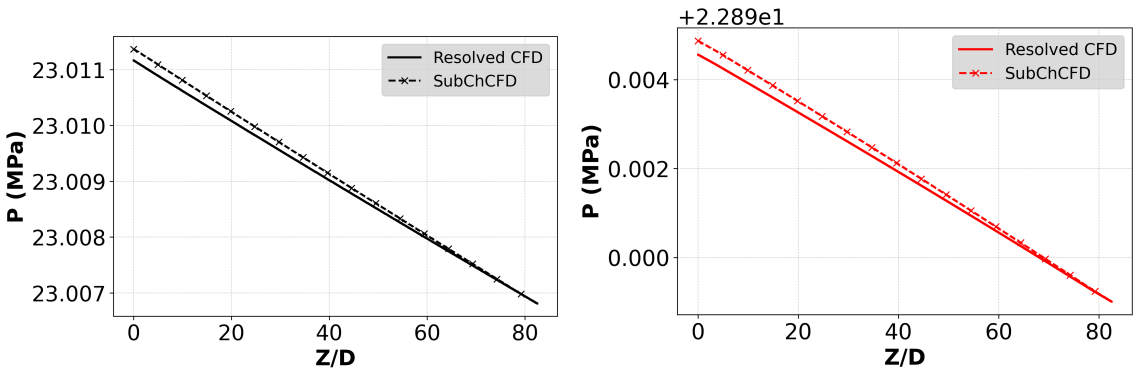

(a) Case 1. (b) Case 2.

Figure 4.12: Comparison of pressure drop for Case 1 and case 2.

Overall, the SubChCFD provides reasonable predictions of heat transfer, subchannel flow redistribution, and pressure drop in supercritical conditions with preliminary development. While it performs well, further refinements are necessary to enhance its capability in capturing buoyancy-driven flow phenomena, particularly in scenarios where buoyancy effects become more significant.

4.4.2 Group B - Modified ECC-SMART project cases

Buoyancy effects play a critical role in influencing heat transfer and flow behaviour under supercritical conditions. To investigate their impact on flow redistribution across different subchannels, Case 3 and Case 4 are set up, representing scenarios with relatively weak and strong buoyancy effects, respectively.

Figure 4.13 presents the axial variation of the buoyancy parameter (Bo^*) across different subchannels for two cases. It is evident that Case 4 exhibits a significantly stronger buoyancy effect compared to Case 3, as reflected in the overall higher values of Bo^*. In both cases, the corner subchannel consistently experiences the strongest buoyancy effects, followed by the edge and center subchannels.

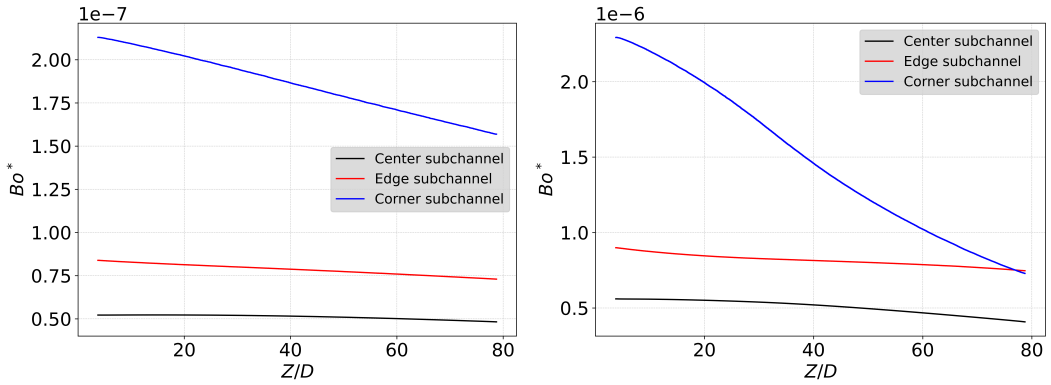

(a) Case 3.

(b) Case 4.

Figure 4.13: Axial distribution of the buoyancy parameter (Bo^*) in different subchannels.

Figure 4.14 presents the axial bulk velocity (U_B) in different subchannels for two cases. The results illustrate how buoyancy influences flow development among the subchannels. In cases 3, where Bo is low, the bulk velocity in each sub-channel increases in parallel with each other, showing the flow being free from the effect of buoyancy. In case 4, the corner subchannel exhibits a noticeable stronger acceleration downstream due to a stronger buoyancy in this sub-channel (see Figure 4.13b. This acceleration contrasts with the center and edge subchannels, where velocity increases more gradually. The observed variations emphasize that stronger buoyancy effects significantly impact flow behaviour, leading to different velocity evolution trends across subchannels.

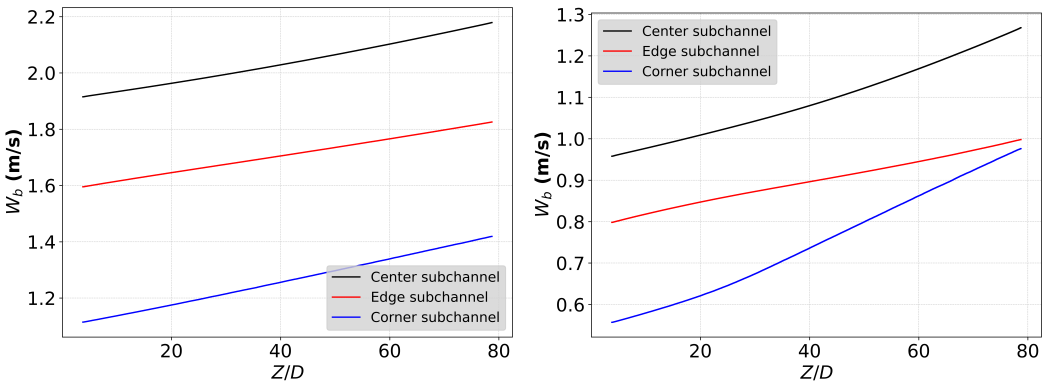

(a) Case 3. (b) Case 4.

Figure 4.14: Axial variation of bulk velocity (U_B) in different subchannels.

Figure 4.15 presents the average axial bulk velocity comparison between SubChCFD and resolved CFD. The bulk velocity is calculated as the cross-sectional average of the axial velocity. Good agreement is observed between SubChCFD and resolved CFD across the flow domain.

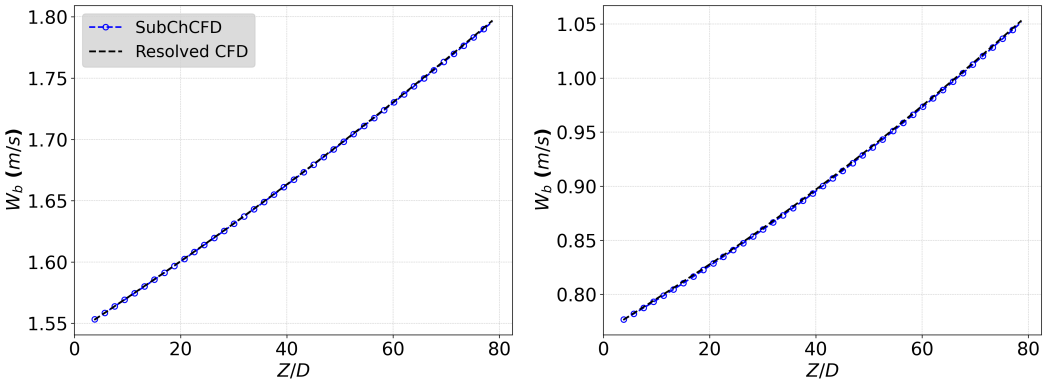

(a) Case 3. (b) Case 4.

Figure 4.15: Average axial bulk velocity comparison.

Figure 4.16 illustrates the axial bulk temperature (T_B) in different subchannels for the cases. In Case 3, the bulk temperature remains below the pseudo-critical point throughout the heated length, and the temperature develeopment in all subchanels are more uniform. In contrast, in the stronger buoyancy effect case (Case 4), the bulk temperature reaches higher values by the end of the heated section, exceeding the pseudo-critical temperature. In the early stage of flow development, the temperature rise rate in corner subchannel is slightly higher.

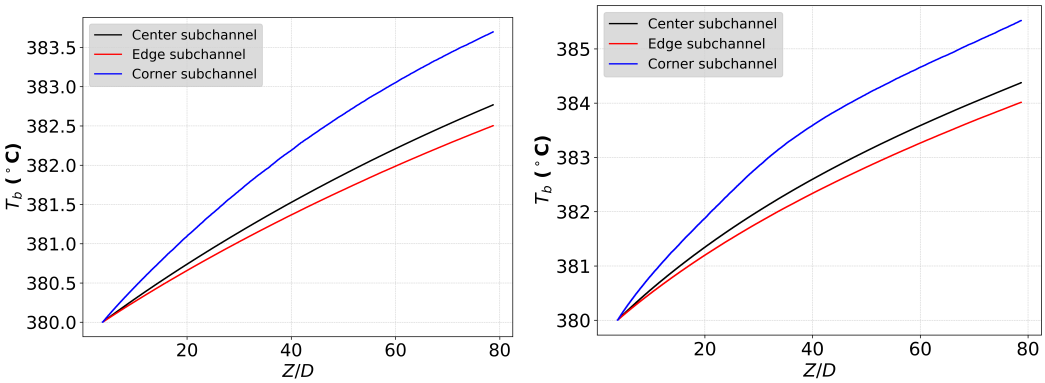

(a) Case 3. (b) Case 4.

Figure 4.16: Axial variation of bulk temperature (T_B) in different subchannels for two cases.

Figure 4.17 presents the comparison of the average axial bulk temperature between SubChCFD and resolved CFD. The bulk temperature is calculated based on an energy-weighted cross-sectional average, accounting for variations in specific heat capacity c_p. The comparison shows great consistency along the axial direction.

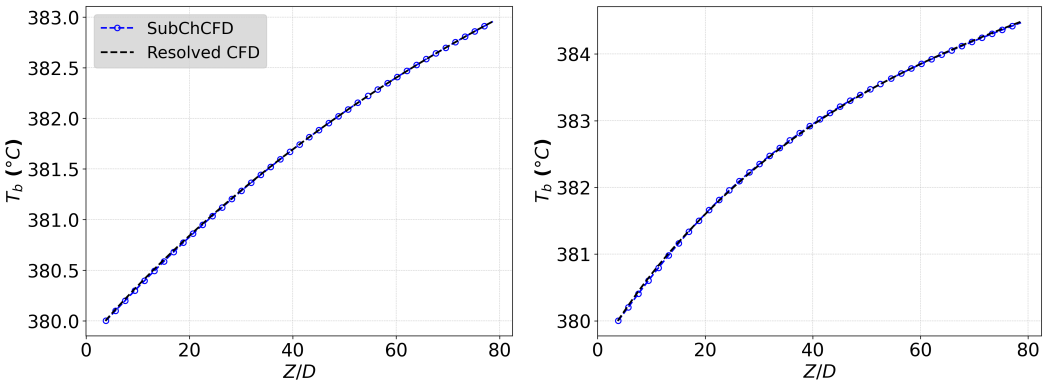

(a) Case 3. (b) Case 4.

Figure 4.17: Average axial bulk velocity comparison.

Figure 4.18 presents the axial variation of the heat transfer coefficient across different subchannels. In Case 3, where the fluid temperature does not reach the pseudo-critical temperature, the heat transfer coefficient exhibits a more gradual increase along the axial direction. Conversely, In Case 4, a noticeable peak in the heat transfer coefficient is observed in the downstream region, primarily due to the local fluid temperature approaching the pseudo-critical temperature. At this point, the c_p reaches a peak, significantly affecting Nusselt number prediction and further enhancing heat transfer. The HTC is the lowest in the corner subchannel and highest in the

central subchannel, consistent to the different Reynolds numbers in these subchannels as implied by the velocity distribution shown in Figure 4.14.

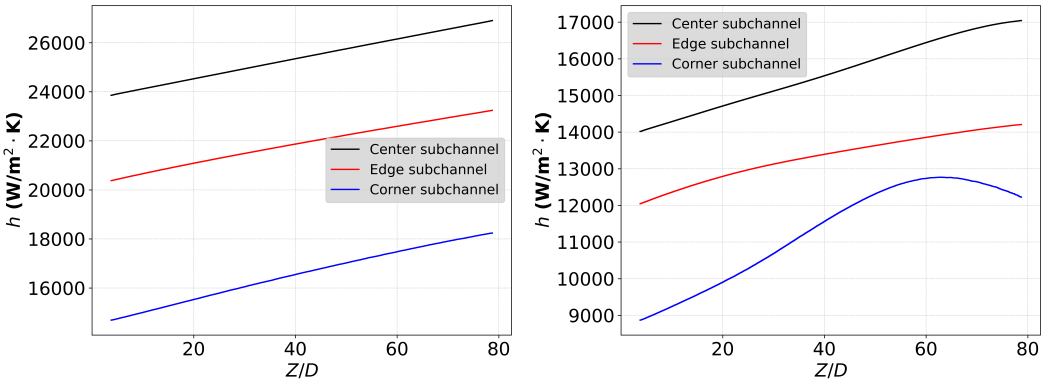

(a) Case 3. (b) Case 4.

Figure 4.18: Comparison of heat transfer coefficient (h) along the axial direction for different subchannels.

The buoyancy effect significantly influences flow development and redistribution across different subchannel regions, affecting both velocity and heat transfer behaviour. The direct impact of buoyancy must be considered with variations in physical properties to accurately capture the flow behaviour in supercritical conditions. The findings highlight the necessity of incorporating buoyancy correction in empirical correlations, particularly for cases with strong buoyancy effects. The following sections will focus on validating buoyancy correction to develop SubChCFD in predicting flow and heat transfer behaviour under strong buoyancy conditions.

As discussed in the literature review and earlier analysis, buoyancy effects become more pronounced at lower mass fluxes cases. To evaluate the buoyancy correction implemented in SubChCFD, this study examines Case 4 and Case 5. Both cases use a lower mass flux of 350 $\mathrm{kg/m^2s}$ and a constant heat flux of 200 $\mathrm{kW/m^2}$. The inlet temperatures are set at 380°C for Case 5 and 384°C for Case 6. The SubChCFD and resolved CFD simulations are presented and compared with each other, aiming to characterize the onset and development of buoyancy-induced heat transfer deterioration, assess its impact on local heat transfer mechanisms, and validate the predictive capability of the SubChCFD approach under strong buoyancy conditions.

Figure 4.19 presents the axial distribution of the buoyancy parameter (Bo^*) for Case 4 and Case 5. The results illustrate that the buoyancy effect is particularly strong in these cases, especially in the corner subchannel.

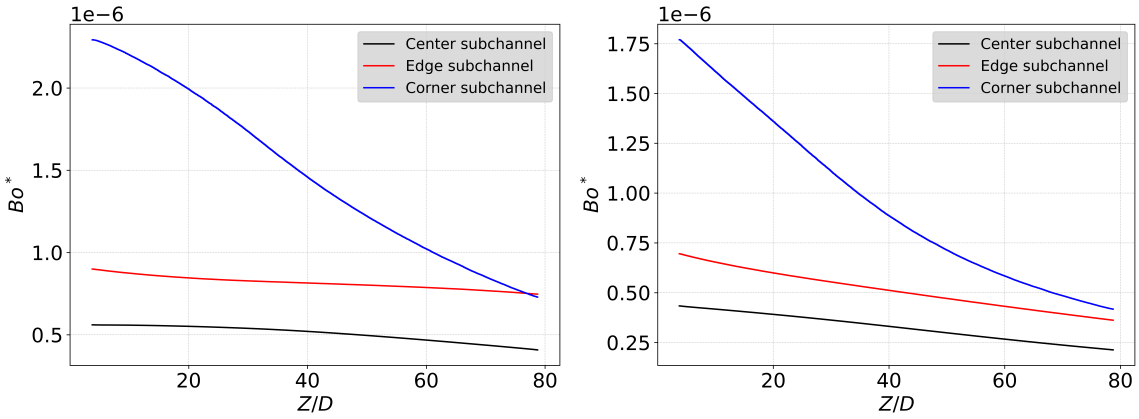

(a) Case 4.

(b) Case 5.

Figure 4.19: Buoyancy parameter (Bo^*) variation along the axial direction.

Figure 4.20 presents the axial distribution of wall temperature in different subchannels for both cases, comparing the performance of various heat transfer correlations. The first row corresponds to Case 4, while the second row represents Case 5. The black lines represent reference data obtained from high-resolution CFD simulations, while the red curves with different markers depict the predictions of different correlations implemented in the SubChCFD.

A distinct wall temperature peak is observed in the corner subchannel, indicating an initial phase of heat transfer deterioration followed by a partial recovery further downstream. Among all correlations, Jackson and the calibrated correlation successfully capture the local heat transfer deterioration, although at different axial locations due to variations in their buoyancy-induced laminarization predictions.

The presence of temperature peaks suggests a response to the buoyancy correction implementation. These peaks arise due to the coarse mesh nature of SubChCFD, where the wall temperature prediction heavily relies on empirical correlations. These correlations are developed for fully developed flow conditions and may not accurately capture the behaviour in the developing region. Despite this limitation, the peaks still provide insight into the axial positions where heat transfer deterioration occurs. Among the correlations, the calibrated model aligns most closely with resolved CFD predictions. Further downstream, as the flow stabilises, all correlations provide reasonable temperature predictions, with the calibrated model remaining the closest to the resolved CFD results in the fully developed stage.

In the edge subchannel, where the buoyancy parameter is lower than in the corner subchannel, all correlations capture the general trend of temperature evolution. The

Jackson and calibrated correlations have better predictions against resolved CFD data compared to the other models.

In the center subchannel, where buoyancy effects are weakest, the Jackson, K & P, and Bishop correlations show good agreement with resolved CFD results. However, the calibrated correlation tends to overpredict the wall temperature, likely due to its stronger buoyancy correction, which is less applicable in this regime.

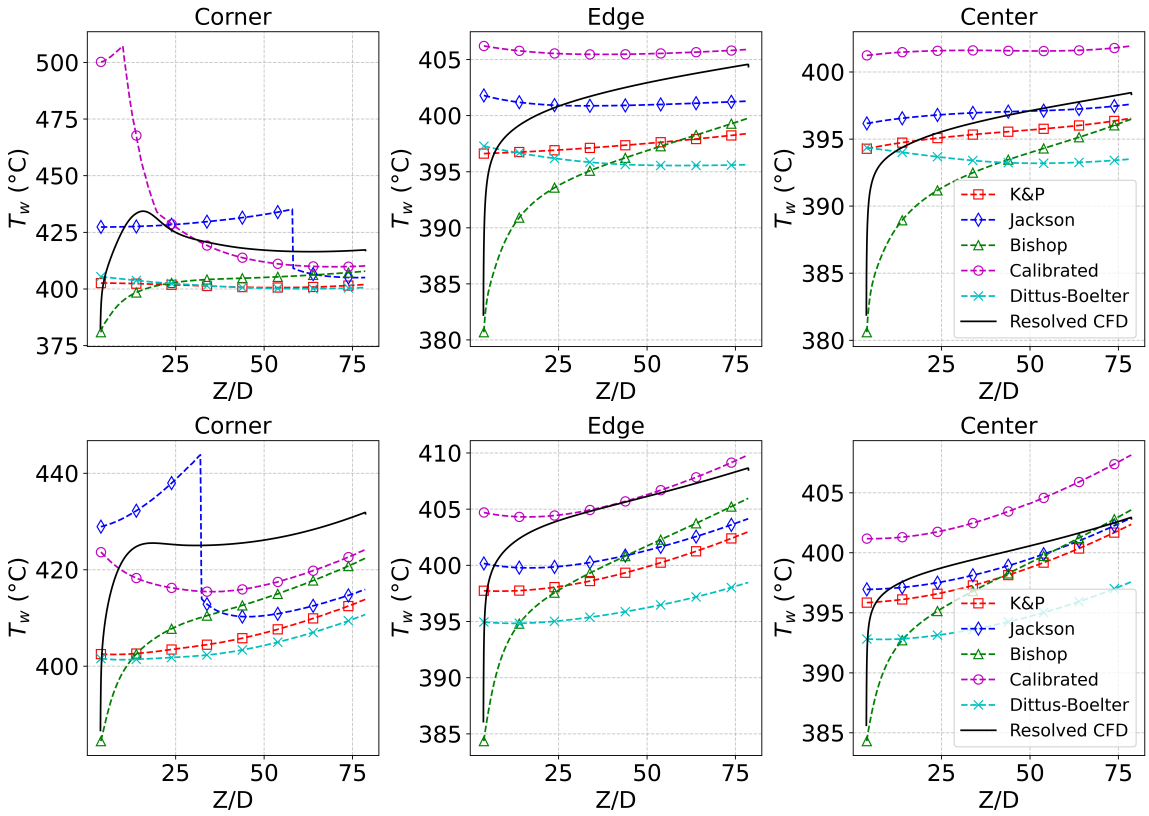

Figure 4.20: Axial variation of wall temperature (T_w) prediction by different correlations in different subchannels: Case 4 (first row); Case 5 (second row).

Overall, all correlations exhibit a similar trend in predictions with resolved CFD, though differences exist in magnitude. Compared to the Dittus–Boelter correlation, all other correlations demonstrate improved performance. The calibrated correlation is best suited for cases with strong buoyancy effects, while the Jackson model performs well across all scenarios. The K & P correlation performs well in cases with weaker buoyancy effects, and the Bishop correlation provides reasonable predictions in all cases. One limitation of all models is their inability to capture entry effects accurately due to the nature of thermal boundary layer development. Instead, they produce an abrupt temperature shift due to the coarse grid resolution. Among them, the

Bishop correlation exhibits a more gradual increase in wall temperature but slightly underpredicts the response to thermal boundary development.

Figure 4.21 shows the axial distribution of wall temperature in different subchannels for Case 4 and Case 5, based on the new combination implementations. Compared to the results using the Bishop correlation shown in Figure 4.20, the Bishop + Calibrated approach predicts slightly higher wall temperatures. This difference is attributed to the response of the Nusselt number ratio to the buoyancy parameter. The predictions in the corner subchannels for both Case 4 and Case 5 are significantly improved, exhibiting trends similar to those observed in the resolved CFD results, which capture the heat transfer deterioration phenomenon. Notably, this trend was not captured when using the original Bishop correlation.

For the Calibrated + Entrance correlation, after accounting for the entrance effect, the predicted wall temperatures show closer agreement with the resolved CFD results. In addition, the moderation of the temperature peak near the entrance suggests improved modelling of the entrance effects during the developing flow stage.

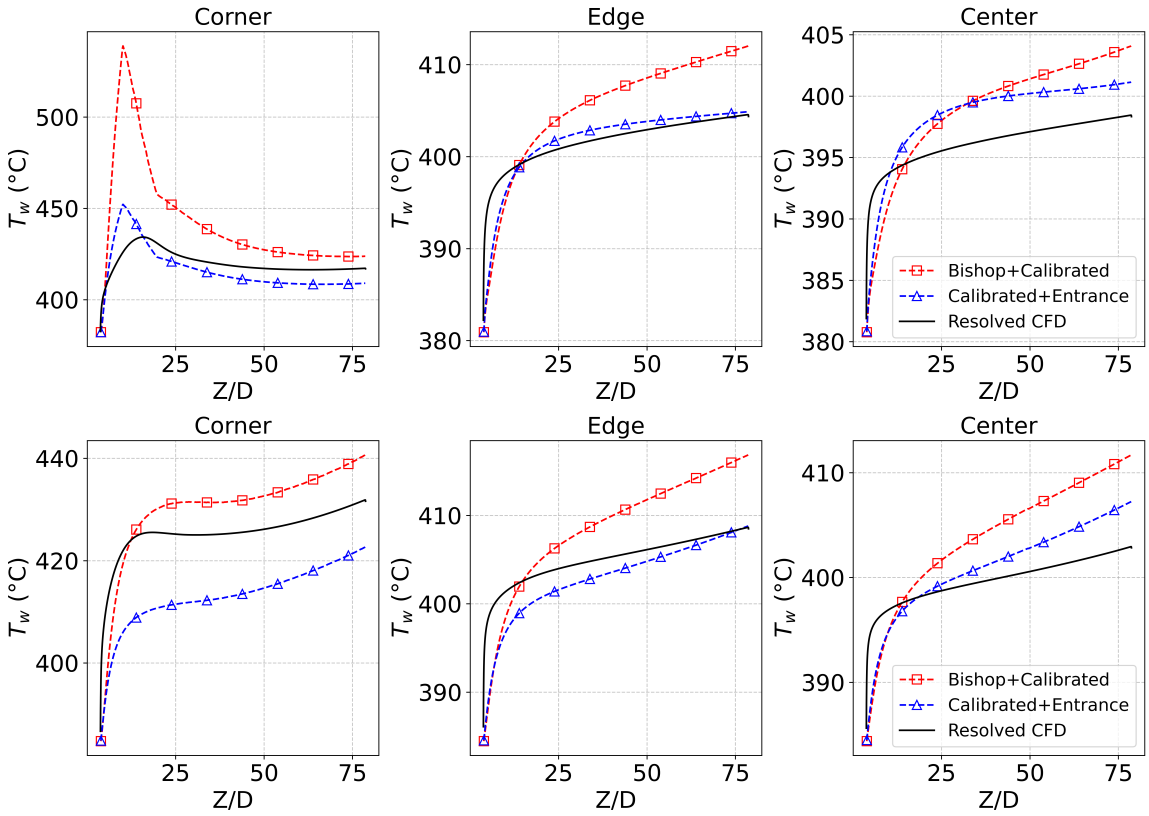

Figure 4.21: Axial variation of wall temperature (T_w) prediction in different subchannels: Case 4 (first row); Case 5 (second row).

To further illustrate the influence of buoyancy correction on wall temperature predictions, Figure 4.22 presents the variation of wall temperature in the corner subchannel alongside the buoyancy parameter along the axial direction. The comparison can show the impact of different buoyancy correction approaches, particularly the difference in the predicted location of heat transfer deterioration. As discussed in previous sections, the deviation among the correlations leads to differences in the location of HTD.

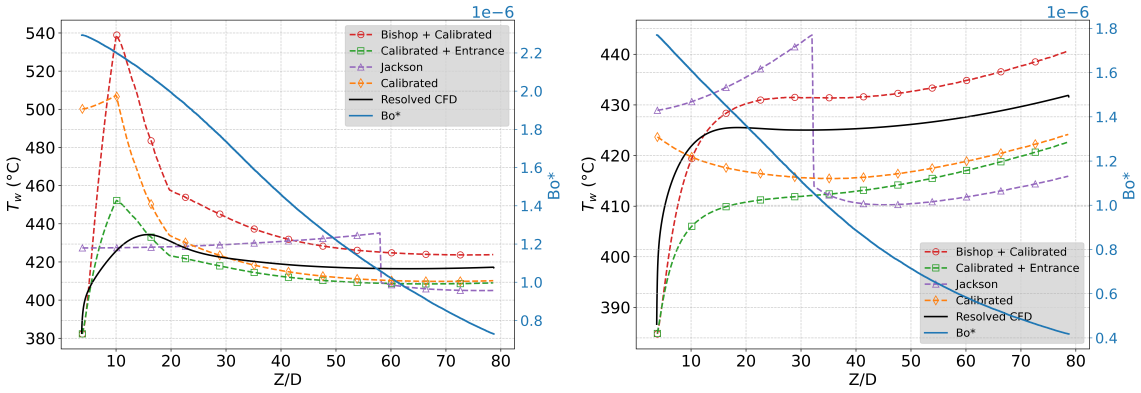

(a) Case 4.

(b) Case 5.

Figure 4.22: Wall temperature and buoyancy parameter (Bo^*) variation along the axial direction in corner subchannel.

Next, the temperature redistribution across different subchannels in Case 4 is analysed at various axial positions to assess the impact of buoyancy effects and compare the performance of SubChCFD on parameter redistribution with conventional CFD. Figure 4.23 presents the temperature variation along two distinct lines: one across the edge and center subchannels (left) and the other in the corner subchannel (right).

Notably, in the corner subchannel (Figure 4.23b), heat transfer deterioration occurs at the onset due to the strong buoyancy effect. This results in a non-uniform temperature development in the streamwise direction, with a higher temperature gradient and a pronounced rise near the pin wall at the initial stage. This effect is primarily due to local heat transfer deterioration and entrance effects. SubChCFD captures these features reasonably well, showing good agreement with resolved CFD predictions despite its coarse mesh nature.

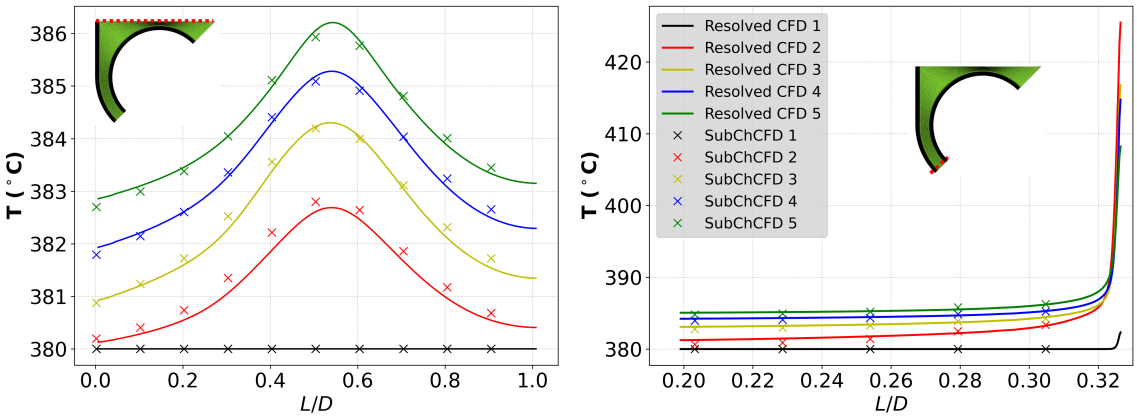

(a) Temperature distribution along the line spanning the edge and center subchannels.

(b) Temperature distribution along the line in the corner subchannel.

Figure 4.23: Radial temperature distribution across different subchannels in Case 4. 1, 2, 3, 4 and 5 represent the cross sections axial location at 0.03m, 0.18m, 0.33m, 0.48m and 0.63m

The velocity distribution along different subchannels is also analysed. Figure 4.24 presents the velocity profiles along the same lines discussed above.

It is useful to discuss the interesting velocity distribution using the resolved CFD results. For the line across the edge and center subchannels, in the upstream, the velocity profile follows a typical trend, exhibiting a local velocity dip at the midpoint due to the narrow gap between the pins and the influence of wall shear, which slows the flow in this region (Figure 4.24a). This is observed from early section. However, later, the velocity profile is flipped and the velocity peaks at the narrow (mid-point) through a strong acceleration in the narrow region. This is due to the combined effects of buoyancy-induced acceleration and stronger flow expansion in this region. This highlights the significant role of buoyancy in shaping flow distribution and velocity profile distortions. It is interesting to note that the SubChCFD has captured the general trends very well, with the initial low velocity at the narrow, its acceleration along the flow and finally peaks towards the downstream end.

In the corner subchannel (Figure 4.24b), the velocity is accelerated near the fuel pin due to heating whereas the acceleration on the casing wall is less, forming an asymmetric profile. SubChCFD effectively captures this buoyancy-induced flow behaviour, showing a good agreement with resolved CFD predictions. The error bars, set at 10%, illustrate that even with a coarse grid approach, SubChCFD provides velocity predictions within an acceptable range.

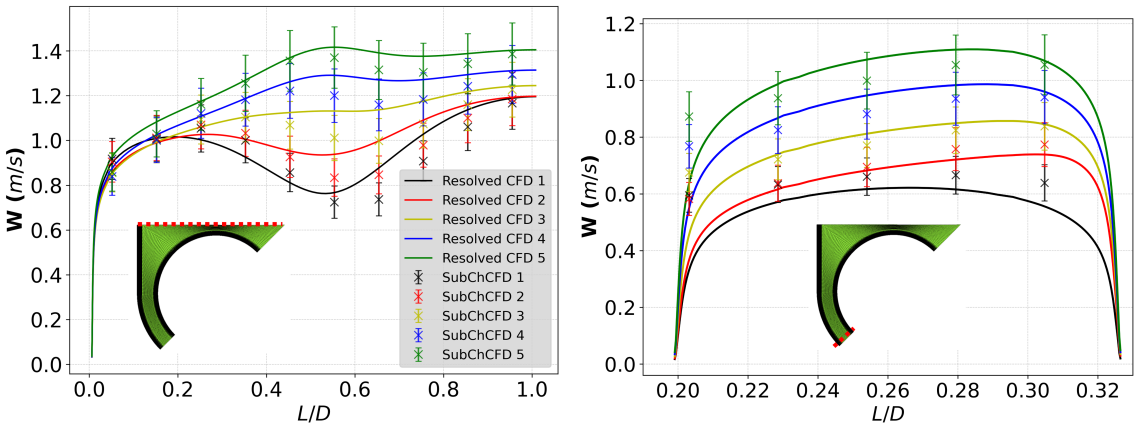

(a) Velocity distribution along the edge and center subchannels.

(b) Velocity distribution along the corner subchannel.

Figure 4.24: Velocity profiles along different subchannels in Case 4.

Overall, the above highlights the redistribution of temperature and velocity across different subchannels due to the effect of buoyancy and flow expansion observed in the resolved CFD. The comparison demonstrates that SubChCFD provides a reasonable approximation of the resolved CFD results by both capturing the physical phenomena quantitatively and providing reasonably good quantitative predictions. This agreement is particularly notable in regions dominated by buoyancy effects, where SubChCFD successfully captures key trends such as heat transfer deterioration and buoyancy-induced flow behaviour.

4.4.3 Group C - Friction factor correlation validation

In addition to the development of heat transfer correlations, friction factor correlations were also considered during the development of SubChCFD for supercritical flow conditions. These correlations are related to the prediction of pressure drop and velocity distribution. The original friction factor correlation, which has already been included in SubChCFD, is based on isothermal flow conditions without any correction for variable properties.

To account for the effects of thermal physical property variation, two additional correlations from the literature were implemented into SubChCFD. The first is Kirillov's correlation [69], which introduces a correction based on the wall-to-bulk density ratio. The second is the correlation proposed by Yamashita et al. [138], which applies a correction using the wall-to-bulk viscosity ratio. Both correlations serve as modifications to the original isothermal formulation.

Resolved CFD results are used as reference data to evaluate the prediction. The comparison is conducted using Case 6 and Case 7. Figure 4.25 shows the buoyancy parameter in different subchannel for Case 6 and Case 7. Case 7 has stronger buoyancy effect, especially in the corner subchannel.

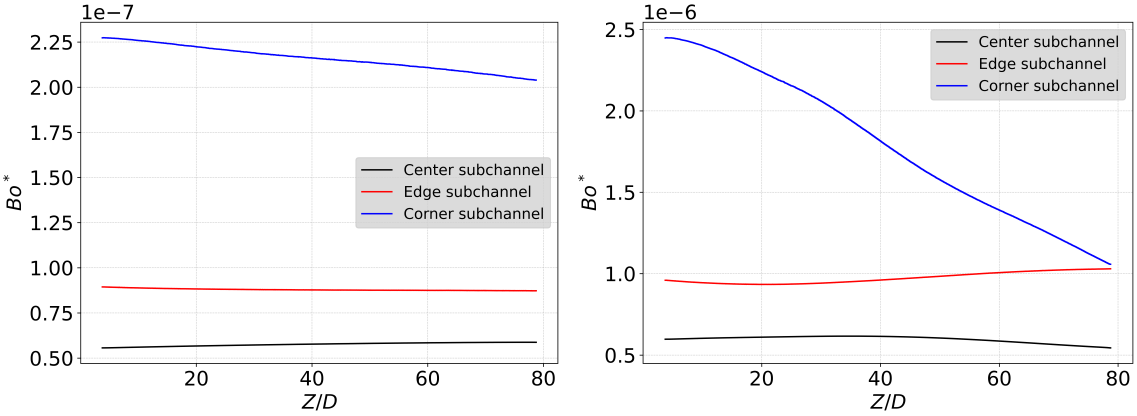

(a) Case 6. (b) Case 7.

Figure 4.25: Buoyancy parameter for Case 6 and case 7.

As shown in Figure 4.26, the predictions in SubChCFD using different correlations are generally consistent with the resolved CFD results. The modified correlations lead to slightly lower pressure drop predictions compared to the original formulation, reflecting the influence of thermal physical property gradients in the flow.

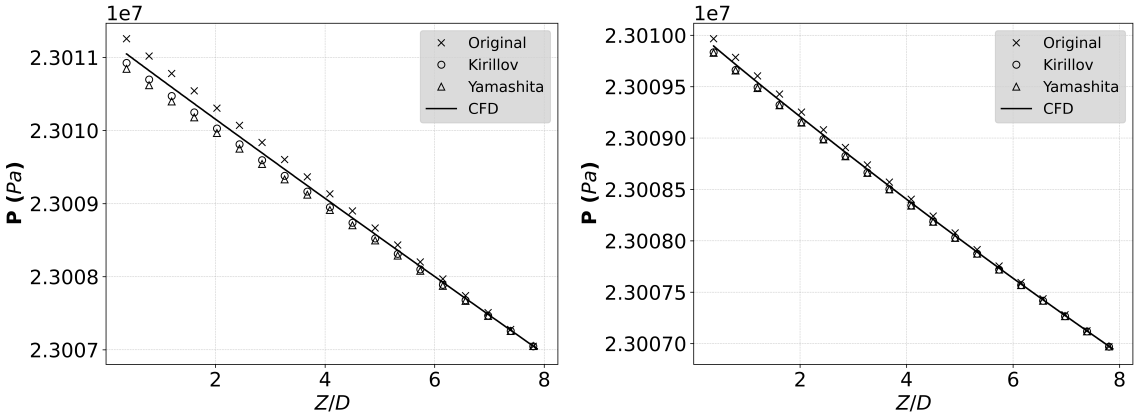

(a) Case 6. (b) Case 7.

Figure 4.26: Comparison of pressure drop for Case 6 and case 7.

Figure 4.27 presents the velocity distribution across the edge and center subchannels at different axial locations, as discussed in the previous section. The data

points with different markers represent the predictions obtained using the original, Kirillov, and Yamashita friction factor correlations. For Case 6, all correlation results are closely aligned, showing minimal variation. In Case 7, slight deviations appear among the different predictions, but the differences remain small overall. indicating limited sensitivity of the velocity field to the choice of friction factor correlation under these conditions.

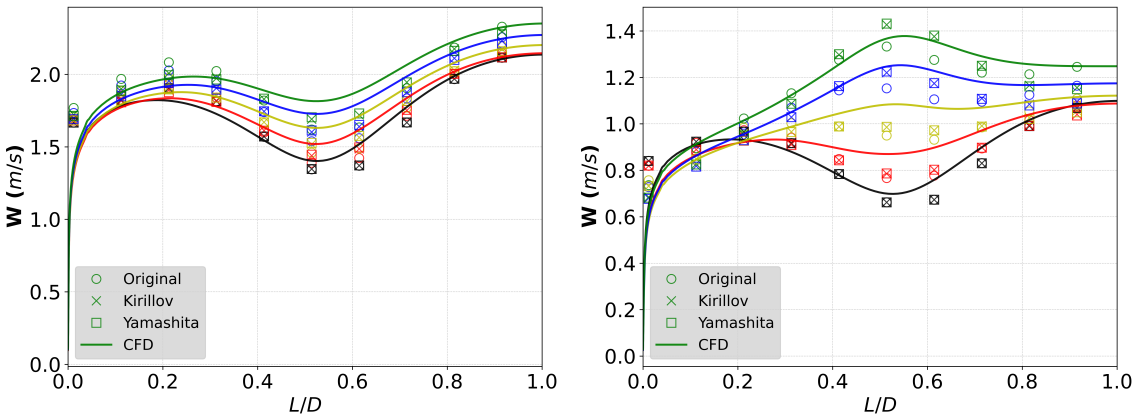

(a) Case 6. (b) Case 7.

Figure 4.27: Comparison of velocity profile for Case 6 and case 7.

In summary, all the correlations show good agreement with the resolved CFD data, and the differences between the predictions are relatively small. This indicates that, under these tested conditions, the pressure drop and velocity redistribution are not highly sensitive to the choice of friction factor correlation. However, further investigation is needed to evaluate the performance of different friction factor correlations under a wider range of flow and thermal conditions.

4.4.4 Group D - Comparison with experimental data

To further demonstrate the accuracy and applicability of the SubChCFD model, its predictions are compared against experimental data from existing studies [126]. The flow conditions are summarized in Case 8 and Case 9, where different inlet temperatures are used to extend the range of bulk enthalpy for a more comprehensive validation. This comparison focuses on key parameters such as wall temperature and its variation with bulk enthalpy, highlighting the predictive performance of different empirical correlations.

Figure 4.28 presents the wall temperature predicted by SubChCFD using different empirical correlations for the fully developed flow region, compared against the measured wall temperature from the experiment.

In Case 8, where buoyancy effects are relatively weak, the K & P and Jackson correlations provide the best agreement with experimental wall temperature data. The Bishop correlation slightly underpredicts, while the Calibrated correlation consistently overpredicts the wall temperature. The overprediction by the calibrated model can be attributed to its stronger buoyancy correction, which is less applicable in subchannels with weaker buoyancy effects.

In Case 9, where buoyancy effects are stronger, all models exhibit deviations from the experimental data. The experimental results indicate an increased rate of wall temperature rise with bulk enthalpy. This trend further confirms the influence of buoyancy, as the heat transfer deterioration occurs, resulting in a steeper temperature rise. This trend is consistent with previous CFD investigations. The calibrated correlation consistently overpredicts wall temperature. This suggests that while the model captures the overall influence of buoyancy, its correction may overcompensate, leading to unexpected higher temperature predictions. Conversely, the K & P, Jackson, and Bishop correlations, which generally align well with experimental data in weaker buoyancy conditions, exhibit noticeable deviations in this case. It seems that their performance declines as the effects of buoyancy become stronger, highlighting the potential limitations in their capacity to account for the effects of stronger buoyancy in the flow.

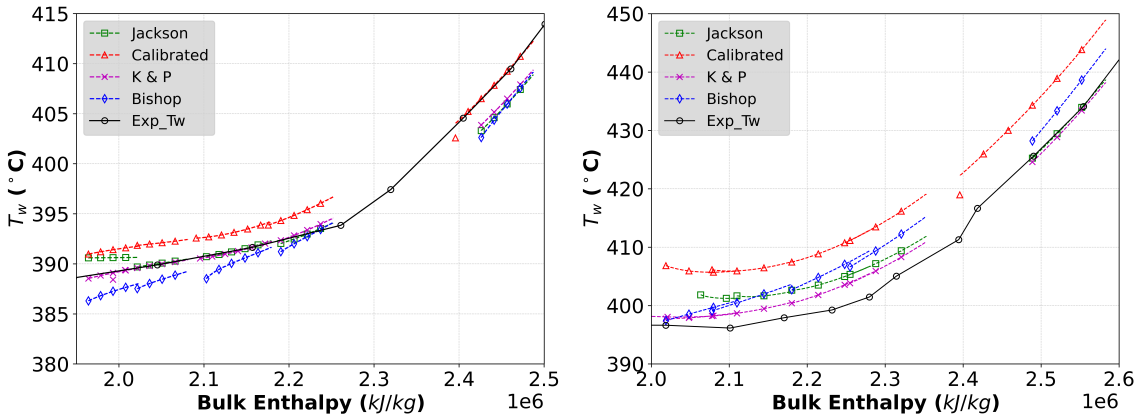

(a) Case 8. (b) Case 9.

Figure 4.28: Comparison of average wall temperature predictions with experimental data.

It also indicates that the SubChCFD predictions remain within 2.5% of the experimental values, which is reasonable considering the coarse mesh nature. However, another key factor that contributes to the observed deviations is the differences in averaging methods between the experimental and numerical approaches. In experiments, temperature probes are positioned at multiple locations around the rod, while in SubChCFD, bulk properties are averaged spatially within each subchannel. This variation in data processing may lead to discrepancies as well.

This heat transfer coefficient comparison is shown in Figure 4.29. All results from SubChCFD can effectively capture the heat transfer enhancement due to the c_p peak around the pseudo-critical temperature, which validates that the Nusselt number correlation accounts for variable physical property performance well in SubChCFD.

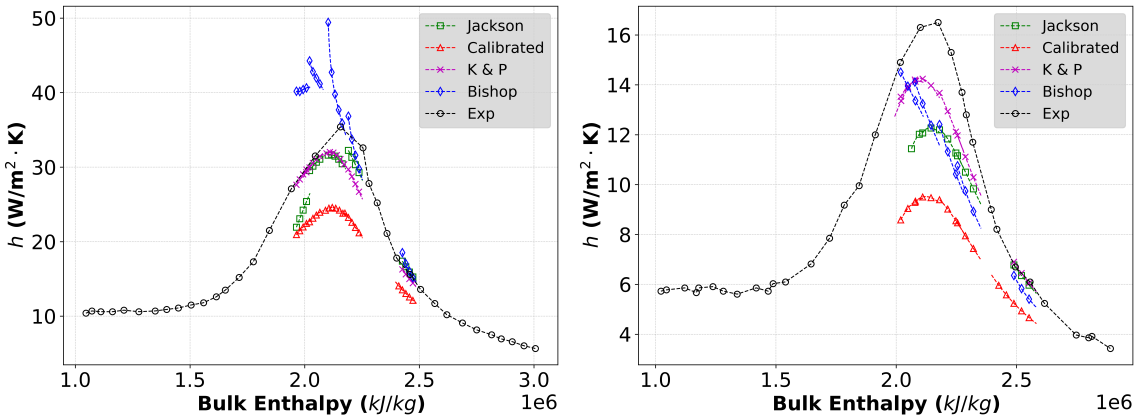

(a) Case 8. (b) Case 9.

Figure 4.29: Comparison of average heat transfer coefficient predictions with experimental data.

Overall, the findings demonstrate that SubChCFD provides a reasonable prediction of heat transfer performance across the entire channel, with agreement observed when compared to experimental data. However, further refinements are necessary to enhance its accuracy, particularly in capturing variations within different subchannels under both strong and weak buoyancy conditions, as well as their interactions.

4.5 Conclusion

This chapter discusses the development, validation, and application of the SubChCFD model for supercritical fluid flow in rod bundle configurations. In addition to implementing correlations that account for variable thermal physical properties and buoyancy corrections, two new combination models: Bishop + Calibrated and Calibrated

+ Entrance, were introduced to enhance prediction, particularly in developing stage. Besides, correlations for modifying the friction factor are implemented as well.

Comparisons with resolved CFD confirmed that SubChCFD can capture key flow physics such as velocity redistribution, heat transfer deterioration, and pressure drop trends using a coarse mesh. The new combination correlations showed significant improvement in predicting wall temperature profiles, especially in corner subchannels, where buoyancy effects are strongest. The Calibrated + Entrance model effectively moderated temperature peaks near the entrance, indicating improved modelling of developing flow. Besides, friction factor correlations were evaluated to examine their influence on pressure drop and velocity distribution. Comparisons between the original isothermal formulation and modified correlations by Kirillov and Yamashita showed good agreement with CFD results. The differences among predictions were small, indicating limited sensitivity to the choice of friction factor correlation under the tested conditions.

Demonstration against experimental data confirmed that SubChCFD achieves reasonable accuracy, with deviations in wall temperature predictions remaining within 2.5%. The analysis also indicated limitations, including the impact of averaging methods, the neglect of wall conduction effects, and the sensitivity of some correlations to strong buoyancy conditions. These findings suggest potential improvements, such as refining the buoyancy correction approach for different flow conditions.

Overall, this study demonstrates the feasibility of using SubChCFD for simulating heat transfer and flow behaviour under supercritical conditions by implementing appropriate correlations, offering a flexible and computationally efficient alternative to fully resolved CFD.

Chapter 5

Development for the wire-wrapped rod bundles

5.1 Introduction

To improve its applicability for complex geometries, this study focuses on extending SubChCFD to model wire-wrapped rod bundle configurations. Wire spacers play an essential role in nuclear fuel assemblies by promoting mixing and enhancing heat transfer, but they also introduce complex flow structures, including swirling flow effects. These flow features cannot be resolved using a coarse mesh, which presents a challenge for SubChCFD development.

To address this challenge, this study adopts a momentum source term approach inspired by Hu et al. [53]. This method uses pseudo-body forces to represent the effect of wire spacers without explicitly resolving their geometry. Volume porosity is used to identify the mesh regions occupied by the wires, and within these regions, momentum source terms are applied to capture the influence of wires on the flow. A local coordinate system aligned with the wire geometry is introduced to formulate these forces, following the approach proposed by Hu et al [53].

This chapter presents the methodology for the development of SubChCFD, along with its validation and demonstration in different wire-wrapped rod bundle configurations, such as a locally wire-wrapped 2×2 rod bundle, a fully wire-wrapped 2×2 rod bundle, and an extended 7-pin bundle in a hexagonal channel. The results are compared with high-resolution CFD simulations and experimental data to validate and demonstrate the capability of SubChCFD for capturing the key flow and heat transfer behaviours induced by wire-wrapped spacers.

5.2 Methodolegy

5.2.1 Pseudo-body force source terms

This development builds upon the foundational work of Hu et al. [53], integrating key methodological components to further develop SubChCFD. In Hu's approach, pseudo-body forces normal to the wire, tangential to the pin, and parallel to the wire are introduced to model the effects of wire spacers on flow behaviour. In SubChCFD, these forces are implemented as body forces in the momentum equations, ensuring the effective replication of wire-induced flow effects.

To apply these forces, a local coordinate system is introduced, as illustrated in Figure 5.1. The unit vector $\mathbf{e}_1$ is normal to the wire and points to the center of the pin. The unit vector $\mathbf{e}_2$ is parallel to the helical wire, representing the direction that follows the wire geometry. The third unit vector $\mathbf{e}_3$ is tangential to the pin but normal to the wire, playing a role in reproducing the secondary flow effects induced by the wire spacer.

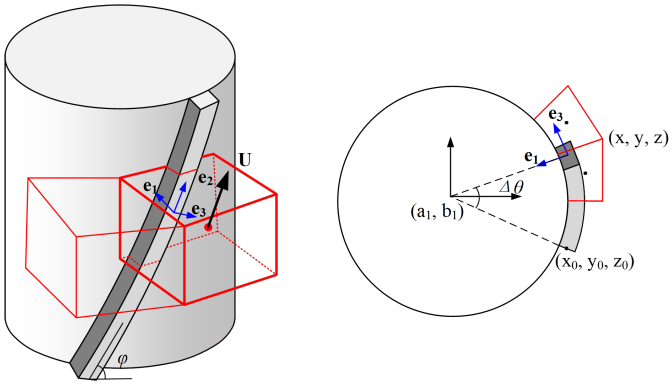

Figure 5.1: Local coordinate system for the momentum source terms.

The angle φ is the helical pitch angle of the wire, which describes the inclination of the wire relative to the rod's axial direction. The angle θ defines the angular position of a computing cell around the rod's cross-section. It is measured from the reference position where the wire first contacts the rod surface. Using these two angles, the local coordinate system is constructed to follow the wire geometry. The body forces are formulated in this local coordinate system and then projected onto the global coordinate system for implementation in the solver.

The total force per unit volume applied within the SubChCFD is expressed as:

$$\vec{f} = f_1\vec{e}_1 + f_2\vec{e}_2 + f_3\vec{e}_3 \tag{5.1}$$

where f_1, f_2, and f_3 are the force components acting along the respective unit vectors $\mathbf{e}_1, \mathbf{e}_2$, and $\mathbf{e}_3$. These components are further defined by the following expressions:

$$\vec{f_1} = \frac{C\rho v_1(v_3 + v_2\cos\Phi + v_1)}{dw}(-\vec{e_1}) \tag{4}$$

$$\vec{f_2} = \frac{f_{fr}\rho v_2^2}{2dw}(-\vec{e_2}) \tag{5}$$

$$\vec{f_3} = \frac{C\rho v_3(v_3 + v_2\cos\Phi + v_1)}{dw}(-\vec{e_3}) \tag{6}$$

In these equations, v_1 is the velocity component normal to both the wire and the pin, defined as $v_1 = |\vec{v} \cdot \vec{e_1}|$. The term v_2 represents the velocity component along the wire direction, expressed as $v_2 = |\vec{v} \cdot \vec{e_2}|$. The force component $\vec{f_1}$ acts in the normal direction, blocking radial flow into the wire region. The force $\vec{f_2}$ is aligned with the helical wire direction and accounts for the additional frictional resistance introduced by the presence of the wire. The friction factor f_{fr} is modelled using the Blasius–McAdams correlation [116]. The force $\vec{f_3}$ influences both the crossflow and axial flow, contributing to swirl generation and flow redistribution.

The coefficient C is a tunable parameter used to control the strength of body forces applied in the directions normal to the wire. In the momentum source model developed by Hu et al. [53], C was introduced to ensure sufficient resistance to block the flow across the wire, effectively accounting for the wire width. In SubChCFD, the wire region is instead defined using volume porosity, but C still serves the same primary purpose. It acts as a drag-related coefficient that determines the magnitude of resistance, ensuring that the applied forces appropriately replicate the blocking effect of the wire without resolving its geometry. Additionally, C contributes to the numerical stability of the simulation by preventing excessive local velocity gradients, thereby acting as a stabilization factor to avoid divergence during iteration.

5.2.2 Mesh and modelling strategy

Accurately identifying the wire region is essential for the application of the momentum source terms in SubChCFD. Wire spacers introduce additional resistance and swirling effects in the coolant flow, which should be reproduced in simulations. To achieve this, it is necessary to identify the computational cells occupied by the wire precisely to ensure that the momentum source terms are correctly applied to account for the

wire effects. This section details the mesh and modelling strategies used to implement these source terms in SubChCFD.

A conventional method for modelling wire spacers is to explicitly resolve the wire geometry using a fine computational mesh. However, when a structured mesh is used, this method may lead to highly skewed cells due to the helical shape of the wire and may require an extremely fine mesh to maintain numerical stability. Such a fine mesh significantly increases computational cost, making it impractical for large-scale simulations. To overcome these challenges, SubChCFD employs a porosity-based approach, which represents the wire as a distributed resistance within the computational domain without explicitly capturing its geometric details.

In SubChCFD, a separate mesh is generated for the wire geometry during the preprocessing stage, as illustrated in Figure 5.2. This wire mesh is used to compute the volume porosity.

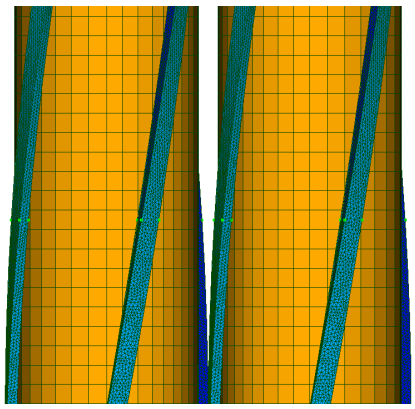

Figure 5.2: Wire mesh for porosity calculation.

The volume porosity is defined as the fraction of the computational cell volume available for fluid flow. Cells that are entirely fluid-filled have a porosity value of 1, whereas cells partially occupied by the wire have a porosity value less than 1. The porosity is used to scale the momentum source terms applied within each cell, ensuring that the forces are only applied in regions partially or fully occupied by the wire. This allows the wire's influence to be accurately incorporated into the simulation. Figure 5.3 illustrates the computed porosity distribution.

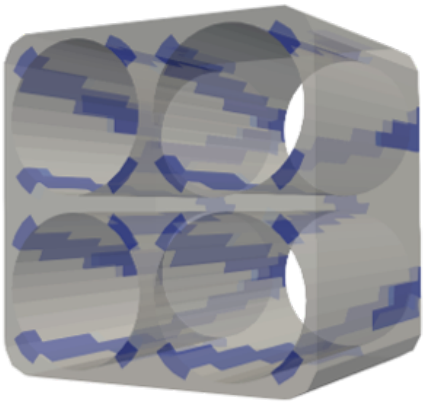

Figure 5.3: Porosity distribution in the computational domain.

The blue regions indicate cells where the porosity is less than one, meaning they are partially or fully occupied by the wire. By incorporating porosity-based wire modelling, the momentum sources are only applied in cells with porosity values less than one, and their magnitudes are weighted according to the porosity. Specifically, the source term in each cell is scaled as

$$\vec{S} = \vec{f} \cdot (1 - \phi) \tag{5.2}$$

where $\vec{f}$ is the original force vector and ϕ is the local porosity. This ensures that the forces introduced by the wire spacers are properly scaled based on their interaction with the coolant flow.

5.3 Cases studied

5.3.1 Physical model

This study considers three test cases, two of which are from the ECC-SMART project [38]. The first case examines a locally wire-wrapped 2×2 rod bundle, where wire spacers are present only in specific sections along the rods. The second case also features a 2×2 rod bundle, but with a single fully wrapped wire around each pin over the entire test section. The third case is based on an experimental study conducted at Hubei Technology University in China [125] investigating cross flow in a 7-pin bundle with fully wire-wrapped spacers in a hexagonal channel.

This section provides a detailed description of the experimental configurations and the flow conditions used in these test cases. In this chapter, the new combination correlations from Chapter 4 are not used. It applies a baseline model, Jackson's

correlation with variable properties and the buoyancy correction to all cases. The purpose of this chapter is to research the effects of wire spacers (flow swirl and mixing), not to deliver best-estimate wall-heat-transfer predictions. Applying one robust and widely validated correlation in all cases eliminates differences between models and enables a consistent comparison.

The first test case is a locally wire-wrapped 2×2 rod bundle, where wire spacers are placed periodically along the rod axis as shown in Figure 5.4, in which the geometric details of the setup are illustrated. The total length of the rod bundle is 2500 mm, with six wire spacer sections distributed along the axial direction. Each wire region is 25 mm long, with four helical wires wrapped around each fuel pin.

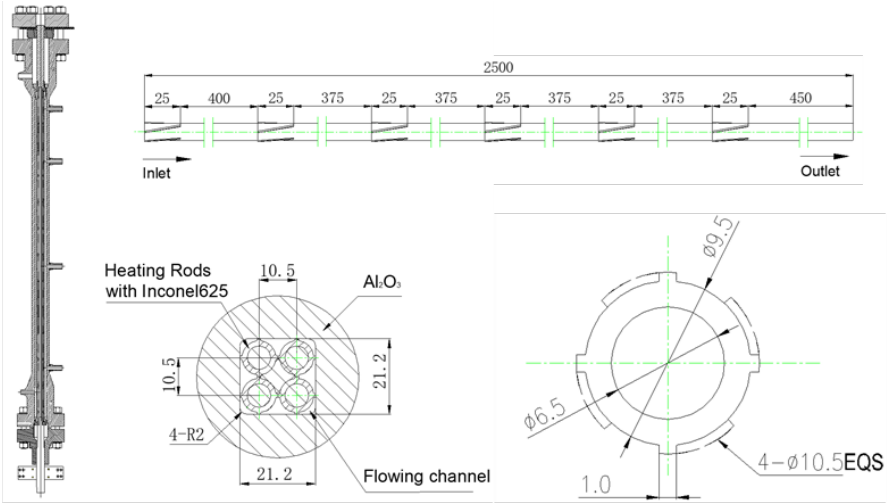

Figure 5.4: Geometric configuration of the locally wire-wrapped 2×2 rod bundle [38].

The experimental conditions used in this test case are outlined in Table 5.1. The coolant operates under supercritical conditions, with a system pressure of 25.0 MPa and an inlet temperature of 353.0°C. The mass flux through the bundle is set at 1025.0 kg/m^2·s, while a uniform heat flux of 504.0 kW/m^2 is applied to the rods.

Table 5.1: Operating conditions for the locally wire-wrapped 2×2 rod bundle.

Case	$\boldsymbol{P}$ (MPa)	$\boldsymbol{G}$ (kg/m^{2}s)	$\boldsymbol{q''}$ (kW/m^2)	$\boldsymbol{T_{in}}$ (°C)
Case 1	25.0	1025.0	504.0	353

In addition to the main cases, a demonstration case was conducted at the initial step as a test case. This test case compares SubChCFD with a fully resolved CFD simulation in a shorter computational domain, aiming to demonstrate the implementation of the momentum source term method.

The physical model used in this test case corresponds to a segment of the locally wire-wrapped rod bundle, but only a portion of the wire-wrapped region is considered, which is 25mm, as shown in Figure 5.4. Unlike the longer domain case, the short domain case is specifically designed to demonstrate the momentum source term method. To simplify the computational setup, the flow conditions are defined at atmospheric pressure rather than under supercritical conditions. No heat input is applied, and the fluid properties are assumed to be constant. The operating conditions are summarised in Table 5.2. And the k-ω SST turbulence model is employed in resolved CFD.

Table 5.2: Operating conditions for the short domain case.

Case	$\boldsymbol{P}$ (Pa)	ρ (kg/m^3)	μ (Pa·s)	**Inlet velocity** (m/s)
Case_short	101325.0	997.13	0.00089	1.5

The second test case involves a fully wire-wrapped 2×2 rod bundle, where each fuel rod is wrapped with a single continuous wire, as illustrated in Figure 5.5. The duct has a width of 23.03 mm and extends 600 mm along the flow direction. Each rod has an outer diameter of 8 mm with a wall thickness of 1.5 mm. The rod pitch is 9.44 mm, and the minimum gap between the rods and the duct's inner wall is 1.44 mm.

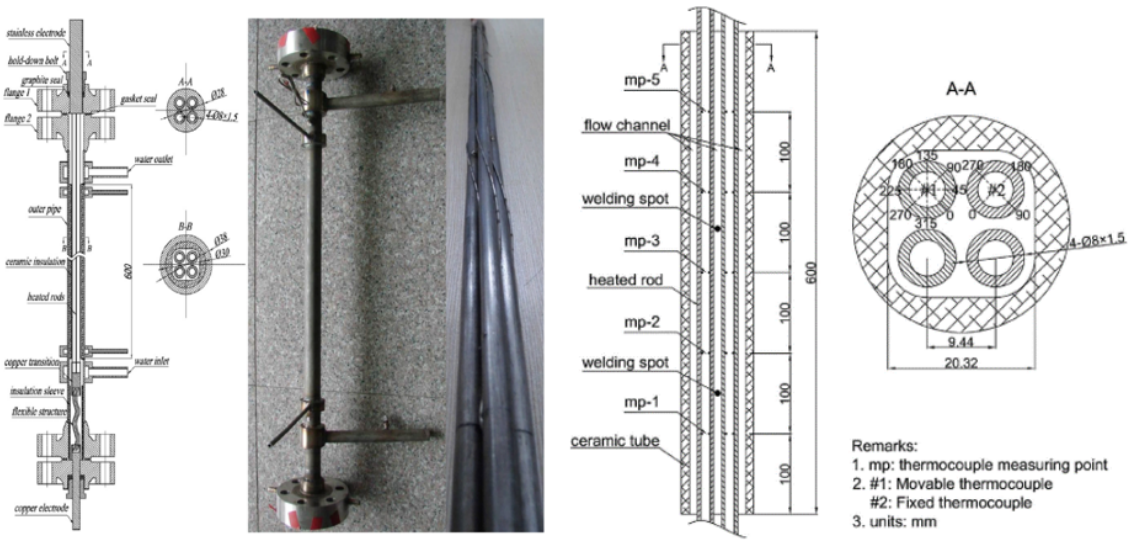

Figure 5.5: Geometric configuration of the fully wire-wrapped 2×2 rod bundle [38].

The flow conditions for both experimental setups, including pressure, mass flow rate, heating power, and inlet temperature, are summarized in Table 5.3. The test

operates under supercritical conditions as well.

Table 5.3: Operating conditions for the fully wire-wrapped 2×2 rod bundle.

Case	$\boldsymbol{P}$ (MPa)	$\boldsymbol{G}$ (kg/m^{2}s)	$\boldsymbol{q''}$ (kW/m^2)	$\boldsymbol{T_{in}}$ (°C)
Case 2	25.26	259.91	12.09	369.19
Case 3	25.03	282.33	12.10	390.75

To further demonstrate the SubChCFD implementation for the predictive of cross flow and across different reactor geometries, a 7-pin wire-wrapped bundle within a hexagonal channel [125] was simulated. The experimental rig is illustrated in Figure 5.6.

The test section for the simulation consists of seven acrylic rods inserted into a hexagonal acrylic chamber. Each rod has an outer diameter of 30 mm, a wall thickness of 0.5 mm, and a total length of 1500 mm. Helical wires are wrapped around each rod to induce swirl and enhance mixing. The wire diameter is 5 mm, with a wall thickness of 0.3 mm and an axial pitch of 500 mm. The wire pitch-to-diameter ratio is 100, and each rod surface is wrapped with three complete wire pitches.

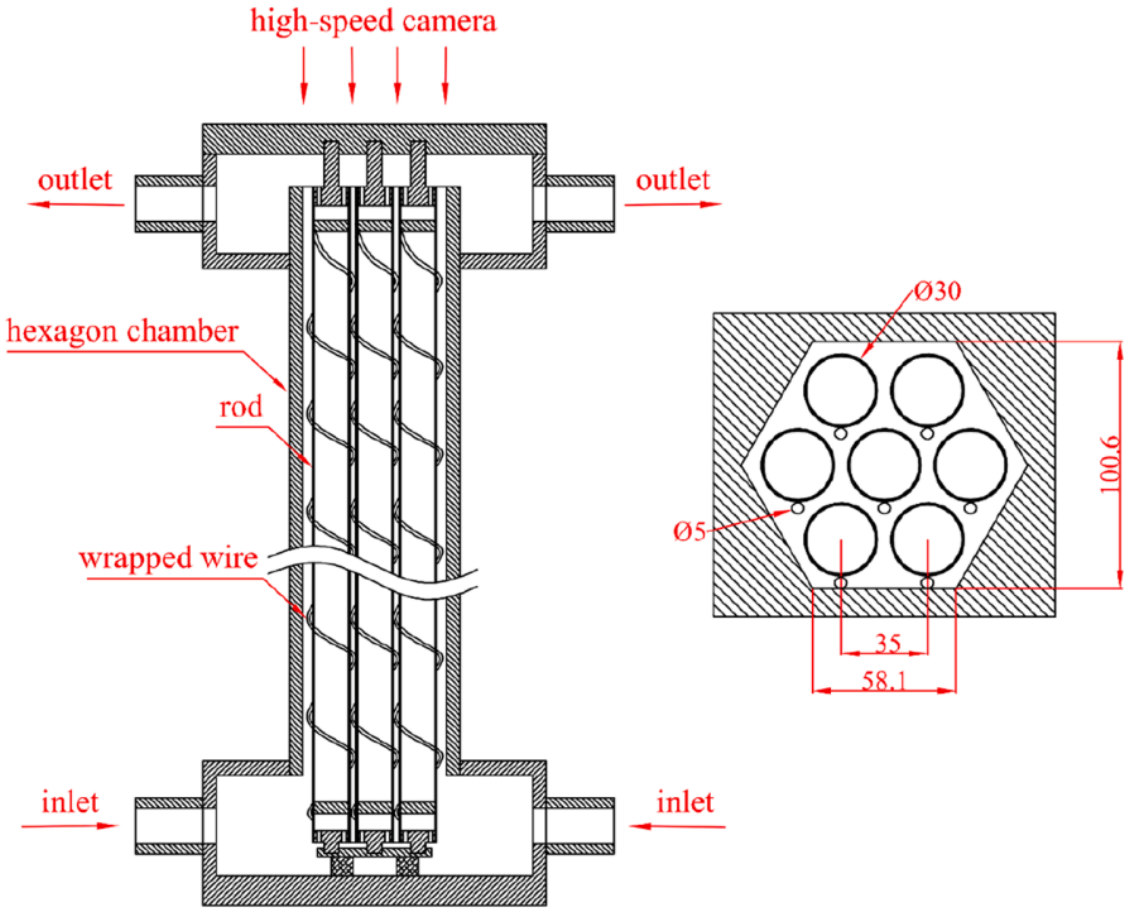

Figure 5.6: Geometric configuration of the 7-pin wire-wrapped bundle within a hexagonal channel [125].

The experimental conditions for this test case, including Reynolds number, volumetric flow rate, nominal velocity and inlet temperature are summarized in Table 5.4. All the cases are conducted under subcritical flow conditions using water as the working fluid.

Table 5.4: Flow conditions for the 7-pin wire-wrapped bundle experiment.

Case	$\boldsymbol{Re}$	$\boldsymbol{Q}$ (m^3/h)	$\boldsymbol{w}$ (m/s)	$\boldsymbol{T_{in}}$ (°C)
Case 4	3000	2.69	0.2	25.0
Case 5	6000	5.38	0.4	25.0
Case 6	9000	8.07	0.6	25.0

5.3.2 Mesh strategy

For all test cases, the SubChCFD simulations follow a consistent meshing strategy. The computational mesh is generated using a two-step process, where a 2D cross-sectional mesh is first created, which is then extruded along the axial direction to a specified length, referencing the corresponding experimental configuration. The computational domain for each case follows the same methodology introduced in the previous chapter (2x2 rod bundle without wire-wrapped spacers). Additionally, the meshing strategy for wire spacers is implemented using the porosity-based method described in the methodology section. These approaches can effectively capture the influence of wire-induced swirl while maintaining computational efficiency.

For the short domain case, the SubChCFD mesh follows the same meshing strategy as described previously. In contrast, the resolved CFD simulation explicitly resolves the wire geometry, requiring a more refined mesh and an advanced turbulence model. A polyhedral mesh is generated for the domain, incorporating prism layers near the walls to improve boundary layer resolution to ensure the y^+ is around one, particularly near the wire surface. And a mesh sensitivity test has been done. This setup provides sufficient accuracy for capturing the relevant flow physics. The cross-sectional view of the CFD mesh, highlighting the explicitly resolved wire geometry, is shown in Figure 5.7.

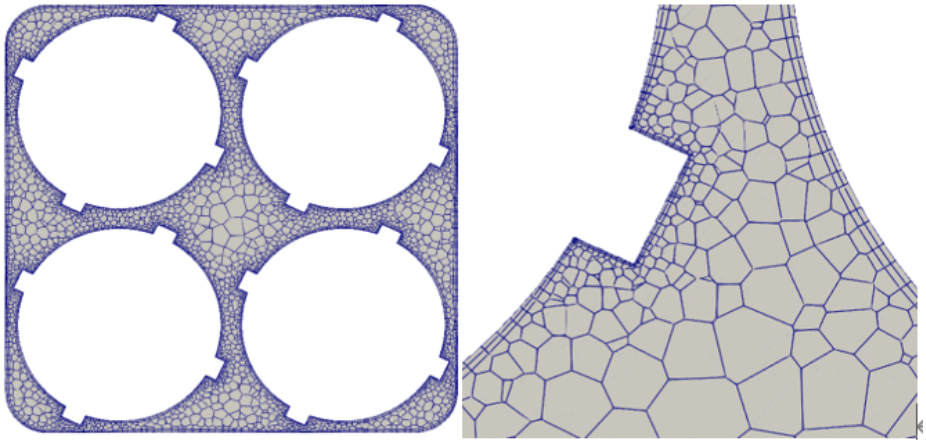

Figure 5.7: Cross-sectional view of the resolved CFD mesh.

5.4 Results and discussion

5.4.1 The short domain case

Before discussing the main cases, the test case described earlier was used to verify the implementation of the momentum source term method. A key aspect of this verification involves ensuring that the local coordinate system $(\mathbf{e}_1, \mathbf{e}_2, \mathbf{e}_3)$ is correctly defined based on the wire spacers.

Figure 5.8 illustrates the extracted local coordinate vectors $\mathbf{e}_1$, $\mathbf{e}_2$, and $\mathbf{e}_3$ from the test case. These vectors are computed for the mesh cells occupied by the wire, ensuring that the momentum source terms are correctly aligned with the wire-induced forces.

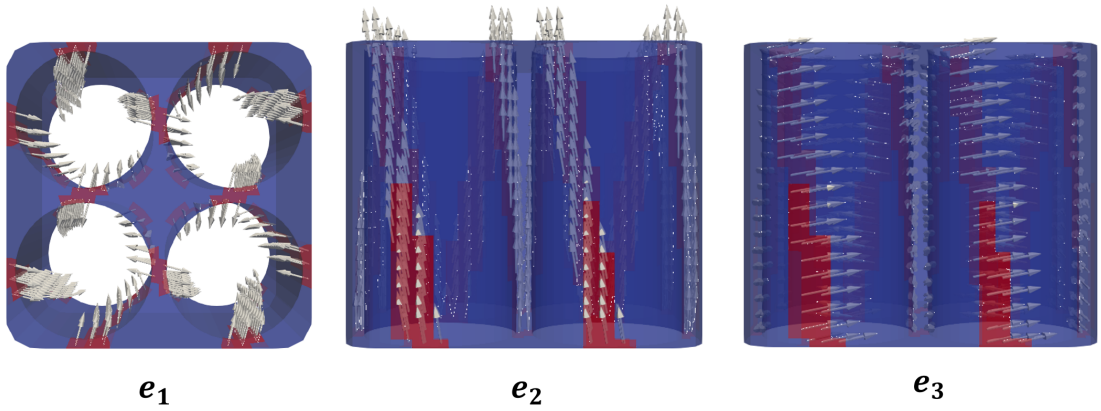

Figure 5.8: Visualization of the local coordinate system $(\mathbf{e}_1, \mathbf{e}_2, \mathbf{e}_3)$.

The results confirm that the cells occupied by the wires are accurately defined around the rods. Furthermore, the local coordinate system is correctly oriented relative to the wire, verifying that the forces can be applied in the appropriate direction to reasonably replicate the physical influence of the wire spacers on the flow behaviour.

To validate whether the implementation in SubChCFD can reproduce the wire spacer effects, the cross flow predicted by SubChCFD are compared with fully resolved CFD data. Figure 5.9 presents velocity vector plots in a cross-sectional view. The left image shows the results from the resolved CFD simulation, while the right image corresponds to the SubChCFD prediction.

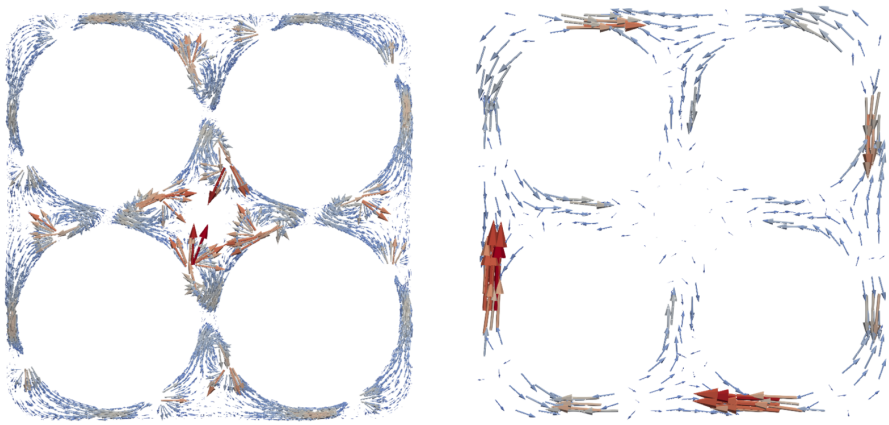

Figure 5.9: Comparison of velocity vector plots in a cross-sectional view: CFD results (left), SubChCFD results (right).

These vector plots illustrate the directional flow patterns and provide a clear depiction of the swirl effects induced by the wire spacers in the channel. Both SubChCFD and CFD predict similar overall swirling motion around the rods. This indicates that the momentum source term approach in SubChCFD is capable of reproducing the primary flow behaviour introduced by the wire spacers.

In this test case, no direct quantitative comparison is provided because the simulation was specifically designed as a simplified setup to verify the correct implementation of the momentum source term method, particularly the alignment of the local coordinate system and the application of pseudo-body forces. The objective here is to demonstrate the capability of SubChCFD to replicate the expected swirl features qualitatively. Quantitative validation exercises are presented later using more realistic and complex cases.

5.4.2 Locally wire-wrapped case

Figure 5.10 presents the comparison of the average bulk velocity along the streamwise direction between SubChCFD of the locally wire-wrapped cases and results from other research groups of the ECC-SMART project [38] using fully resolved CFD simulations with different turbulence models. In SubChCFD, the average bulk velocity is calculated based on all computing cells across the entire cross section.

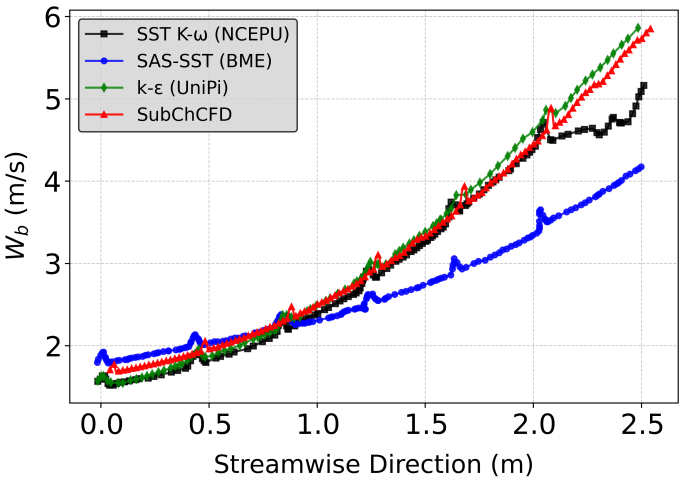

Figure 5.10: Comparison of the average bulk velocity along the streamwise direction. North China Electric Power University(NCEPU), Budapest University of Technology and Economics (BME), University of Pisa (UniPi)

The results show that SubChCFD agree well with CFD simulations of NCEPU (SST) and UniPi (k-ϵ) in terms of overall trend and magnitude of the bulk velocity in the axial direction. Despite using a coarser mesh, the method captures the key flow characteristics in the wire-wrapped region, including the peaks in the velocity profile correspond to the wire-wrapped sections, due to localized acceleration of the flow. This acceleration occurs because the wire spacers reduce the available flow area, causing an increase in velocity. After passing through the wire-wrapped region, the flow gradually recovers.

The comparison between the pressure drops predicted using SubChCFD and TEMPA-SC, a subchannel code, is shown in Figure 5.11. The results demonstrate that the pressure drop predictions from both codes are in close agreement. The different absolute pressure values are due to the use of different reference pressure, which is insignificant.

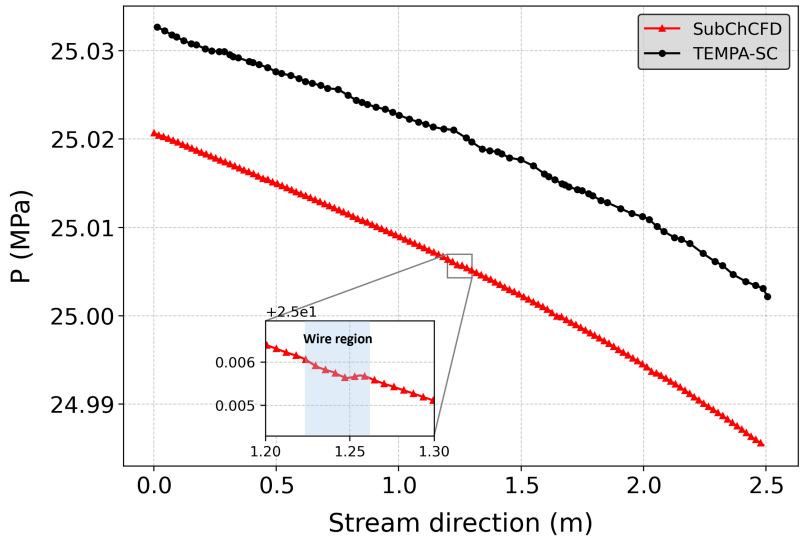

Figure 5.11: Comparison of pressure drop predictions between SubChCFD and TEMPA-SC.

The inset in the figure highlights the effect of the wire spacers. It can be seen that the pressure gradient in the spacer region is greater than in other regions due to the additional pressure drop caused by the spacer, and immediately after the spacer, there is a sudden recovery of the pressure as expected. It is therefore clear that the implementation of the momentum source terms allows SubChCFD to correctly account for the localized pressure variations caused by the wire-wrapped structures.

Figure 5.12 presents the wall temperature distribution along the streamwise direction at a fixed azimuthal angle on the rod, for different type of subchannels: center, edge, and corner. The SubChCFD predictions follow the general trend observed in the other models, whereas there are significant differences between the predictions of the two resolved CFD models. This is not surprising as the swirling effect can be difficult to be accurately captured by eddy viscosity models. The SubChCFD follows that of the trend of the SST-k-ω better.

Significant temperature fluctuations are observed in all models which are primarily due to the influence of the wire spacers. These spacers periodically disrupt the flow, causing localized velocity variations and enhanced heat transfer, which lead to temperature oscillations. The SST (NRCKI) and SST k-ω (NCEPU) models exhibit more fluctuations, whereas SubChCFD produces a smoother temperature profile. This difference arises because, in resolved CFD, the wall temperature is extracted at a single location within the subchannel, whereas in SubChCFD, the data represents an averaged wall temperature over subchannels.

Additionally, in the axial wall temperature distributions, several local dips are observed along the streamwise direction. These lower temperature spikes are attributed to the wire-induced local enhancement of heat transfer. The presence of the wire promotes crossflow and mixing between subchannels, which enhances convective heat transfer and locally reduces the wall temperature. SubChCFD does not explicitly account for mixing effects in the Nusselt number correlation, though the predicted temperature profiles still exhibits some small enhanced heat transfer. This indicates that the momentum source term approach indirectly captures some impact of wire spacers on heat transfer through its influence on the flow field, but if local peak temperature is required, further explicit correlation should be included.

Finally, it is interesting to note the significantly different wall temperature increases in the different subchannels. In center subchannels, the wall temperature increase streamwise is the lowest due to a strong axial flow. In contrast, edge and corner subchannels have a lower flow through them and hence a greater increase in local bulk temperature and hence also a greater increase in wall temperature. SubChCFD has captured these differences in the subchannels very well, demonstrating its capability to capture the key thermal-hydraulic features, such as temperature variations and local enhancements in heat transfer.

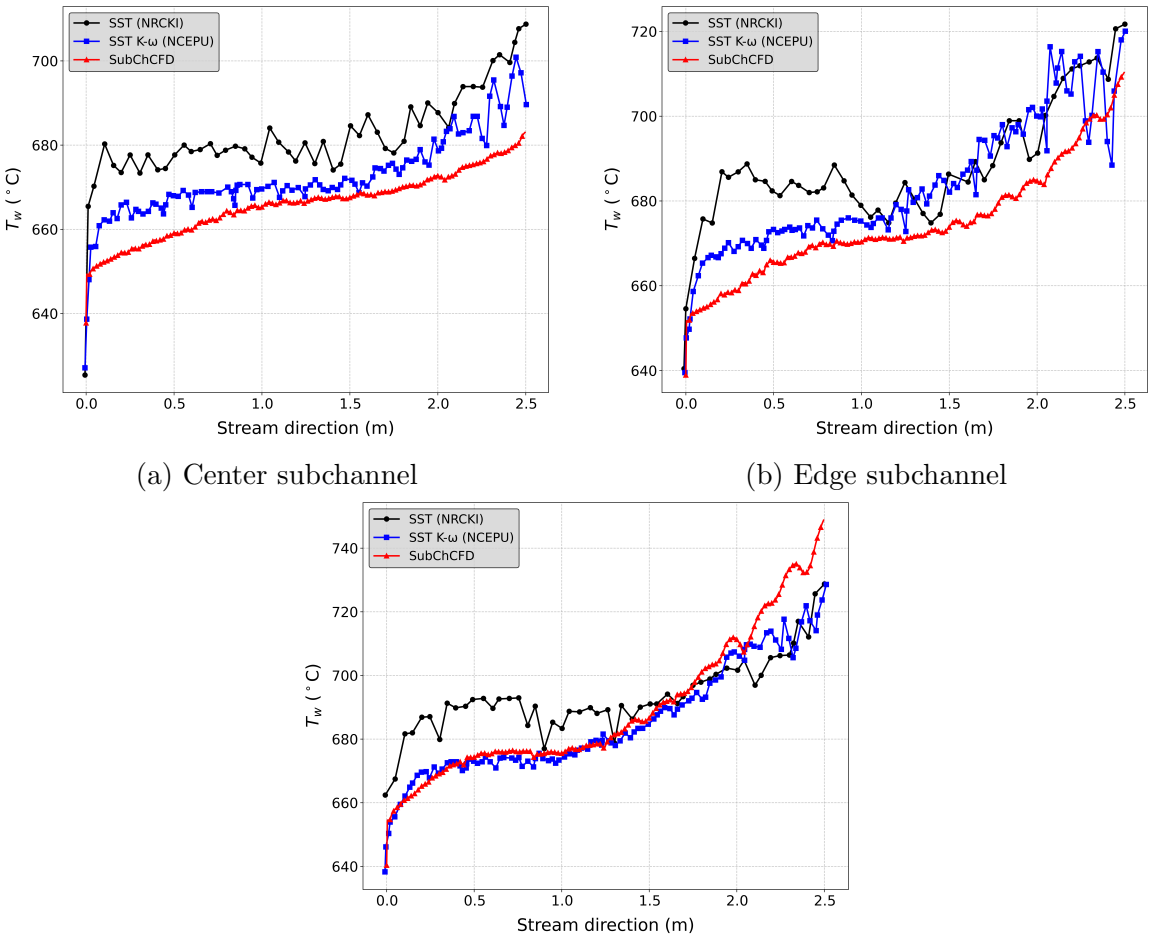

(a) Center subchannel

(b) Edge subchannel

(c) Corner subchannel

Figure 5.12: Comparison of wall temperature distributions at different subchannels.

While temperature fluctuations in the wall temperature profiles obscure the lower-temperature spikes due to the wire effect, the HTC profile can provide a clearer depiction of the periodic enhancement of heat transfer. Figure 5.13 presents the comparison of HTC along the streamwise direction for different models. The strong periodic peaks observed in HTC profiles observed in the resolved CFD (especially case blue) highlight the influence of the wire spacers. These HTC are local valuies but, in SubChCFD, the presented HTC results represent the average heat transfer coefficient around each rod, calculated based on a spatially weighted average of the corresponding subchannel region. The SubChCFD is clear capable of capturing the thermal behaviour associated with flow disturbances introduced by the spacers despite a much small magnitude due the the average.

The SubChCFD results show relatively higher HTC values compared to the other models, which suggests that the heat transfer correlation used in SubChCFD may be

over predicting the enhancement effect. However, the overall trend and periodicity align well with the predictions from SST (NRCKI) and SST k-ω (NCEPU). This indicates that SubChCFD successfully captures the key thermal phenomena associated with wire-wrapped rod bundles.

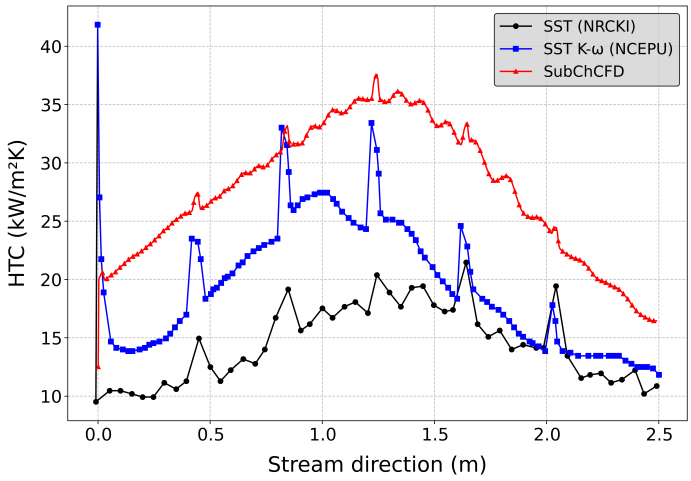

Figure 5.13: Comparison of the heat transfer coefficient (HTC) along the streamwise direction.

In conclusion, the validation of SubChCFD in the locally wire-wrapped case under supercritical conditions confirms its capability to capture the key flow and heat transfer phenomena associated with this geometry. Comparisons with resolved CFD models show that SubChCFD predicts the overall trends well, with reasonable agreement in velocity distribution, pressure loss and heat transfer behaviour.

5.4.3 Fully wire-wrapped

This section demonstrates the application of SubChCFD for fully wire-wrapped rod bundles under supercritical conditions.

Figure 5.14 illustrates the velocity vector field within the rod bundle at different axial positions, showing the impact of the wires on flow behaviour in fully wire-wrapped configuration. Three cross-sectional slices are extracted at different locations along the streamwise direction to show the evolving flow patterns.

The velocity vectors reveal that the wire spacers continuously drive crossflow between subchannels. This swirling motion persists along the entire rod length due to the continuous helical wrapping, which could impact pressure loss and wall temperature prediction depending on the extent of the resulting flow redistribution. The

ability of SubChCFD to capture these wire-wrapping effects offers a new avenue for accurate thermal hydraulic predictions in supercritical conditions.

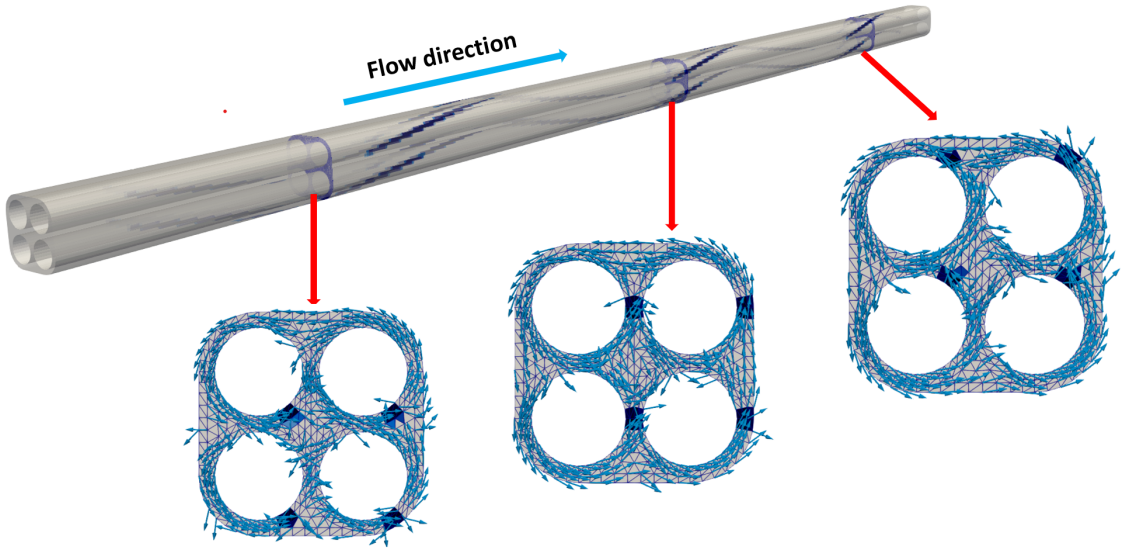

Figure 5.14: Velocity vector field at different axial locations in the fully wire-wrapped rod bundle.

Figure 5.15 shows the axial bulk velocity along the streamwise direction for three different subchannels (center, edge, and corner) for Case 2 and Case 3. The center subchannel consistently exhibits the highest velocity, with a smooth and steady increase along the axial direction, indicating a more uniform and less obstructed flow. This behaviour is due to the relatively uniform obstruction caused by the wire spacers along the axial direction in the center subchannel, resulting in smoother flow development and smaller velocity variations.

In contrast, the edge and corner subchannels exhibit periodic variations in velocity, which result from the periodic obstruction caused by the wire spacers. The wire distribution within the edge subchannel at 0.15m to 0.25m is shown in Figure 5.16. This leads to localised flow acceleration and recovery within each subchannel as the flow moves downstream. SubChCFD successfully captures these effects, demonstrating its capability to reproduce the effects of wire wrapping in each subchannel.

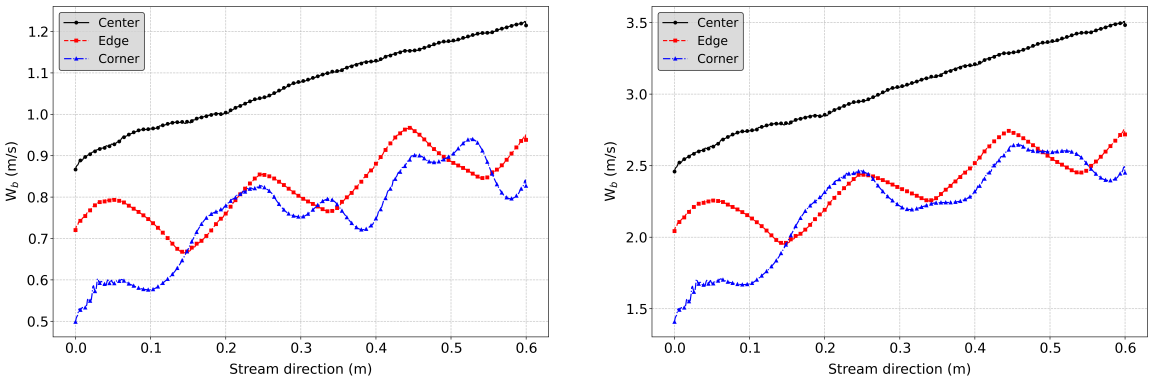

(a) Case 2. (b) Case 3.

Figure 5.15: Axial bulk velocity distribution within differnet subchannels along the streamwise direction.

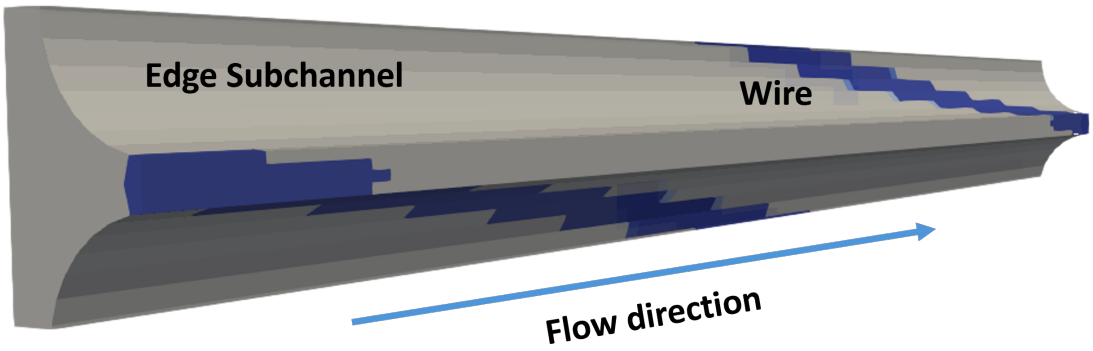

Figure 5.16: Wire distribution in the edge subchannel at 0.15m to 0.25m.

Figure 5.17 compares the pressure distribution along the streamwise direction. In both cases, the SubChCFD prediction of pressure drop is in good agreement with that of Advanced Thermal-hydraulic Analysis Sub-channel code (ATHAS). This validation shows that SubChCFD is capable of predicting pressure losses in fully wire-wrapped rod bundles under supercritical conditions with reasonable accuracy.

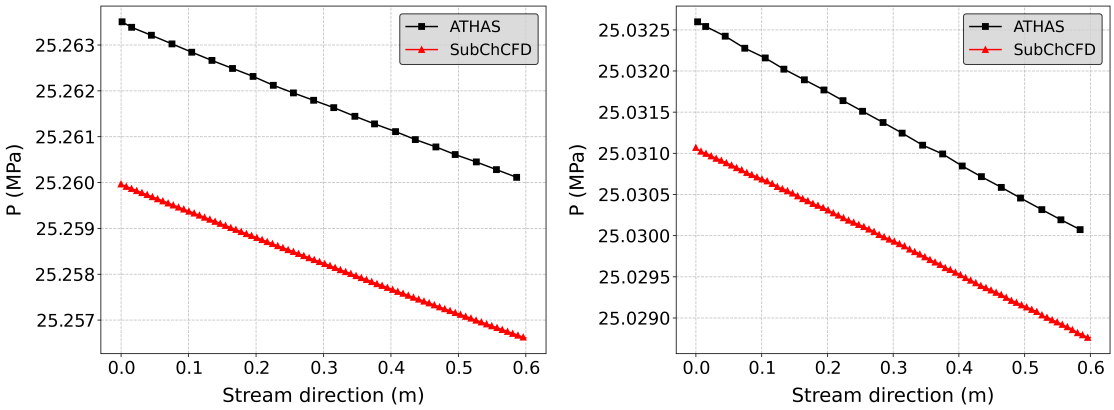

(a) Case 2. (b) Case 3.

Figure 5.17: Comparison of axial pressure drop.

Figure 5.18 compares the average wall temperature along the streamwise direction for Case 2 and Case 3. The results of SubChCFD are compared against those of CFD stimulations from other participants [38], in which the k-ω SST turbulence model was used. The SubChCFD results show a similar increasing trend in wall temperature along the streamwise direction when compared to the CFD results. However, the temperature values predicted by SubChCFD are generally lower compared to the CFD predictions. Similar discrepancies were observed in the previous research chapter, suggesting that further investigation is needed to compare these predictions with experimental data. Despite these differences, the temperature variation across all models remains relatively close, with differences ranging from approximately 5 K to 15 K.

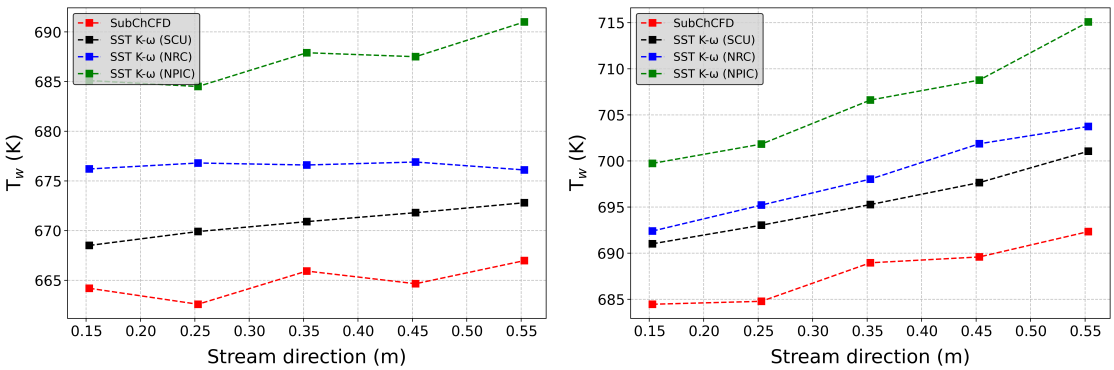

(a) Case 2. (b) Case 3.

Figure 5.18: Comparison of the average wall temperature along the streamwise direction.

The predicted axial pressure drop and wall temperature trends show close agreement with resolved CFD results, demonstrating SubChCFD's ability to predict the global thermal-hydraulic behaviour in fully wire-wrapped rod bundles.

The analysis in this section primarily focuses on the overall temperature and pressure drop predictions in the axial direction. However, the cross-sectional flow distribution, particularly the effects of crossflow induced by wire spacers, remains an important aspect for further demonstration.

5.4.4 The 7-Pin channel

The 7-pin bundle case serves as a demonstration of SubChCFD's capability to predict crossflow behaviour in a more complex rod bundle geometry. This section focuses on analysing the swirling motion induced by wire spacers, comparing simulation results with experimental data. Velocity distributions and crossflow intensity are examined across different subchannels to assess the SubChCFD's ability in capturing key flow phenomena.

Figure 5.19 presents the crossflow distribution within the 7-pin bundle geometry at the same cross-sectional location, comparing experimental observations with the results obtained from SubChCFD. The velocity vectors reveal distinct swirl patterns across the entire domain, with localized vortex structures forming in specific subchannel regions. The colour map further illustrates the intensity of crossflow, where regions with higher intensity (yellow to red) correspond to areas of high flow, particularly within narrow gaps between the walls and pins, as well as downstream of the wire spacer region.

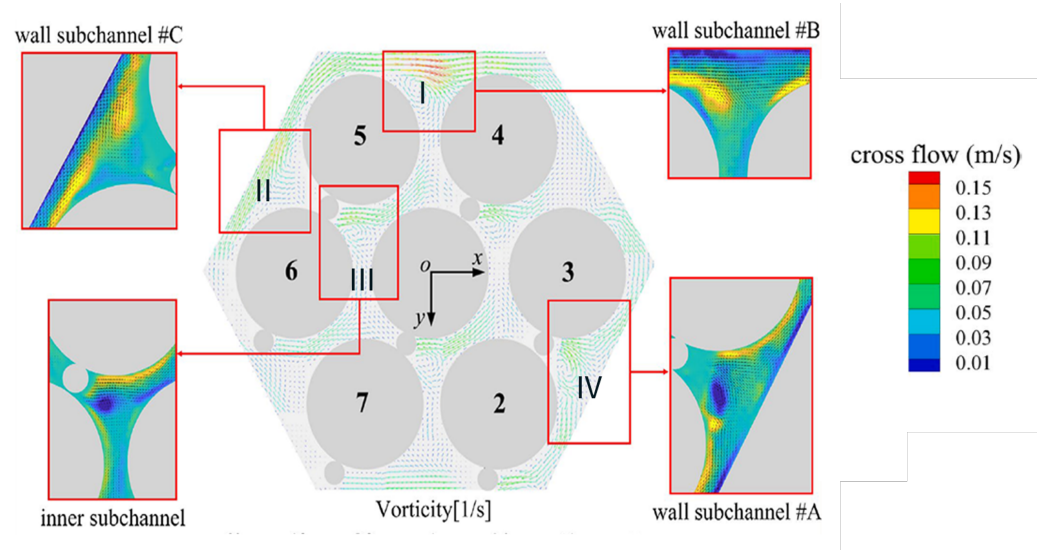

(a) Experimental crossflow visualization.

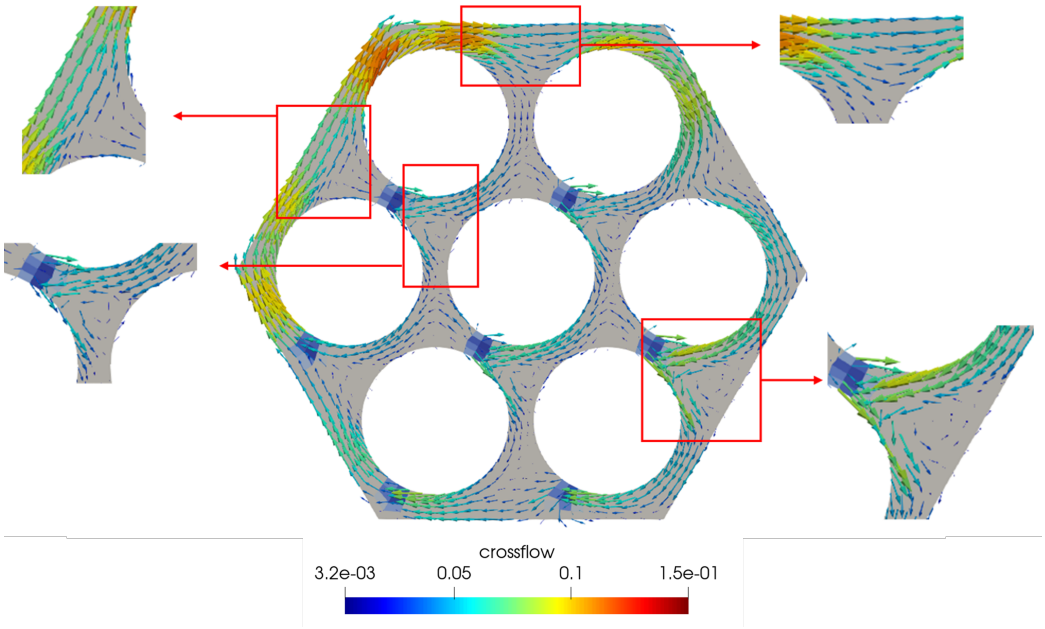

(b) Crossflow prediction using SubChCFD.

Figure 5.19: Comparison of experimental and SubChCFD-predicted crossflow distributions within the 7-pin bundle.

The zoomed-in subchannel regions provide a detailed comparison of the predicted and experimental flow fields. Despite the use of a coarse grid, the SubChCFD model effectively captures the primary crossflow features and some localized vortex structures near the wire in inner and edge subchannels. These vortices are generated as a result of the obstruction caused by the wire spacer. When the crossflow is blocked by the wire, it leads to localized flow reversal and vortex formation within the subchan-

nel. While the local vortices are well reproduced, generally speaking, variations in their exact center locations and sometime the intensities, compared to experimental data are observed. This discrepancy may be attributed to the coarse grid resolution. The results indicate that the implemented forces effectively account for the wire spacer effects on crossflow behaviour.

Figure 5.20 presents a comparison of the velocity vector fields in the inner subchannel, highlighting localized vortex formation due to crossflow interactions. The alignment of velocity patterns between the experimental results and SubChCFD predictions suggests that SubChCFD effectively captures the overall crossflow behaviour in this region, including the presence of swirl and vortex structures.

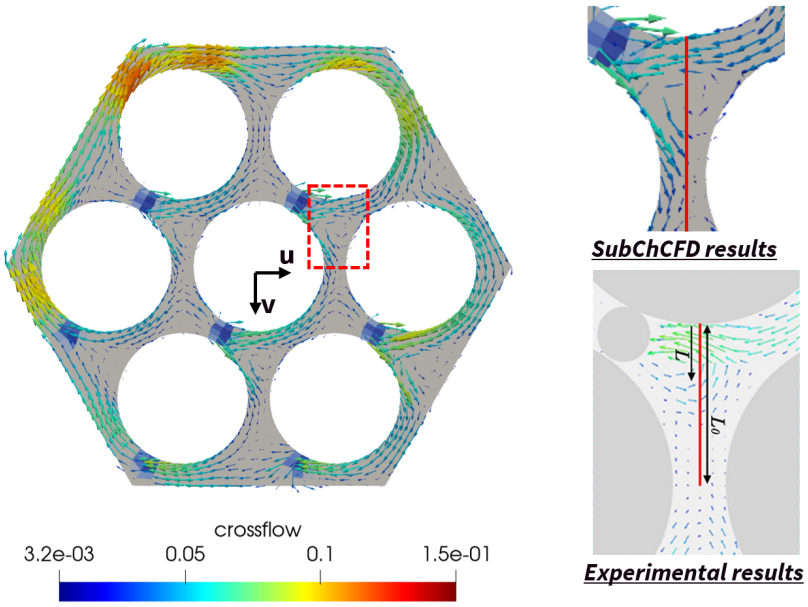

Figure 5.20: Comparison of velocity vector fields in the inner subchannel of the 7-pin bundle.

Figure 5.21 provides a quantitative comparison of the normalized velocity components within the subchannel. The plots display the normalized velocity u/w and velocity v/w at three different Reynolds numbers: 3000, 6000, and 9000.

In the u/w plot, the SubChCFD results align well with the experimental data. The characteristic velocity dip around $L/L_0 = 0.2$, followed by a subsequent recovery, is accurately captured. This behaviour is associated with vortex-induced flow patterns within the inner subchannel.

The v/w plot further demonstrates the SubChCFD model's ability to capture local vortices arising from crossflow interactions. The v/w in the region L/L_0 between 0.3

to 1.0 is well predicted by the subchcfd, but the values between L/L_0 between 0 and 0.3 seem to be significantly lower, in fact with the wrong sign (that is, in the wrong direction). This is a result of the local vortex predicted by the subchcfd model is shifted in relation from the measurement, see, Figure 5.20. Such level of deviation in the SubChCFd is expected and it demonstrate the limitation of the coarse grid resolution in resolving fine-scale turbulence structures.

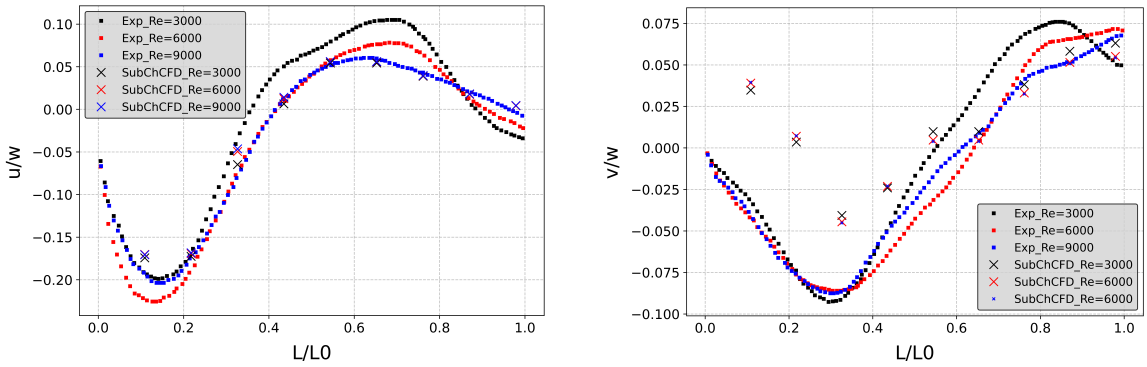

(a) Normalized streamwise velocity u/w.

(b) Normalized lateral velocity v/w.

Figure 5.21: Comparison of normalized velocity components in the inner subchannel.

Figure 5.22 presents a comparison of velocity vector fields in the edge subchannel. The overall swirling motion in the entire section is well captured by SubChCFD. However, the SubChCFD model underpredicts the magnitude of the velocity in certain regions. The local vortex observed in the experimental data near the wire spacer is not reproduced in the simulation, again showing the limitation of SubChCFD in capturing detailed local flow structures.

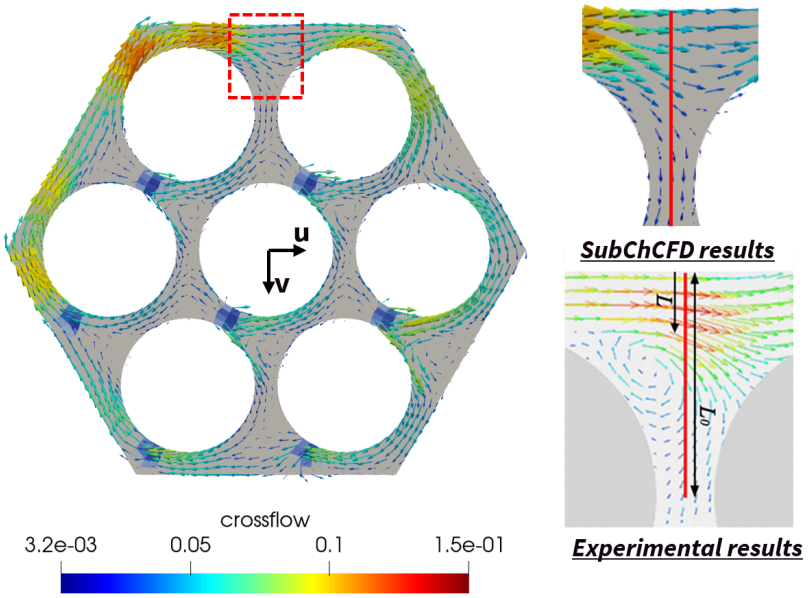

Figure 5.22: Comparison of velocity vector fields in the edge subchannel of the 7-pin bundle.

Figure 5.23 presents a quantitative comparison of the normalized velocity components in the edge subchannel. Consistent with the observation of a strong vortex in the edge channel (Figure 5.22), the experimental data shows a strong positive peak in both u and v. However, the subChCFD does not capture these peaks due to the lack of vortex in this region likely due to the use of coarse grid CFD. The predictions away from the wall, L/L_0 ¿ 0.6, agree reasonably well with the experimental data. Despite of this, the SubChCFD is able to predict significant cross flow due to the overall swirling effect caused by the wire wrap.

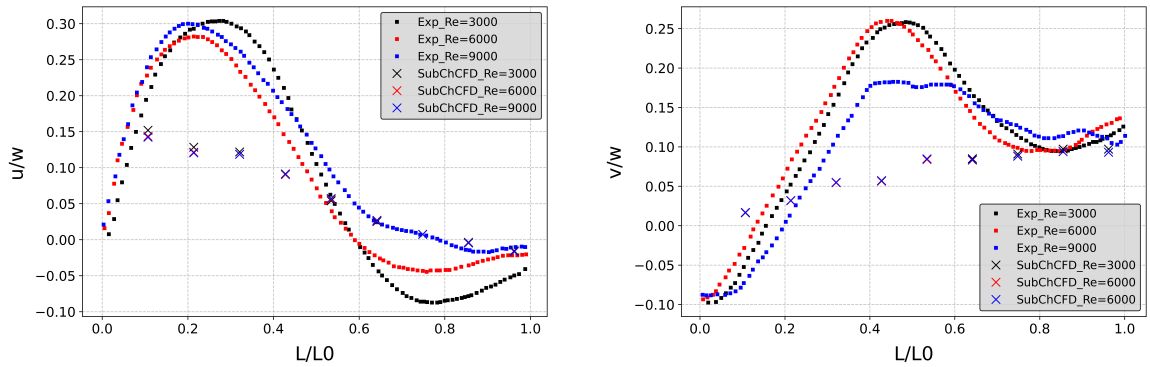

(a) Normalized streamwise velocity u/w.

(b) Normalized lateral velocity v/w.

Figure 5.23: Comparison of normalized velocity components in the edge subchannel.

Figure 5.24 illustrates the velocity field in the corner subchannel. The velocity

vectors indicate strong crossflow effects induced by the wire spacers, with higher flow intensity near the pin walls and reduced velocities closer to the housing wall due to the hexagonal channel geometry, which is shown in both the experimental data and the SubChCFD prediction.

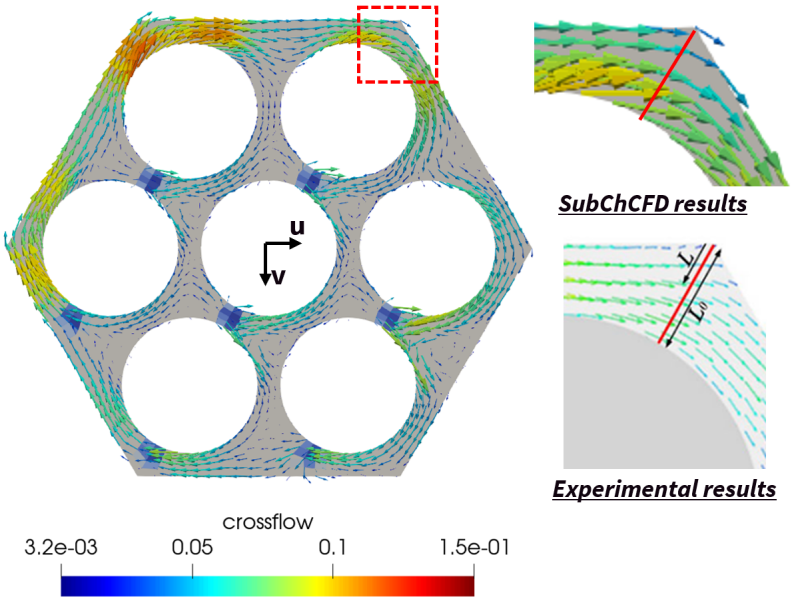

Figure 5.24: Comparison of velocity vector fields in the corner subchannel of the 7-pin bundle.

Figure 5.25 compares the crossflow intensity between experimental data and SubChCFD simulations in the corner subchannel. The overall profile of the cross-flow velocity is well captured by SubChCFD. Higher velocity regions are observed near the pin walls, indicating swirling induced acceleration, while lower velocity values appear closer to the housing wall. This variation is due to the hexagonal channel geometry, where the corner region is not perfectly round, leading to a non-uniform velocity profile. Despite the limited number of mesh layers in this region, SubChCFD successfully captures this geometry induced effect.

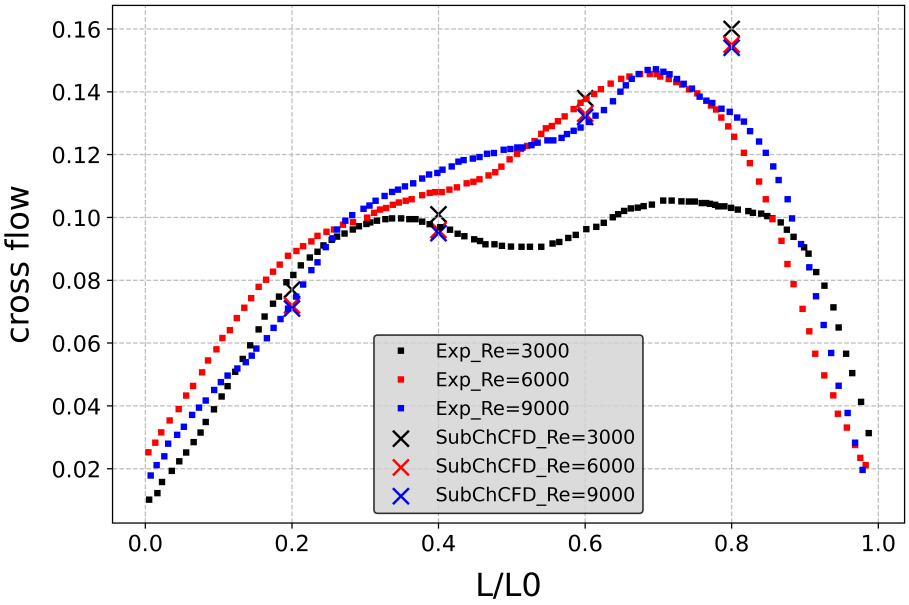

Figure 5.25: Comparison of crossflow intensity in the corner subchannel.

However, at $Re = 3000$, the experimental results exhibit a different trend compared to higher Reynolds numbers, which is not reproduced by SubChCFD. At lower Reynolds numbers, the crossflow intensity is weaker, indicating reduced secondary flow motion. The SubChCFD model appears to over predict the influence of wire spacers at these lower flow conditions, suggesting that further refinement of the momentum source term may be necessary.

The results indicate that SubChCFD effectively predicts the dominant swirling behaviour in the corner subchannel. However, further calibration of the momentum source term is required to improve accuracy across different flow conditions, particularly at lower Reynolds numbers where the model tends to overestimate the wire spacer effect.

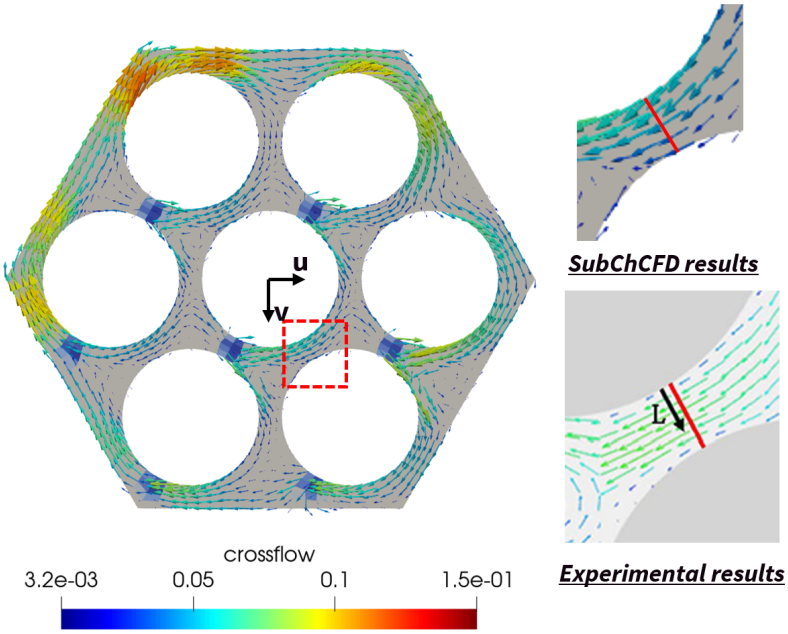

Figure 5.26: Comparison of velocity vector fields in the inner subchannel between two rods in the 7-pin bundle.

Figure 5.26 presents the velocity distribution in the region between two adjacent rods. This region is also important as it highlights the dominant crossflow interactions driven by the swirling motion around the rods. The velocity vectors indicate a tangential flow component along the pin surfaces, demonstrating the effect of flow redirection caused by the wire spacers in both the measurements and the SubChCFD predictions.

The comparison of crossflow intensity between experimental data and SubChCFD simulations is shown in Figure 5.27. The strong crossflow velocity highlights the influence of swirling motion induced by the wire spacers along the rod walls. A noticeable asymmetry in the SubChCFD profile suggests that the flow has not fully recovered from the upstream center subchannel effects, where swirling interactions have altered the local flow characteristics.

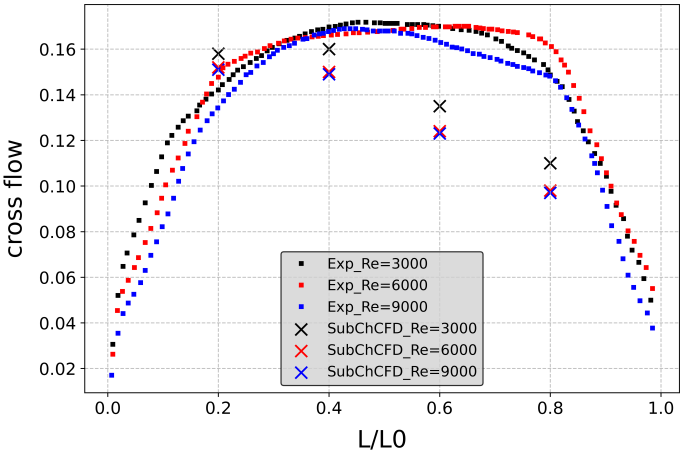

Figure 5.27: Comparison of crossflow intensity between pins.

Despite some discrepancies in velocity magnitudes with experimental data, the SubChCFD model effectively captures the overall crossflow behaviour in this region, demonstrating its capability to predict dominant flow trends.

The 7-pin bundle demonstration confirms that SubChCFD can capture dominant crossflow behaviour, including swirling motion and local vortex structures in certain subchannels. While it successfully predicts velocity distribution and crossflow intensity, some discrepancies in magnitude and vortex center location persist due to grid resolution limitations. Overall, SubChCFD effectively reproduces key flow characteristics, demonstrating its capability for crossflow prediction in various geometries.

5.5 Conclusions

This chapter presents a new development in SubChCFD for the simulation of wire-wrap effects, where pseudo forces are used to account for the wire effect rather than resolving the complex wire geometry. The validation was conducted in locally and fully wire-wrapped cases under supercritical conditions, assessing temperature distribution and pressure drop along the axial direction. The 7-pin bundle case further validated the model's capability in predicting crossflow behaviour in a more complex setting.

SubChCFD successfully captured the axial pressure drop and heat transfer characteristics in both the locally and fully wire-wrapped cases, showing reasonable agreement with CFD results. The periodic influence of wire spacers on flow redistribution was well represented. In the fully wire-wrapped case, SubChCFD captures the global behaviour well: the axial trends of temperature and pressure are reproduced, and

key flow features are present. Minor temperature discrepancies point to limits of the heat-transfer correlation, but the method delivers these results at substantially lower computational cost than resolved CFD.

The 7-pin bundle case confirmed the ability of SubChCFD to predict crossflow behaviour induced by wire spacers. The model captures dominant swirling motion and local vortex structures in different subchannels. Some deviations in vortex strength and position were observed due to the coarse grid limitation.

Overall, SubChCFD with new development proves to have the ability to model axial and radial flow and heat transfer behaviour in wire-wrapped rod bundles.

Chapter 6

Application of SubChCFD in natural circulation loops

6.1 Introduction

Natural circulation loops are relevant to passive cooling systems in nuclear reactors, as they enable coolant circulation without relying on external pumps. The main objective of this chapter is to demonstrate the capability of SubChCFD in simulating the transient behaviour of a natural convection loop. Two distinct configurations are examined: one features horizontal heating and vertical cooling (HHVC), where an asymmetric heater-cooler arrangement creates a preferential initial flow direction. The other configuration features horizontal heating and horizontal cooling (HHHC), with both sections positioned symmetrically, resulting in more uniform initial flow development.

To enable the modelling of NCLs using SubChCFD, development is focused on several key aspects, including implementation of friction factor correlations for straight pipes, modifications to Nusselt number correlation to account for thermal boundary development and calibration of shear stress in elbow regions. The effectiveness and limitations of SubChCFD in capturing instabilities in natural circulation loops is assessed by comparing its prediction with detailed CFD results for velocity and temperature oscillations, as well as flow reversals.

6.2 Model development

6.2.1 Friction factor correlations for pipe flow

In previous chapters, the development of SubChCFD has primarily focused on rod bundles, whereas this case involves pipe flow. Since SubChCFD relies on empirical

correlations, correlations developed for pipe flows are used. In addition, for the natural circulation loop, flow may be laminar, transitional or turbulent, which needs to be accounted for.

In a straight pipe, the flow transitions through different regimes are illustrated in the Moody diagram, which is shown in Figure 6.1, each regime requiring a specific friction factor correlation.

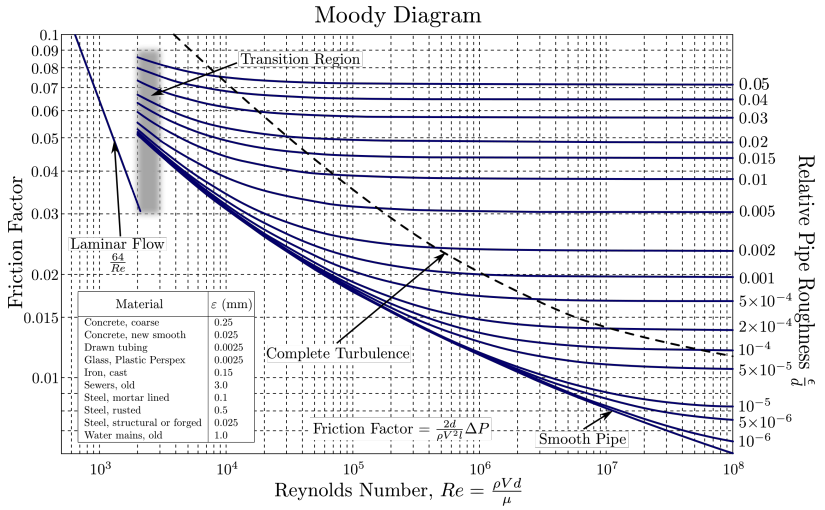

Figure 6.1: Moody diagram [132].

In SubChCFD, the following correlations are implemented. For laminar flow (Re $<$ 2000), the friction factor is determined as [130]:

$$f = \frac{64}{\mathrm{Re}} \tag{6.1}$$

For transitional flow ($2000 < \mathrm{Re} < 3000$), where the flow characteristics are more complex due to the onset of turbulence, an empirical correlation proposed by Swapnalee and Vijayan [114] is applied:

$$f = \frac{1.2063}{\mathrm{Re}^{0.416}} \tag{6.2}$$

For moderate turbulent flow ($3000 < \mathrm{Re} \leq 20,000$), the Blasius correlation [130] is used to estimate the friction factor:

$$f = \frac{0.316}{\mathrm{Re}^{0.25}} \tag{6.3}$$

For higher turbulence levels ($20,000 < \mathrm{Re} < 200,000$), an improved Blasius correlation, validated by Fang et al. [39], provides a more accurate prediction of the friction factor:

$$f = \frac{0.184}{\mathrm{Re}^{0.2}} \tag{6.4}$$

By implementing these friction factor correlations, SubChCFD can properly predict flow resistance across different flow regimes in pipe geometries. This development enhances its applicability beyond rod bundle based configurations, making it suitable for modelling a wider range of thermal-hydraulic systems.

6.2.2 Friction loss in the elbow region

For the simulation of the whole natural circulation loops, the elbow sections present additional challenges. The elbow regions contribute to head loss through both physical and numerical mechanisms. Physically, elbows cause form losses due to flow separation, curvature effects, and the generation of secondary flows. Conversely, numerical diffusion is an unwanted computational artefact associated with the use of a coarse mesh. It is necessary to consider all these effects in the elbow regions.

For the SubChCFD development, the wall shear stress in the elbow region is implemented as a momentum source expressed as:

$$\tau_w = -\frac{1}{2}\rho k u|u| \cdot \frac{d}{(2R+d)\pi} = -\frac{1}{2}\rho K u|u| \tag{6.5}$$

where K is the loss coefficient (K = 0.04 in this case), ρ is the density and u is the local velocity.

The shear stress is implemented within the elbow region for this specific case. The coarse-grid pressure drop was matched to the fine-mesh RANS simulations for the same conditions. This new development allows SubChCFD to account for frictional losses, form losses, and numerical dissipation effects in the elbow region, which are otherwise not captured by SubChCFD.

6.2.3 Nusselt number correlation

As the fluid enters the heated and cooled sections, it experiences an entrance effect, which is relevant to the development of the thermal boundary layer and should be taken into account in the heat transfer correlations used. In addition, the flow experiences strong axial temperature gradients due to the developing thermal boundary layer. As the fluid enters the heated or cooled section, temperature changes rapidly along the axial direction, which should be modelled appropriately to ensure realistic simulation outcomes by using a reasonably fine mesh.

For fully developed flow, standard correlations can be used, such as the Dittus-Boelter equation for turbulent flow [37]:

$$Nu = 0.023 Re^{0.8} Pr^{0.4} \tag{6.6}$$

However, in the entrance region, where the thermal boundary layer is still developing, the correlation needs to be corrected to account for the evolving heat transfer characteristics. In Chapter 4, heat transfer in supercritical conditions was discussed using the Bishop correlation, which is widely used for turbulent flow in rod bundle geometries. However, in this chapter, thermal entrance effects are significant for natural circulation in a square loop pipe configuration due to the short heated and cooled sections. To account for the developing thermal boundary layer, a modified Dittus–Boelter correlation with an entrance-length correction (Incropera et al. [13]) expressed as:

$$Nu_x = 0.023\, Re^{0.8}\, Pr^{0.4} \left(\frac{x}{D}\right)^{-0.05} \tag{6.7}$$

Here, Nu_x is the local Nusselt number at an axial position x, x is the distance from the pipe inlet, and D is the pipe diameter. The correction term $\left(\frac{x}{D}\right)^{-0.05}$ accounts for the thermal entrance development. This effect is typically significant near the start of heating/cooling and gradually diminishes as the flow approaches fully developed conditions.

In SubChCFD, this correlation is considered to correct the heat transfer coefficient in the entrance regions, ensuring that both the heated and cooled sections properly account for the thermal development. However, implementing this correction presents a challenge. Due to flow oscillations and flow reversal, the actual entrance to the heating or cooling section depends on the instantaneous flow direction, making it difficult to define consistently. This part of the development work is quite challenging and still ongoing.

In this work, a simplified calibration approach was adopted to demonstrate the capability of SubChCFD in modelling NCL behaviour. For a specific test case, the average Nusselt number in the cooling section was estimated based on resolved CFD simulations and from SubChCFD using the Dittus–Boelter correlation [37] respectively. To align the heat transfer predictions between the two approaches, a correction coefficient was applied to the Nusselt number estimated in SubChCFD. This coefficient was calibrated such that the resulting Nusselt number closely matched that from the resolved CFD, ensuring comparable heat transfer performance. This calibration

is specific to the present case, as the heating and cooling sections are relatively short and the thermal boundary layers are never fully developed. This calibrated Nusselt number helps to account for the influence of thermal development over the entire length.

6.3 Case description

To investigate the flow behaviour in a natural circulation loop and evaluate the capabilities of SubChCFD, a square-shaped loop is considered in this study. The reference geometry is based on work by Dean et al. [134], as illustrated in Figure 6.2. The detailed geometric parameters of the loop are provided in Table 6.1. The heater is located at the centre of the bottom horizontal pipe, where a constant heat flux is applied as the heat input. The cooler is positioned at the top-right vertical section or the centre of the top horizontal pipe, where a constant temperature boundary condition is imposed.

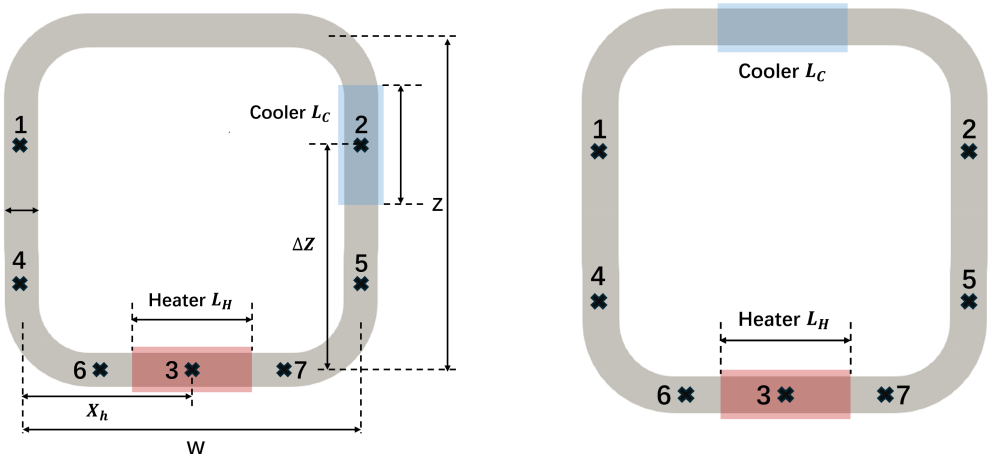

(a) HHVC. (b) HHHC.

Figure 6.2: Geometry information of the square loop configuration.

Table 6.1: Dimensionless geometric parameters of the square natural circulation loop.

Configuration	H/δ	Z/W	R/δ	$\Delta Z/Z$	L_H/W	X_h/W
Square Loop	10	1	1.5	0.675	0.35	0.5

To capture the flow characteristics and assess transient behaviour within the loop, seven monitoring points are placed at different locations across the loop, as indicated in Figure 6.2a. These monitoring points enable the analysis of velocity fluctuations,

temperature variations, and flow direction changes, providing insights into the dynamic behaviour of the system.

The operating conditions of the system are summarised in Table 6.2. The fluid properties are assumed to be constant. The Boussinesq approximation is used to account for buoyancy effects. The Boussinesq approximation models buoyancy by assuming the fluid is incompressible with constant properties everywhere except in the gravity/body-force term. A constant heat flux is applied in the heated section, while the reference temperature corresponds to the initial temperature in the system. The constant wall temperature in the cooling section is slightly lower than the initial temperature, establishing an initial buoyancy-driven flow.

Table 6.2: Thermal physical conditions.

Ra	Gr	Pr	ρ	μ	β	c_p	q''	T_{ref}	T_{cool}
–	–	–	(kg/m^3)	(Pa·s)	(1/K)	(J/kg·K)	(W/m^2)	(°C)	(°C)
8.07×10^{13}	1.13×10^{13}	7.1	1000.0	0.001	0.1	4000.0	4.87×10^7	19.5	19.0

6.3.1 Mesh generation

The low Reynolds number Launder-Sharma turbulence model is used based on findings from the literature, where it has been shown to provide satisfactory performance in circulation loop systems [74, 133]. This turbulence model is used in resolved CFD simulations to generate reference results.

A structured mesh is generated, with special refinement near the wall regions to ensure that the dimensionless wall distance (y^+) remains close to 1. For the cross-section of the pipe, an O-grid mesh topology is utilised to maintain high mesh quality and improve numerical stability in curved geometries.

The RANS CFD simulation employs a high-resolution mesh, as shown in Figure 6.3. A fine mesh is particularly important in natural circulation loop simulations to accurately capture boundary layer effects and turbulence characteristics.

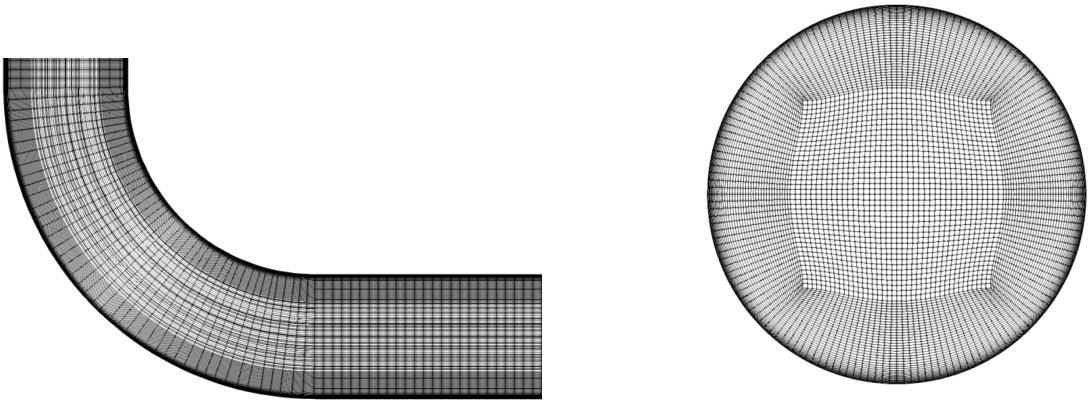

(a) Mesh for the elbow region. (b) Cross-sectional O-grid mesh.

Figure 6.3: Mesh structure used in resolved CFD simulations.

In SubChCFD, a similar meshing strategy is adopted, but it is significantly coarser compared to the resolved CFD mesh, as shown in Figure 6.4. The filter mesh generation for SubChCFD differs from rod bundles meshing. In this configuration, only one subchannel covers the entire cross-section of the pipe, unlike the multiple subchannels used in previous subchannel models. Additionally, the filter mesh is applied only to the straight pipe sections (red regions), as shown in Figure 6.4a.

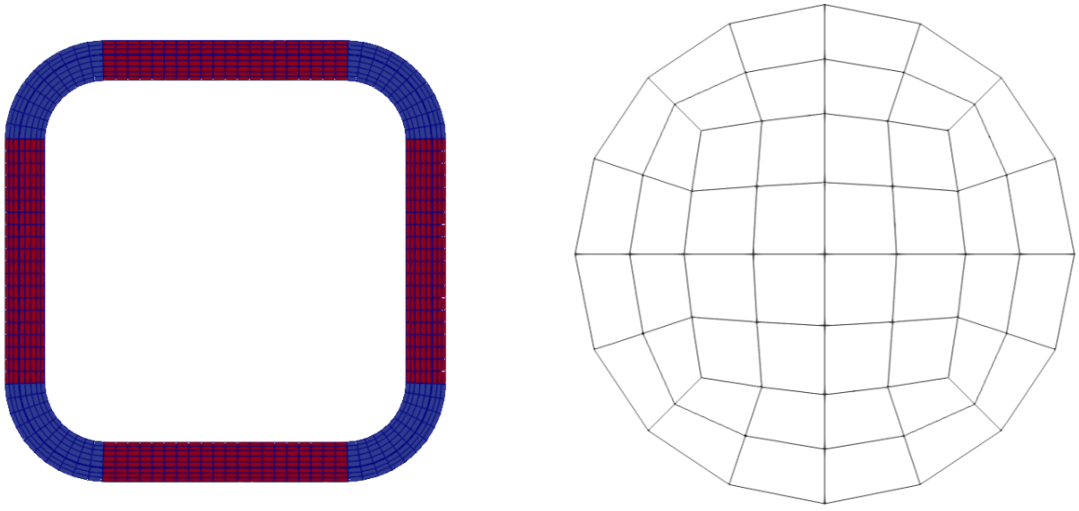

(a) Coarse mesh in a curved pipe section. (b) Coarse cross-sectional mesh.

Figure 6.4: Mesh structure used in SubChCFD simulations.

6.4 Results and discussion

6.4.1 Horizontal heating and vertical cooling

Figure 6.5 presents the horizontal velocity U at three monitoring points in the natural circulation loop: monitor 3 (heated section), monitor 6, and monitor 7. Across all monitoring points, both CFD and SubChCFD results exhibit oscillations in velocity, indicating flow instability within the system. The velocity magnitude fluctuates between positive and negative values, indicating frequent reversals of flow. This behaviour is characteristic of the unstable flow conditions that can occur in natural circulation loops. SubChCFD generally captures the oscillation frequency well but slightly deviates in amplitude. The frequency differences are minimal across all monitoring points, suggesting that SubChCFD successfully predicts the overall oscillatory nature of the system.

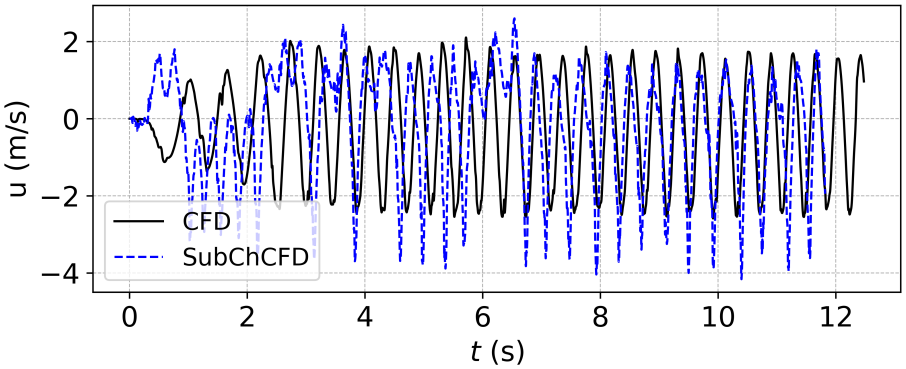

(a) Monitor 3

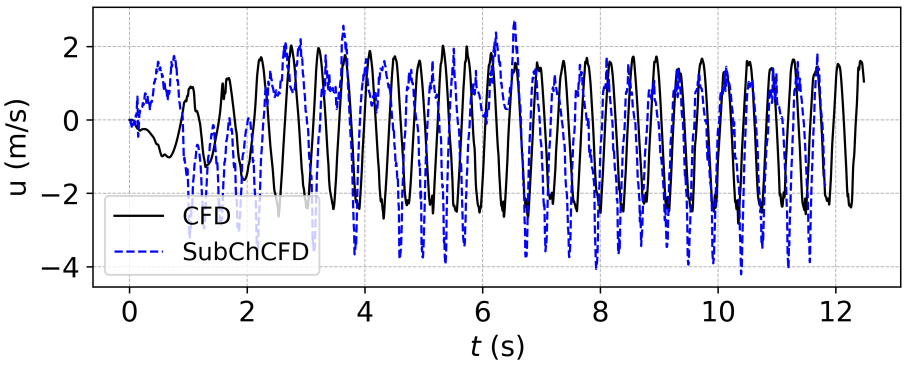

(b) Monitor 6

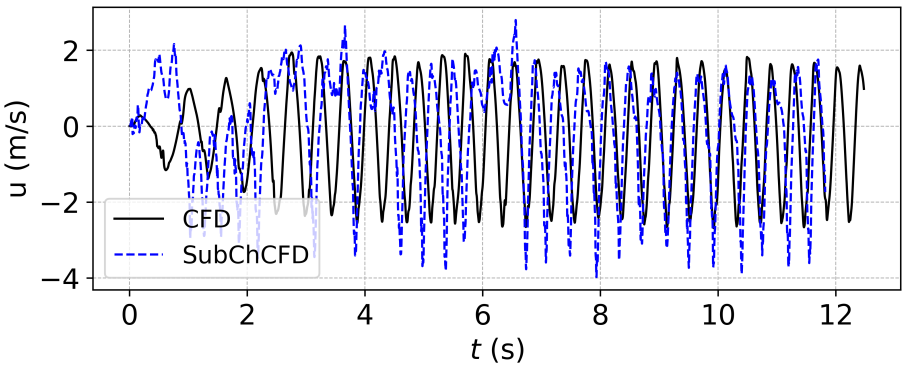

(c) Monitor 7

Figure 6.5: Time history of horizontal velocity at different locations.

Figure 6.6 compares temperature evolution between the resolved CFD and SubChCFD methods at three monitoring locations. The values are very high as the cases are all designed for the comparison by referring to Dean's research [134] . The results show that SubChCFD follows the overall trend of the CFD results, capturing the periodic transient heating process and fluctuation phenomena. Both the amplitude and the frequency of the oscillations have been in points 1 and 2 agree well between the

two simulations. The agreement is worse at point 3 though the basic unsteady feature has been captured by SUbChCFD. These fluctuations indicate flow instabilities. After applying the calibrated Nusselt number to account for the overall developing effect, the thermal performance predicted by SubChCFD closely matches that of the RANS simulation.

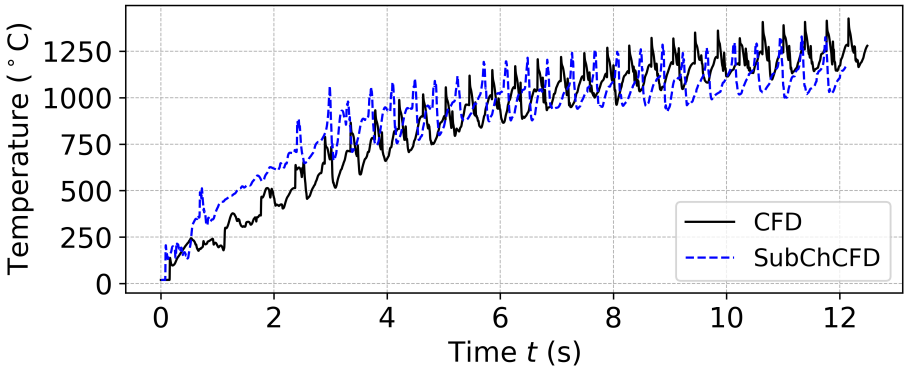

(a) Monitor 1

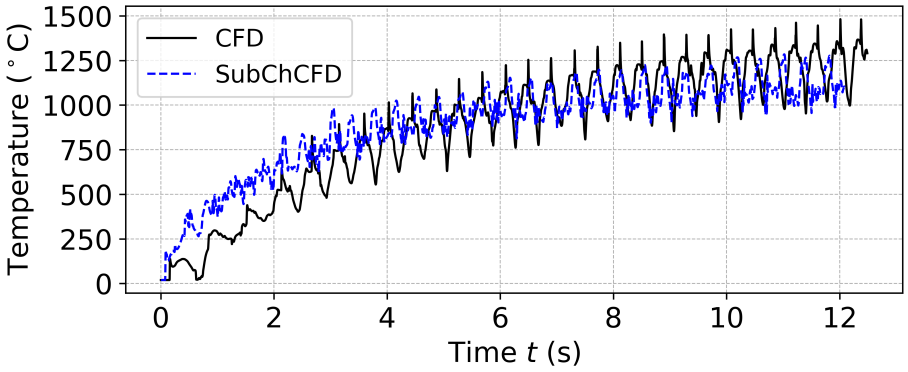

(b) Monitor 2

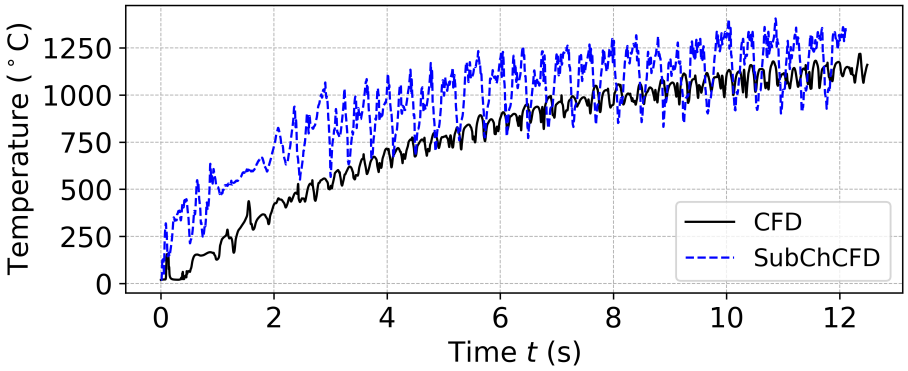

(c) Monitor 3

Figure 6.6: Temperature comparison of CFD and SubChCFD results at different locations.

Figure 6.7 presents temperature contour plot at different time instances. These results again suggest the oscillatory flow behaviour within the loop, including the flow reversal. Although the exact timing of the transitions differs slightly between the models, both SubChCFD and resolved CFD exhibit the same dynamic trend.

Initially, the flow moves in an anti-clockwise direction (judging by noticing the heated hot fluid moving to the left) due to thermal expansion in the heated section (t=9.79s). As the coolant continues to absorb heat and moves toward the cooler region on the right, the flow gradually decelerates. Continued cooling eventually causes the flow to slow and partially reverse. At this transitional stage, the temperature field becomes more symmetric. As the effect of the cooling increases further, the thermal driving force of this cooler leg becomes strong enough to overcome the previous clockwise motion, causing the flow to reverse direction and develop into a counter-clockwise circulation.

This test case demonstrates that SubChCFD is capable of capturing complex unsteady phenomena such as flow reversal, having showcased its ability to model the key thermal-hydraulic characteristics of the NCL.

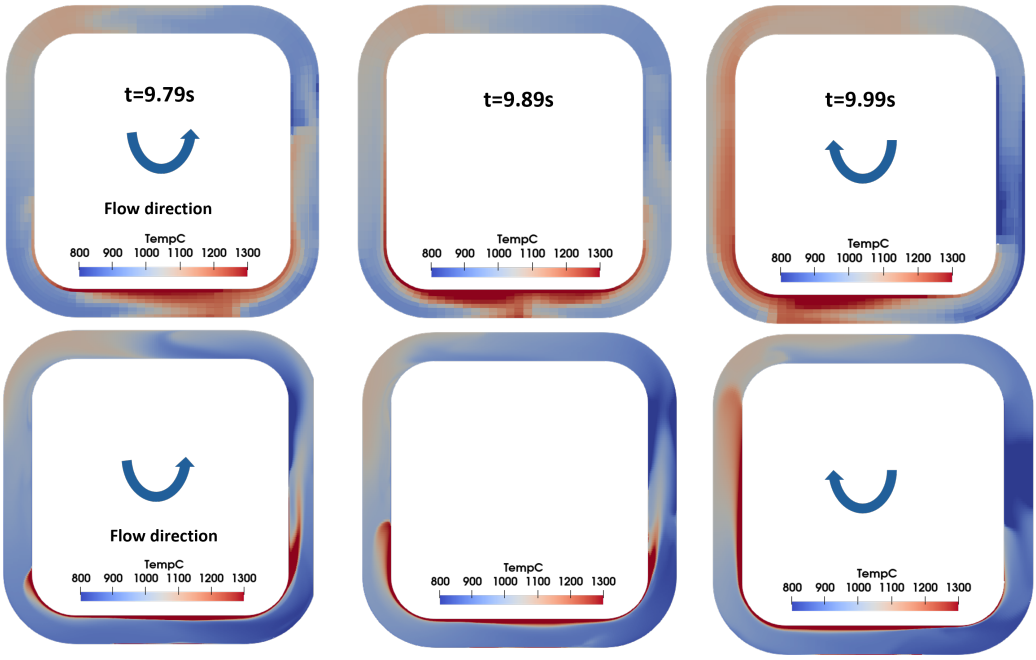

Figure 6.7: Temperature contour plots at different time instances: SubChCFD results (first row) and resolved CFD results (second row).

Figure 6.8 presents the shear stress contour plots comparing the SubChCFD results and the resolved CFD results at t = 9.79 s. The results show a high degree of

similarity between the two methods, indicating that the shear stress implementation in the elbow region captures the shear loss reasonably while using a coarse mesh.

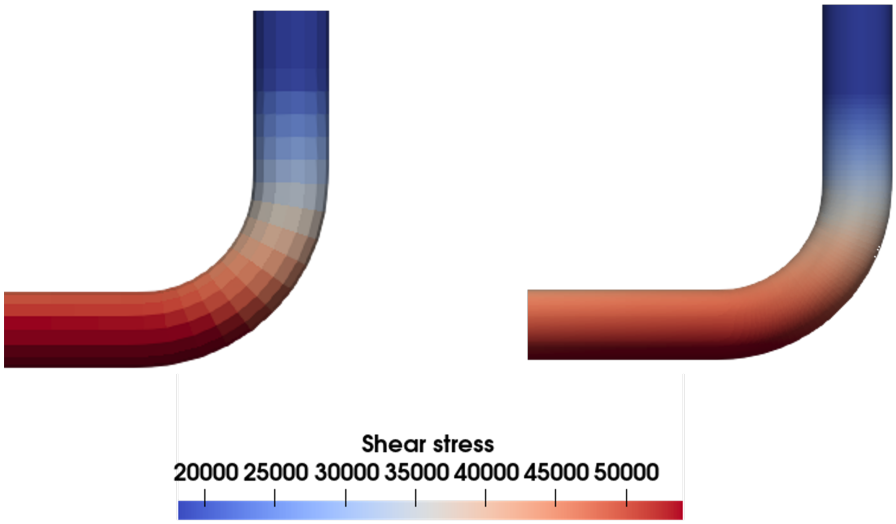

Figure 6.8: Comparison of shear stress distribution between SubChCFD and resolved CFD: SubChCFD results at 9.79s (left) and resolved CFD results at 6.17s (right).

6.4.2 Horizontal heating and horizontal cooling

The flow development in a natural circulation loop is heavily influenced by the relative positioning of the heating and cooling sections. In the previous configuration, where the heating section was horizontal and the cooling section was vertical, the system exhibited a dominant initial flow direction due to the asymmetric arrangement of the heat source and sink.

In contrast, in this case, the configuration features both the heating and cooling sections positioned horizontally and symmetrically, eliminating the natural dominance for an initial flow direction. This introduces additional challenges in flow development, as the system becomes more sensitive to localised thermal expansion effects in the heated section and momentum diffusion in the cooling region.

The objective of this case is to evaluate whether SubChCFD can reasonably capture the key flow behaviours in this configuration, including the formation of circulation patterns, transient instabilities, and flow reversals.

The velocity evolution at monitoring points 3, 6, and 7 is presented in Figure 6.9, comparing the results from resolved CFD and SubChCFD. Across all monitoring locations, SubChCFD captures the oscillations but overpredicts the velocity magnitude and oscillation frequency in comparison with the resolved CFD.

One notable observation is that the velocity magnitude fluctuates symmetrically between positive and negative values, roughly within the range of $[-4, 4]$ m/s. This differs from the previous configuration, where the presence of a vertical cooling section and the resulting asymmetry in the loop geometry promoted a dominant flow direction, leading to a more directionally biased flow pattern. In this case, since both heating and cooling sections are horizontally positioned, the system exhibits a more symmetric flow development.

The higher velocity magnitudes and increased oscillation frequency observed in SubChCFD compared to resolved CFD can be partially attributed to differences in how boundary conditions are implemented in the two approaches. Although the system geometry is symmetric, with the heater and cooler placed to avoid flow bias, the lack of a dominant flow direction increases sensitivity to boundary treatment and numerical schemes. In SubChCFD, the boundary conditions at the heater and cooler are implemented using simplified correlations and calibrated parameters (e.g., Nusselt number), which differ from the more physically detailed wall treatment used in resolved CFD. This likely contributes to the discrepancies in flow magnitude and dynamics between the two methods. Overall, SubChCFD can capture the global flow oscillations in this case.

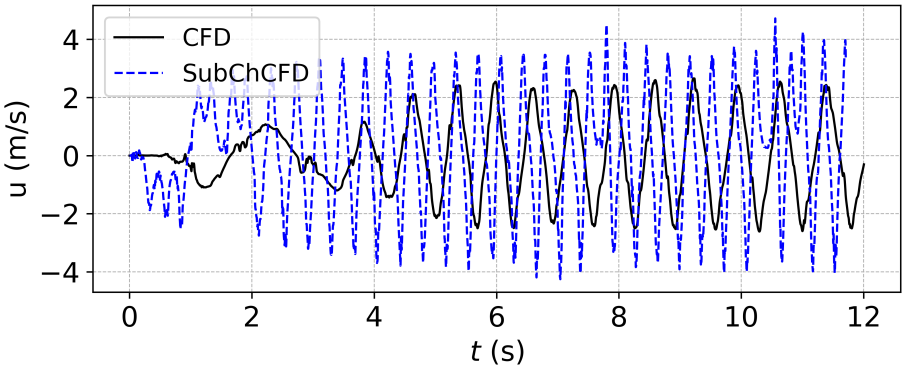

(a) Monitor 3.

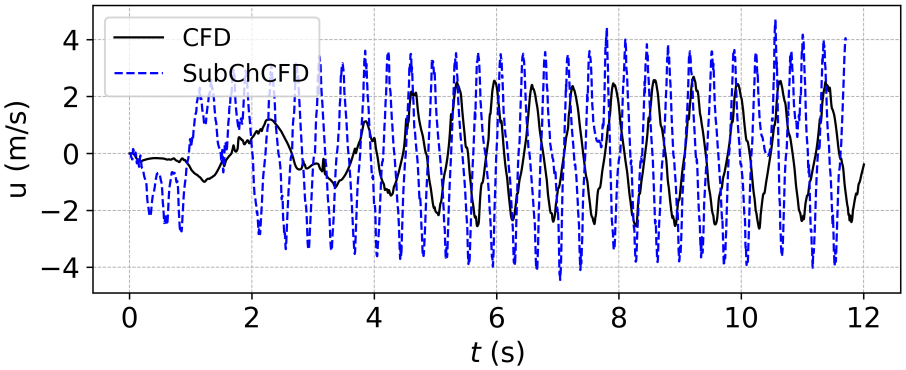

(b) Monitor 6.

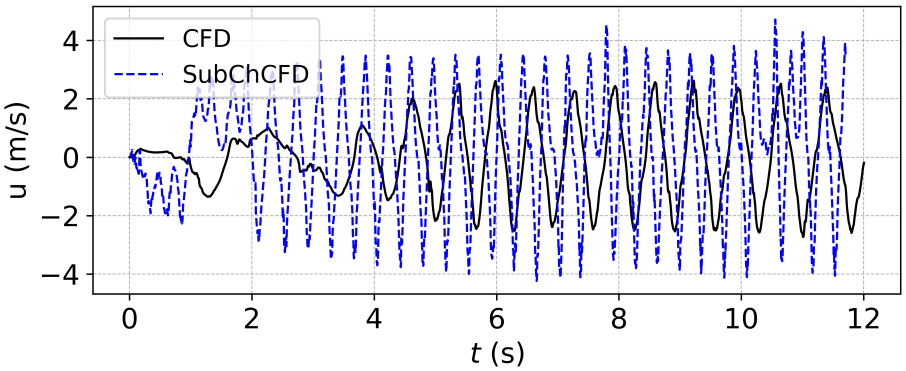

(c) Monitor 7.

Figure 6.9: Comparison of velocity oscillations between resolved CFD and SubChCFD at different monitoring locations.

The temperature contour plots from SubChCFD simulations, shown in Figure 6.10, illustrate the evolution of temperature at different time instances in the horizontal heating and horizontal cooling configuration. This setup removes the vertical asymmetry present in the previous case, allowing the flow to evolve more symmetrically.

At $t = 5.79$, the flow exhibits a clockwise circulation. As the flow enters the

cooling section, it gradually reduces in temperature. This results in a weakening of the clockwise circulation due to the thermal expansion, as observed at $t = 5.89\,\mathrm{s}$, where the flow slows and the temperature field becomes more uniformly distributed.

As the fluid passes through the horizontal cooler located at the top, it continues to lose heat while flowing downward through the right-side pipe. This sustained cooling increases the temperature difference between the right vertical pipe and the heater at the bottom. The growing imbalance enhances the thermal driving force in the right pipe. As a result, the flow reverses, leading to the development of a counter-clockwise circulation at $t = 5.99$.

These results demonstrate that, even in the absence of vertical asymmetry, SubChCFD successfully captures the unsteady evolution of the flow and the occurrence of flow reversal.

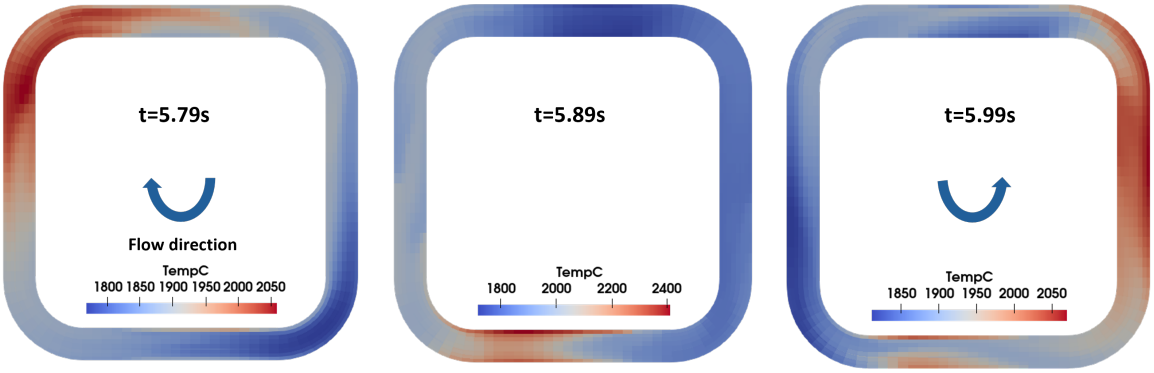

Figure 6.10: Temperature contour plots showing the flow evolution at different time steps in the horizontal heating and horizontal cooling configuration.

6.5 Conclusion

This chapter investigates the instability behaviour of a natural circulation loop under different heating and cooling configurations, focusing on a comparative analysis between SubChCFD and resolved CFD results. The objective was to develop and evaluate the capability of SubChCFD in simulating transient flow phenomena, particularly velocity oscillations and flow reversal.

The results demonstrated that SubChCFD successfully captured key unsteady behaviours, including the onset of oscillations and flow direction changes. While SubChCFD slightly overpredicts the amplitude and frequency of velocity oscillations in HHHC case, this overprediction is not observed in the HHVC case, where the agreement with resolved CFD is much closer. The overall trends remained consistent.

In both the HHVC and HHHC configurations, SubChCFD reproduced the essential flow evolution patterns.

The use of appropriate friction factor correlations, the implementation of shear stress treatment in elbow regions, and the calibration of the Nusselt number together enable SubChCFD to capture both frictional and heat transfer effects in the system. These developments enhance SubChCFD's capability to simulate the transient behaviour of natural circulation loops.

Overall, this study demonstrates the potential of SubChCFD as a viable tool for capturing instability behaviour in natural circulation loops, offering a computationally efficient approach for transient thermal-hydraulic analysis. Even though the work reported in this chapter is still preliminary and there is still significant scope for further improvement and testing.

Chapter 7

Conclusions and Future Work

7.1 Conclusions

This thesis has presented further development, validation, and demonstration of the SubChCFD for analysing thermal-hydraulic behaviour in nuclear systems. The research focused on three main areas: supercritical scenarios, wire-wrapped rod bundles, and natural circulation loops (NCLs).

The study systematically addressed several key challenges, including the rapid variation of fluid properties near the pseudo-critical point, the influence of strong buoyancy forces on flow and heat transfer, the complex crossflow and swirl phenomena induced by wire-wrapped spacers, and flow instability in natural circulation systems. The main findings from the results chapters (Chapter 4, 5 and 6) are summarised below.

Chapter 4 - Development and application of SubChCFD for supercritical fluid heat transfer:

- The SubChCFD with consideration of variable physical property was validated against ECC-SMART project cases [38]. The results confirmed its capability to predict key thermal-hydraulic behaviour under supercritical conditions.
- The SubChCFD is able to capture strong buoyancy effects on the flow redistribution across subchannels.
- The implementation of empirical correlations reduc discrepancies between SubChCFD and high-resolution CFD results.
- A newly implemented combination of heat transfer correlations, including entrance effects, improves the performance of SubChCFD for developing flow regions.

- Different frictional factor correlations were assessed, showing limited impact on axial pressure drop and radial flow redistribution
- The SubChCFD model was further validated using different heat transfer correlations in fully developed flow regions, showing reasonable agreement with experimental data.

Chapter 5 - Development for the wire-wrapped rod bundles:

- A momentum source term approach was implemented in SubChCFD to produce the flow swirl behaviour induced by wire-wrapped spacers. Its feasibility was first demonstrated in a short domain test case.
- The model showed good agreement with high-resolution CFD results in both locally and fully wire-wrapped rod bundle configurations based on ECC-SMART project [38], confirming its ability to capture the key flow features introduced by the wire-wrap geometry.
- Validation against experimental data for a 7-pin rod bundle case further demonstrated the capability of SubChCFD in predicting crossflow behaviour.

Chapter 6 - Application of SubChCFD in natural circulation loops:

- SubChCFD was applied to simulate NCL configurations. Key improvements included the implementation of a friction factor correlation for straight pipes across different flow regimes, calibration of the Nusselt number to account for thermal boundary layer development, and the modelling of shear stress effects in elbow regions.
- SubChCFD captures key transient behaviours such as oscillatory flow, temperature and velocity fluctuations, and flow reversals in both horizontal heating vertical cooling and horizontal heating horizontal cooling configurations.
- SubChCFD matched resolved CFD results trend in reproducing key instability behaviour, demonstrating its ability to simulate unsteady flow behaviour in NCLs.

Overall, this PhD study has demonstrated that the SubChCFD model is a practical and efficient tool for analysing thermal-hydraulic systems in nuclear reactors. It provides a good balance between accuracy and computational cost. The flexibility of

the model allows it to be adapted to different flow conditions and geometrical configurations through the implementation of appropriate empirical correlations. This makes SubChCFD a promising approach for engineering applications.

7.2 Future Work

Although SubChCFD has been further developed and validated in this PhD study, there are several directions it can be improved or extended in future research:

- **Buoyancy correction on friction factor**: The current friction factor correlations account for property variation, which may indirectly reflect buoyancy influence. However, these correlations do not explicitly include the buoyancy effect on wall shear stress. Future work could consider implementing correlations that directly account for buoyancy effects, particularly under strong mixed convection conditions.

- **Flow acceleration consideration**: In supercritical conditions, strong gradients in fluid properties can lead to significant flow acceleration, particularly in the axial direction. This effect is not considered in the current model. Future work could consider flow acceleration to improve the performance of SubChCFD.

- **Wire-wrap modelling**: The current momentum source approach captures the overall swirl and crossflow effects induced by wire-wraps. However, the use of a finer computational mesh could be further explored to better resolve local flow structures, such as small-scale vortices.

- **Coupling method for natural circulation loop**: In natural circulation loops, flow behaviour in elbow regions is complex. To improve accuracy, a coupling strategy with resolved CFD in these regions could be developed, allowing SubChCFD to capture detailed local flow information.

- **Validation with experiments**: Further validation against experimental data is necessary to enhance the reliability of the SubChCFD model. In particular, experiments involving mixed convection under supercritical conditions, wire-wrapped rod bundles, and a variety of flow regimes in NCLS would provide valuable benchmarks for assessing the capability of SubChCFD.

- **Demonstration for different configurations**: The current developments and validations of SubChCFD have primarily been conducted using a 2×2 rod bundle configuration. Future work should extend the application to larger and more realistic geometries.

Addressing these areas will help improve the performance of SubChCFD for both design and safety analysis in advanced nuclear reactors.

Bibliography

[1] VY Agbodemegbe, Xu Cheng, EHK Akaho, and FKA Allotey. An investigation of the effect of split-type mixing vane on extent of crossflow between subchannels through the fuel rod gaps. *Annals of Nuclear Energy*, 88:174–185, 2016.

[2] N Aksan. An overview on thermal-hydraulic phenomena for water cooled nuclear reactors; part ii: Alwrs and scwrs. *Nuclear Engineering and Design*, 354:110214, 2019.

[3] Walter Ambrosini. Lesson learned from the adoption of numerical techniques in the analysis of nuclear reactor thermal-hydraulic phenomena. *Progress in Nuclear Energy*, 50(8):866–876, 2008.

[4] Walter Ambrosini and JC Ferreri. The effect of truncation error on the numerical prediction of linear stability boundaries in a natural circulation single-phase loop. *Nuclear Engineering and Design*, 183(1-2):53–76, 1998.

[5] Walter Ambrosini, Nicola Forgione, JC Ferreri, and M Bucci. The effect of wall friction in single-phase natural circulation stability at the transition between laminar and turbulent flow. *Annals of Nuclear Energy*, 31(16):1833–1865, 2004.

[6] Nolan Anderson, Yassin Hassan, and Richard Schultz. Analysis of the hot gas flow in the outlet plenum of the very high temperature reactor using coupled relap5-3d system code and a cfd code. *Nuclear Engineering and Design*, 238(1):274–279, 2008.

[7] ANSYS Inc. *ANSYS Fluent Theory Guide*. ANSYS Inc., 2024. Release 2024R1.

[8] F. Archambeau, N. Mechitoua, and M. Sakiz. Code_saturne: A finite volume code for the computation of turbulent incompressible flows—industrial applications. *International Journal on Finite Volumes*, 1(1), 2004.

[9] Joong Hun Bae, Jung Yul Yoo, and Haecheon Choi. Direct numerical simulation of turbulent supercritical flows with heat transfer. *Physics of fluids*, 17(10), 2005.

[10] E Baglietto and H Ninokata. A turbulence model study for simulating flow inside tight lattice rod bundles. *Nuclear Engineering and Design*, 235(7):773–784, 2005.

[11] E Baglietto, H Ninokata, and Takeharu Misawa. Cfd and dns methodologies development for fuel bundle simulations. *Nuclear Engineering and Design*, 236(14-16):1503–1510, 2006.

[12] G Bergeles and Wolfgang Rodi. *Engineering Turbulence Modelling and Experiments-3*. Newnes, 2012.

[13] Theodore L Bergman, Adrienne S Lavine, Frank P Incropera, and David P DeWitt. *Introduction to heat transfer*. John Wiley & Sons, 2011.

[14] Davide Bertolotto, Annalisa Manera, Simon Frey, Horst-Michael Prasser, and Rakesh Chawla. Single-phase mixing studies by means of a directly coupled cfd/system-code tool. *Annals of Nuclear Energy*, 36(3):310–316, 2009.

[15] Ulrich Bieder, Valérie Barthel, Frederic Ducros, Partrick Quéméré, and Simone Vandroux. Cfd calculations of wire wrapped fuel bundles: modeling and validation strategies. In *Workshop Proceedings of Computational Fluid Dynamics for Nuclear Reactor Safety Applications (CFD4NRS-3)*, volume 90, 2010.

[16] Ulrich Bieder, François Falk, and Gauthier Fauchet. Les analysis of the flow in a simplified pwr assembly with mixing grid. *Progress in Nuclear Energy*, 75:15–24, 2014.

[17] AA Bishop, RO Sandberg, and LS Tong. Forced-convection heat transfer to water at near-critical temperatures and supercritical pressures. Technical report, Westinghouse Electric Corp., Pittsburgh, Pa. Atomic Power Div., 1964.

[18] ANIS BOUSBIA-SALAH, PETRUZZI ALESSANDRO, et al. State of the art in using best estimate calculation tools in nuclear technology. *Nuclear engineering and technology*, 38(1):11–32, 2006.

[19] Jacopo Buongiorno, James W Sterbentz, and Philip E MacDonald. Study of solid moderators for the thermal-spectrum supercritical water-cooled reactor. *Nuclear technology*, 153(3):282–303, 2006.

[20] Yuli Cao, Ruina Xu, S He, and Peixue Jiang. Accelerating turbulence in heated micron tubes at supercritical pressure. *Journal of Fluid Mechanics*, 972:A13, 2023.

[21] Francesco Carbone and Walter Ambrosini. Steady-state and stability analysis of natural circulation with fluids at supercritical pressure. In *International Conference on Nuclear Engineering*, volume 50039, page V003T09A001. American Society of Mechanical Engineers, 2016.

[22] Yunus Cengel and John Cimbala. *Ebook: Fluid mechanics fundamentals and applications (si units)*. McGraw Hill, 2013.

[23] Laltu Chandra, Ferry Roelofs, Michiel Houkema, and Bouke Jonker. A stepwise development and validation of a rans based cfd modelling approach for the hydraulic and thermal-hydraulic analyses of liquid metal flow in a fuel assembly. *Nuclear Engineering and Design*, 239(10):1988–2003, 2009.

[24] Khurrum Saleem Chaudri, Jaeha Kim, and Yonghee Kim. Development and validation of a fast sub-channel code for lwr multi-physics analyses. *Nuclear Engineering and Technology*, 51(5):1218–1230, 2019.

[25] Guangliang Chen, Zhijian Zhang, Zhaofei Tian, Lei Li, Xiaomeng Dong, and Haoran Ju. Design of a cfd scheme using multiple rans models for pwr. *Annals of Nuclear Energy*, 102:349–358, 2017.

[26] SK Chen, NE Todreas, and NT Nguyen. Evaluation of existing correlations for the prediction of pressure drop in wire-wrapped hexagonal array pin bundles. *Nuclear Engineering and Design*, 267:109–131, 2014.

[27] Zhao Chen, Xue-Nong Chen, Andrei Rineiski, Pengcheng Zhao, and Hongli Chen. Coupling a cfd code with neutron kinetics and pin thermal models for nuclear reactor safety analyses. *Annals of Nuclear Energy*, 83:41–49, 2015.

[28] X Cheng, YH Yang, and SF Huang. A simplified method for heat transfer prediction of supercritical fluids in circular tubes. *Annals of Nuclear Energy*, 36(8):1120–1128, 2009.

[29] Michael E Conner, Emilio Baglietto, and Abdelaziz M Elmahdi. Cfd methodology and validation for single-phase flow in pwr fuel assemblies. *Nuclear Engineering and Design*, 240(9):2088–2095, 2010.

[30] Santiago Corzo, Damian Ramajo, and Norberto Nigro. 1/3d modeling of the core coolant circuit of a phwr nuclear power plant. *Annals of Nuclear Energy*, 83:386–397, 2015.

[31] Xiang-Zhe Cui and Kwang-Yong Kim. Three-dimensional analysis of turbulent heat transfer and flow through mixing vane in a subchannel of nuclear reactor. *Journal of Nuclear Science and Technology*, 40(10):719–724, 2003.

[32] F D'Auria, M Frogheri, and M Misale. System codes capabilities in predicting instabilities in single-phase natural circulation. 1997.

[33] Ajoy Debbarma and KM Pandey. Numerical analysis of the flow and heat transfer in the sub-channel of supercritical water reactor. In *ASME International Mechanical Engineering Congress and Exposition*, volume 56345, page V08AT09A048. American Society of Mechanical Engineers, 2013.

[34] Jian Deng, Qi Lu, Yu Liu, Xiaoyu Wang, Xiaolei Yang, Yong Zhang, and Jibin Zhang. Review of sub-channel code development for pressurized water reactor and introduction of corth-v2. 0 sub-channel code. *Progress in Nuclear Energy*, 125:103373, 2020.

[35] Jian Deng, Qi Lu, Di Wu, Chenglong Wang, Chao Guo, Zhengpeng Mi, Daishun Huang, Mingyu Yan, Xiaoyu Wang, Xi Chen, et al. Sub-channel code development of lead-bismuth eutectic fast reactor available for multiple fuel assembly structures. *Annals of Nuclear Energy*, 149:107769, 2020.

[36] Gilles Desrayaud, Alberto Fichera, and Guy Lauriat. Two-dimensional numerical analysis of a rectangular closed-loop thermosiphon. *Applied thermal engineering*, 50(1):187–196, 2013.

[37] FW Dittus. Heat transfer in automobile radiators of the tubular type. *University of California Publications in Engineering*, 1930.

[38] ECC-SMART Project Consortium. Enhanced computational capabilities for small modular reactors and advanced reactor technologies (ecc-smart). https://ecc-smart.eu/, 2020. Horizon 2020 Project.

[39] Xiande Fang, Yu Xu, and Zhanru Zhou. New correlations of single-phase friction factor for turbulent pipe flow and evaluation of existing single-phase friction factor correlations. *Nuclear Engineering and Design*, 241(3):897–902, 2011.

[40] Carlo Fiorina, Ivor Clifford, Manuele Aufiero, and Konstantin Mikityuk. Genfoam: a novel openfoam® based multi-physics solver for 2d/3d transient analysis of nuclear reactors. *Nuclear Engineering and Design*, 294:24–37, 2015.

[41] Paul Fischer, James Lottes, Andrew Siegel, and Giuseppe Palmiotti. Large eddy simulation of wire-wrapped fuel pins i: Hydrodynamics in a periodic array. In *Joint International Topical Meeting on Mathematics & Computation and Supercomputing in Nuclear Applications, Monterey, CA, USA*. Citeseer, 2007.

[42] R Gajapathy, K Velusamy, P Selvaraj, P Chellapandi, and SC Chetal. A comparative cfd investigation of helical wire-wrapped 7, 19 and 37 fuel pin bundles and its extendibility to 217 pin bundle. *Nuclear Engineering and Design*, 239(11):2279–2292, 2009.

[43] Wu Gang, Jie Pan, Qincheng Bi, Zhendong Yang, and Han Wang. Heat transfer characteristics of supercritical pressure water in vertical upward annuli. *Nuclear Engineering and Design*, 273:449–458, 2014.

[44] Han-Yang Gu, Zhen-Xiao Hu, Da Liu, Hong-Bo Li, Meng Zhao, and Xu Cheng. Experimental study on heat transfer to supercritical water in 2× 2 rod bundle with wire wraps. *Experimental Thermal and Fluid Science*, 70:17–28, 2016.

[45] HY Gu, Xu Cheng, and YH Yang. Cfd analysis of thermal–hydraulic behavior in scwr typical flow channels. *Nuclear Engineering and Design*, 238(12):3348–3359, 2008.

[46] Sahil Gupta, Amjad Farah, Krysten King, Sarah Mokry, and Igor Pioro. Developing new heat-transfer correlation for supercritical-water flow in vertical bare tubes. In *International Conference on Nuclear Engineering*, volume 49309, pages 809–817, 2010.

[47] Kevin P Hallinan and Raymond Viskanta. Heat transfer from a vertical tube bundle under natural circulation conditions. *International journal of heat and fluid flow*, 6(4):256–264, 1985.

[48] Gábor Házi. On turbulence models for rod bundle flow computations. *Annals of Nuclear Energy*, 32(7):755–761, 2005.

[49] Jundi He, Ran Tian, PX Jiang, and Shuisheng He. Turbulence in a heated pipe at supercritical pressure. *Journal of Fluid Mechanics*, 920:A45, 2021.

[50] S He, WS Kim, and JH Bae. Assessment of performance of turbulence models in predicting supercritical pressure heat transfer in a vertical tube. *International Journal of Heat and Mass Transfer*, 51(19-20):4659–4675, 2008.

[51] H Helf, G Bava, M Champ, T Raga, DJ Hanson, HLO Holmstrom, G Jung, R Mandl, J Miettinen, SA Naff, et al. Catalogue of generic plant states leading to core melt in pwrs. *includes Appendix*, 1, 1996.

[52] Darren L Hitt, Christopher M Danforth, et al. A numerical investigation of 3-d flow regimes in a toroidal natural convection loop. *International journal of heat and mass transfer*, 54(25-26):5253–5261, 2011.

[53] Rui Hu and Thomas H Fanning. A momentum source model for wire-wrapped rod bundles—concept, validation, and application. *Nuclear Engineering and Design*, 262:371–389, 2013.

[54] Zhenxiao Hu, Da Liu, Jiaqi Tao, and Hanyang Gu. Experimental study on heat transfer of supercritical water in 2× 2 rod bundle with wrapped wire. *Atomic Energy Science and Technology*, 50(9):1606–1611, 2016.

[55] ZX Hu, HB Li, JQ Tao, D Liu, and HY Gu. Experimental study on heat transfer of supercritical water flowing upward and downward in 2× 2 rod bundle with wrapped wire. *Annals of Nuclear Energy*, 111:50–58, 2018.

[56] INTERNATIONAL ATOMIC ENERGY AGENCY. Progress in methodologies for the assessment of passive safety system reliability in advanced reactors. Technical Report IAEA-TECDOC-1752, IAEA, Vienna, 2014.

[57] Kostadin N Ivanov, Tara M Beam, Anthony J Baratta, Adi Irani, and Nick Trikouros. Pressurised water reactor main steam line break (mslb) benchmark. v. 1. final specifications. 1999.

[58] J D_ Jackson. Consideration of the heat transfer properties of supercritical pressure water in connection with the cooling of advanced nuclear reactors. In *The 13th pacific basin nuclear conference. Abstracts*, 2002.

[59] JD Jackson. Fluid flow and convective heat transfer to fluids at supercritical pressure. *Nuclear Engineering and Design*, 264:24–40, 2013.

[60] JD Jackson, MA Cotton, and BP Axcell. Studies of mixed convection in vertical tubes. *International journal of heat and fluid flow*, 10(1):2–15, 1989.

[61] J-J Jeong, KS Ha, BD Chung, and WJ Lee. Development of a multi-dimensional thermal-hydraulic system code, mars 1.3. 1. *Annals of Nuclear Energy*, 26(18):1611–1642, 1999.

[62] Adam J. Johnston, Rachael L. Baumann, and John L. Falconer. Temperature-entropy diagram for water. https://demonstrations.wolfram.com/TemperatureEntropyDiagramForWater/, 2016. Wolfram Demonstrations Project.

[63] Donald D Joye. Pressure drop correlation for laminar, mixed convection, aiding flow heat transfer in a vertical tube. *International journal of heat and fluid flow*, 24(2):260–266, 2003.

[64] Bae Kang-Mok, Joo Hyung-Kook, and Bae Yoon-Yeong. Conceptual design of a 1400 mwe supercritical water cooled reactor core with a cruciform type u/zr solid moderator. 2007.

[65] Min-Tsung Kao, Chung-Yun Wu, Ching-Chang Chieng, Yiban Xu, Kun Yuan, Milorad Dzodzo, Michael Conner, Steven Beltz, Sumit Ray, and Teresa Bissett. Cfd analysis of pwr core top and reactor vessel upper plenum internal subdomain models. *Nuclear Engineering and Design*, 241(10):4181–4193, 2011.

[66] Min-Tsung Kao, Chung-Yun Wu, Ching-Chang Chieng, Yiban Xu, Kun Yuan, Milorad B Dzodzo, Michael Conner, Steven Beltz, Sumit Ray, and Teresa Bissett. Cfd analysis of pwr reactor vessel upper plenum sections: flow simulation in control rods guide tubes. In *International Conference on Nuclear Engineering*, volume 49323, pages 499–506, 2010.

[67] Nobuhide Kasagi and Mitsugu Nishimura. Direct numerical simulation of combined forced and natural turbulent convection in a vertical plane channel. *International Journal of Heat and Fluid Flow*, 18(1):88–99, 1997.

[68] WS Kim, S He, and JD Jackson. Assessment by comparison with dns data of turbulence models used in simulations of mixed convection. *International journal of heat and mass transfer*, 51(5-6):1293–1312, 2008.

[69] PL Kirillov. Heat and mass transfer at supercritical parameters. the short review of researches in russia. theory and experiments. In *Proceedings of the first international symposium on supercritical water-cooled reactors, design and technology*, 2000.

[70] PL Kirillov, AA Kolosov, Eh I Petrova, AM Smirnov, and OA Sudnitsyn. Temperature distribution in a turbulent water flow under supercritical pressures circular tubes. Technical report, Gosudarstvennyj Komitet po Ispol'zovaniyu Atomnoj Ehnergii SSSR, 1986.

[71] S Koshizuka, Naoki Takano, and Y Oka. Numerical analysis of deterioration phenomena in heat transfer to supercritical water. *International journal of heat and mass transfer*, 38(16):3077–3084, 1995.

[72] Juraj Králik. Cfd simulation of air flow over an object with gable roof, revised with y+ approach. 2016.

[73] EA Krasnoshchekov, VS Protopopov, F Van, and IV Kuraeva. Experimental investigation of heat transfer for carbon dioxide in the supercritical region. In *Proceedings of the 2nd All-Soviet Union Conference on Heat and Mass Transfer, Minsk, Belarus*, volume 1, pages 26–35, 1964.

[74] Jayaraj Yallappa Kudariyawar, Abhijeet Mohan Vaidya, Naresh Kumar Maheshwari, and Polepalle Satyamurthy. Computational study of instabilities in a rectangular natural circulation loop using 3d cfd simulation. *International Journal of Thermal Sciences*, 101:193–206, 2016.

[75] Gaurav Kumar and Raj Kumar Singh. Supercritical water flow in heated wire wrapped rod bundle channels: A review. *Progress in Nuclear Energy*, 158:104620, 2023.

[76] Adrienne S Lavine, Ralph Greif, and Joseph AC Humphrey. A three-dimensional analysis of natural convection in a toroidal loop—the effect of grashof number. *International journal of heat and mass transfer*, 30(2):251–262, 1987.

[77] AS Lavine, R Greif, and JAC Humphrey. Three-dimensional analysis of natural convection in a toroidal loop: effect of tilt angle. 1986.

[78] Eric W. Lemmon, Marcia L. Huber, and Mark O. McLinden. NIST reference fluid thermodynamic and transport properties database (refprop): Version 10.0. National Institute of Standards and Technology, Standard Reference Database 23, 2022.

[79] Laurence KH Leung, Yanfei Rao, and Krishna Podila. Assessment of computational tools in support of heat-transfer correlation development for fuel assembly of canadian supercritical water-cooled reactor. *Journal of Nuclear Engineering and Radiation Science*, 2(1):011006, 2016.

[80] MJ Lewis, R Pochard, F D'auria, H Karwat, K Wolfert, G Yadigaroglu, and HLO Holmstrom. Thermohydraulics of emergency core cooling in light water reactors-a state of the art report. *CSNI Rep*, pages 2020–01, 1989.

[81] Hongzhi Li, Haijun Wang, Yushan Luo, Hongfang Gu, Xiaobao Shi, Tingkuan Chen, Eckart Laurien, and Yu Zhu. Experimental investigation on heat transfer from a heated rod with a helically wrapped wire inside a square vertical channel to water at supercritical pressures. *Nuclear Engineering and Design*, 239(10):2004–2012, 2009.

[82] Jiankang Li and JD Jackson. Buoyancy-influenced turbulent heat transfer to air flowing variable property in a uniformly heated vertical tube. *TURBULENT HEAT TRANSFER*, 1998.

[83] B Liu, S He, C Moulinec, and J Uribe. Sub-channel cfd for nuclear fuel bundles. *Nuclear Engineering and Design*, 355:110318, 2019.

[84] B Liu, S He, C Moulinec, and J Uribe. Coupled porous media approaches in sub-channel cfd. *Nuclear Engineering and Design*, 377:111159, 2021.

[85] CC Liu, YM Ferng, and CK Shih. Cfd evaluation of turbulence models for flow simulation of the fuel rod bundle with a spacer assembly. *Applied Thermal Engineering*, 40:389–396, 2012.

[86] Lei Liu, Zejun Xiao, Xiao Yan, Xiaokang Zeng, and Yanping Huang. Numerical simulation of heat transfer deterioration phenomenon to supercritical water in annular channel. *Annals of Nuclear Energy*, 53:170–181, 2013.

[87] XJ Liu and N Scarpelli. Development of a sub-channel code for liquid metal cooled fuel assembly. *Annals of Nuclear Energy*, 77:425–435, 2015.

[88] Amit Mangal, Vikas Jain, and AK Nayak. Capability of the relap5 code to simulate natural circulation behavior in test facilities. *Progress in Nuclear Energy*, 61:1–16, 2012.

[89] RP Martin and BK Taylor. Benchmarking assessment of relap5/mod3 for the low flow and natural circulation experiment. Technical report, Westinghouse Savannah River Co., Aiken, SC (United States), 1992.

[90] A Mertol, R Greif, and Y Zvirin. Two-dimensional study of heat transfer and fluid flow in a natural convection loop. 1982.

[91] E Merzari, H Ninokata, and E Baglietto. Numerical simulation of flows in tight-lattice fuel bundles. *Nuclear Engineering and Design*, 238(7):1703–1719, 2008.

[92] Elia Merzari, Paul Fischer, H Yuan, Katrien Van Tichelen, Steven Keijers, Jeroen De Ridder, Joris Degroote, Jan Vierendeels, Heleen Doolaard, VR Gopala, et al. Benchmark exercise for fluid flow simulations in a liquid metal fast reactor fuel assembly. *Nuclear Engineering and Design*, 298:218–228, 2016.

[93] Mario Misale, Monica Frogheri, Francesco D'Auria, Emanuele Fontani, and Alicia Garcia. Analysis of single-phase natural circulation experiments by system codes. *International Journal of Thermal Sciences*, 38(11):977–983, 1999.

[94] A Moorthi, Anil Kumar Sharma, and K Velusamy. A review of sub-channel thermal hydraulic codes for nuclear reactor core and future directions. *Nuclear Engineering and Design*, 332:329–344, 2018.

[95] Yoshiaki Oka, Seiichi Koshizuka, and Tomoko Yamasaki. Direct cycle light water reactor operating at supercritical pressure. *Journal of Nuclear Science and Technology*, 29(6):585–588, 1992.

[96] David Palko and Henryk Anglart. Theoretical and numerical study of heat transfer deterioration in high performance light water reactor. *Science and Technology of Nuclear Installations*, 2008(1):405072, 2008.

[97] Marco Pizzarelli. The status of the research on the heat transfer deterioration in supercritical fluids: A review. *International Communications in Heat and Mass Transfer*, 95:132–138, 2018.

[98] Krishna Podila and Yanfei Rao. Cfd modelling of supercritical water flow and heat transfer in a 2× 2 fuel rod bundle. *Nuclear Engineering and Design*, 301:279–289, 2016.

[99] W David Pointer, Justin Thomas, Tom Fanning, Paul Fischer, Andrew Siegel, Jeffrey Smith, and Akira Tokuhiro. Rans-based cfd simulations of sodium fast reactor wire-wrapped pin bundles. 2009.

[100] Stephen B Pope. Turbulent flows. *Measurement Science and Technology*, 12(11):2020–2021, 2001.

[101] Mohammad Mizanur Rahman, Ji Dongxu, Mehrdad Shahmohammadi Beni, Ho Choi Hei, Weidong He, and Jiyun Zhao. Supercritical water heat transfer for nuclear reactor applications: A review. *Annals of Nuclear Energy*, 97:53–65, 2016.

[102] Mohammad Mizanur Rahman, Ji Dongxu, Nusrat Jahan, Massimo Salvatores, and Jiyun Zhao. Design concepts of supercritical water-cooled reactor (scwr) and nuclear marine vessel: A review. *Progress in Nuclear Energy*, 124:103320, 2020.

[103] F Roelofs, VR Gopala, L Chandra, M Viellieber, and A Class. Simulating fuel assemblies with low resolution cfd approaches. *Nuclear engineering and design*, 250:548–559, 2012.

[104] Ferry Roelofs, Vinay R Gopala, Santhosh Jayaraju, Afaque Shams, and Ed Komen. Review of fuel assembly and pool thermal hydraulics for fast reactors. *Nuclear Engineering and Design*, 265:1205–1222, 2013.

[105] DS Rowe. Cobra iiic: digital computer program for steady state and transient thermal-hydraulic analysis of rod bundle nuclear fuel elements. Technical report, Battelle Pacific Northwest Labs., Richland, WA (United States), 1973.

[106] Gaiane Sabundjian, Delvonei Alves de Andrade, Pedro Ernesto Umbehaun, Walmir Maximo Torres, Alfredo Jose Alvim de Castro, Francisco A Braz Filho, Eduardo Madeira Borges, Junior Belchior, Ricardo Takeshi Vieira da Rocha, Osvaldo Luiz Almeida Damy, et al. Relap5 simulation for one and two-phase natural circulation phenomenon. 2007.

[107] E Schmidt, E Eckert, and U Grigull. *Heat transfer by liquids near the critical state*. Wright Field, Air Materiel Command, 1946.

[108] Kim Seong Hoon, Kim Young In, Bae Yoon Yeong, and Cho Bong Hyun. Numerical simulation of the vertical upward flow of water in a heated tube at supercritical pressure. Technical report, American Nuclear Society, 555 North Kensington Avenue, La Grange Park, IL . . . , 2004.

[109] Jianqiang Shan, Henan Wang, Wei Liu, Linxing Song, Xuanxiang Chen, and Yang Jiang. Subchannel analysis of wire wrapped scwr assembly. *Science and Technology of Nuclear Installations*, 2014(1):301052, 2014.

[110] Jianqiang Shan, Bo Zhang, Changying Li, and Laurence KH Leung. Scwr subchannel code athas development and candu-scwr analysis. *Nuclear Engineering and Design*, 239(10):1979–1987, 2009.

[111] Jan-Patrice Simoneau, Julien Champigny, Brian Mays, and Lewis Lommers. Three-dimensional simulation of the coupled convective, conductive, and radiative heat transfer during decay heat removal in an htr. *Nuclear Engineering and Design*, 237(15-17):1923–1937, 2007.

[112] Jorge Solis, Kostadin N Ivanov, Baris Sarikaya, Andy M Olson, and Kenneth W Hunt. Boiling water reactor turbine trip (tt) benchmark. volume i: Final specifications. Technical report, Organisation for Economic Co-Operation and Development, 2001.

[113] D Squarer, T Schulenberg, D Struwe, Y Oka, D Bittermann, N Aksan, Cs Maraczy, Riitta Kyrki-Rajamäki, A Souyri, and P Dumaz. High performance light water reactor. *Nuclear Engineering and Design*, 221(1-3):167–180, 2003.

[114] BT Swapnalee and PK Vijayan. A generalized flow equation for single phase natural circulation loops obeying multiple friction laws. *International Journal of Heat and Mass Transfer*, 54(11-12):2618–2629, 2011.

[115] HS Swenson, JR Carver, and CR d Kakarala. Heat transfer to supercritical water in smooth-bore tubes. 1965.

[116] Neil E Todreas and Mujid S Kazimi. Thermal hydraulic fundamentals. *(No Title)*, 1990.

[117] Antonio Toti, Jan Vierendeels, and F Belloni. Improved numerical algorithm and experimental validation of a system thermal-hydraulic/cfd coupling method for multi-scale transient simulations of pool-type reactors. *Annals of Nuclear Energy*, 103:36–48, 2017.

[118] Nobumasa Tsuji, Masaaki Nakano, Eiji Takada, Kazumi Tokuhara, Kazutaka Ohashi, Futoshi Okamoto, Yujiro Tazawa, Yoshitomo Inaba, and Yukio Tachibana. Study of the applicability of cfd calculation for httr reactor. *Nuclear Engineering and Design*, 271:564–568, 2014.

[119] Henk Kaarle Versteeg. *An introduction to computational fluid dynamics the finite volume method, 2/E*. Pearson Education India, 2007.

[120] Mathias Viellieber and Andreas G Class. Anisotropic porosity formulation of the coarse-grid-cfd (cgcfd). In *International Conference on Nuclear Engineering*, volume 44984, pages 473–483. American Society of Mechanical Engineers, 2012.

[121] PK Vijayan, H Austregesilo, and V Teschendorff. Simulation of the unstable oscillatory behavior of single-phase natural circulation with repetitive flow reversals in a rectangular loop using the computer code athlet. *Nuclear Engineering and Design*, 155(3):623–641, 1995.

[122] PK Vijayan, SK Mehta, and AW Date. On the steady-state performance of natural circulation loops. *Int. J. Heat Mass Transfer*, 34(9):2219–2230, 1991.

[123] PK Vijayan, AK Nayak, DS Pilkhwal, D Saha, and V Venkat Raj. Effect of loop diameter on the stability of single-phase natural circulation in rectangular loops. In *Nureth*, volume 5, pages 61–267, 1992.

[124] Han Wang, Qincheng Bi, and Laurence KH Leung. Heat transfer from a 2× 2 wire-wrapped rod bundle to supercritical pressure water. *International Journal of Heat and Mass Transfer*, 97:486–501, 2016.

[125] Han Wang, Muchuan Sun, Dajun Fan, Hao Hu, Peiqi Liang, and Jianguo Yan. Experimental investigation of the crossflow of water in a 7-pin wire-wrapped rod bundle. *Experimental Thermal and Fluid Science*, 149:111010, 2023.

[126] Han Wang, Shunqi Wang, Jinguang Zang, Junfeng Wang, and Yanping Huang. Direct numerical simulation of the turbulent flow and heat transfer of supercritical co2 in a semicircular pipe. *International Journal of Heat and Mass Transfer*, 168:120882, 2021.

[127] Mingjun Wang, Yingjie Wang, Wenxi Tian, Suizheng Qiu, and GH Su. Recent progress of cfd applications in pwr thermal hydraulics study and future directions. *Annals of Nuclear Energy*, 150:107836, 2021.

[128] Pierre Welander. On the oscillatory instability of a differentially heated fluid loop. *Journal of Fluid Mechanics*, 29(1):17–30, 1967.

[129] CL Wheeler, CW Stewart, RJ Cena, DS Rowe, and AM Sutey. Cobra-iv-i: An interim version of cobra for thermal-hydraulic analysis of rod bundle nuclear fuel elements and cores. Technical report, Battelle Pacific Northwest Labs., Richland, WA (United States), 1976.

[130] Frank M. White. *Viscous Fluid Flow*. McGraw-Hill Education, 3rd edition, 2006.

[131] Frank M White. Fluid mechanics mcgraw-hill series in mechanical engineering. *Univ. Rhode Isl*, 157:813, 2007.

[132] Wikipedia contributors. Moody chart. https://en.wikipedia.org/wiki/Moody$_chart, n.d. Acces
$2025 - 04 - 29$.

[133] Dean Wilson, Hector Iacovides, and Tim Craft. Les and unsteady rans computations of natural convection cooling loops. *Chemical Engineering Research and Design*, 194:211–224, 2023.

[134] Dean Wilson, Hector Iacovides, and Tim Craft. Numerical insights into the transient behaviour of single-phase natural circulation loops for nuclear passive cooling applications. *Annals of Nuclear Energy*, 208:110730, 2024.

[135] Dean Wilson, Hector Iacovides, and Timothy Craft. Numerical insights into the transient behaviour of single phase natural convection loops for nuclear passive cooling applications. In *11th International Symposium on Turbulence and Shear Flow Phenomena (TSFP11). Southampton, UK*, 2019.

[136] Pan Wu, Yanhao Ren, Min Feng, Jianqiang Shan, Yanping Huang, and Wen Yang. A review of existing supercritical water reactor concepts, safety analysis codes and safety characteristics. *Progress in Nuclear Energy*, 153:104409, 2022.

[137] K Yamagata, K Nishikawa, S Hasegawa, T Fujii, and S Yoshida. Forced convective heat transfer to supercritical water flowing in tubes. *International journal of heat and mass transfer*, 15(12):2575–2593, 1972.

[138] Tohru Yamashita, Hideo Mori, Suguru Yoshida, and Masaki Ohno. Heat transfer and pressure drop of a supercritical pressure fluid flowing in a tube of small diameter. *Memoirs of the Faculty of Engineering, Kyushu University*, 63(4):227–244, 2003.

[139] Metin Yetisir, Michel Gaudet, Jeremy Pencer, Michael McDonald, David Rhodes, Holly Hamilton, and Laurence Leung. Canadian supercritical water-cooled reactor core concept and safety features. *CNL Nuclear Review (Online)*, 5(2):189–202, 2016.

[140] Suguru YOSHIDA. Heat transfer to supercritical pressure fluids flaming in tubes. *Proc. SCR-2000, Tokyo, Japan, Nov. 6-9*, pages 72–78, 2000.

[141] Jongwoo You, Jung Y Yoo, and Haecheon Choi. Direct numerical simulation of heated vertical air flows in fully developed turbulent mixed convection. *International Journal of Heat and Mass Transfer*, 46(9):1613–1627, 2003.

[142] G Zhang, YH Yang, HY Gu, and YQ Yu. Coolant distribution and mixing at the core inlet of pwr in a real geometry. *Annals of Nuclear Energy*, 60:187–194, 2013.

[143] Kanglong Zhang. The multiscale thermal-hydraulic simulation for nuclear reactors: A classification of the coupling approaches and a review of the coupled codes. *International Journal of Energy Research*, 44(5):3295–3315, 2020.

[144] M Zhao, HY Gu, and X Cheng. Experimental study on heat transfer of supercritical water flowing downward in circular tubes. *Annals of Nuclear Energy*, 63:339–349, 2014.

[145] Yu Zhu. Numerical investigation of the flow and heat transfer within the core cooling channel of a supercritical water reactor. 2010.